SINGLE MOLECULE DNA DYNAMICS IN MICRO- AND NANO-FLUIDIC DEVICES

by

JING TANG

B.S. Chemical Engineering, Tsinghua University (2005),
M.S. Chemical Engineering Practice, Massachusetts Institute of Technology (2009).

Submitted to the Department of Chemical Engineering
in partial fulfillment of the requirements for the degree of

Doctor of Philosophy in Chemical Engineering

at the

MASSACHUSETTS INSTITUTE OF TECHNOLOGY

October 2010
[February 2011]

© Massachusetts Institute of Technology 2010. All rights reserved.

ARCHIVES
MASSACHUSETTS INSTITUTE OF TECHNOLOGY
FEB 09 2011
LIBRARIES

Author____
Department of Chemical Engineering
October 21, 2010

Certified by______________________________________
Patrick S. Doyle
Associate Professor of Chemical Engineering
Thesis Supervisor

Accepted by______________________________________
William M. Deen
Chairman, Department Committee on Graduate Students

Single Molecule DNA Dynamics in Micro- and Nano-fluidic Devices

by
Jing Tang

Submitted to the Department of Chemical Engineering
on October 21, 2010, in partial fulfillment of the
requirements for the degree of
Doctor of Philosophy in Chemical Engineering

Abstract

Rapid genome characterization is one of the grand challenges of genome science today. Although the complete sequences of certain representative human genomes have been determined, genomes from a much larger number of individuals are yet to be studied in order to fully understand genome diversity and genetic diseases. While current state-of-the-art sequencing technologies are limited by the large timescale and cost required to analyze a single sample, an alternative strategy termed DNA mapping has recently received considerable attention. Unlike sequencing which produces single-base resolution, DNA mapping resolves coarse-scale (~kbp) information of the sequence, which is much faster and cheaper to obtain, but still sufficient to discern genomic differences among individuals within a given species.

Advances in fluorescence microscopy have allowed the possibility to directly map a single DNA molecule. This concept, though straightforward, faces a major challenge that the entropic tendency of polymeric DNA to adopt a coiled conformation must be overcome so as to optically determine the position of specific sequences of interest on the DNA backbone. The ability to control and manipulate the conformation of single DNA molecules, especially, to stretch them into a linear format in a consistent and uniform manner, is thus crucial to the performance of such mapping devices. The focus of this thesis is to develop a reliable single DNA stretching device that can be used in single molecule DNA mapping, and to experimentally probe the fundamental physics that govern DNA deformation.

In the aspect of device design, the strategy we pursue is the use of an elongational electric field with a stagnation point generated in the center of a cross-slot or T channel to stretch DNA molecules. The good compatibility of electric field with small channel dimensions allows us to use micro- or nano-fabricated channels with height on the order of or smaller than the natural size of DNA to keep the molecule always in focus, a feature desirable for any mapping applications. The presence of the stagnation point allows the possibility to dynamically trap and stretch single DNA molecules. This trapping capability ensures uniform stretching within a sample ensemble, and also allows prolonged imaging time to obtain accurate detection results.

We primarily investigate the effects of channel height on the stretching process, specifically, we seek the possibility of utilizing slit-like nanoconfinement to aid DNA stretching. Although extensive previous studies have demonstrated that geometric confinement of DNA can substantially alter the conformation and dynamics of these molecules at equilibrium, no direct studies of this non-equilibrium stretching process in confinement exist prior to the work presented in this thesis. We find that slit-like confinement indeed facilitates DNA stretching by reducing the deformation rate required to achieve a certain extension. However, due to the fact that the steric interactions between the DNA and the confining walls vanish at large extensions, highly stretched DNA under confinement behaves qualitatively similar to unconfined DNA except with screened hydrodynamic interactions, and a new time scale arises that should be used to describe the large change in extension with applied deformation rate. In a consecutive study, we examine the low-extension stretching process and observe a strongly modified coil-stretch transition characterized by two distinct critical deformation rates for DNA in confinement, different from the unconfined case where a single critical deformation rate exists. With kinetic theory modeling, we demonstrate that the two-stage coil-stretch transition in confinement is induced by a modified spring force law, which is essentially related to the extension-dependent steric interactions between DNA and the confining walls.

We also study aspects of the equilibrium conformation and dynamics of DNA in slit-like confinement in order to provide insight into regimes where existing studies show inconsistent results. We use both experiments and simulations to demonstrate that the in-plane radius of gyration and the 3D radius of gyration of DNA behaves differently in weak confinement. In strong confinement, we do not identify any evident change in the scalings of equilibrium size, diffusivity, and longest relaxation time of the DNA with channel height from the de Gennes regime to the Odijk regime. Although the transition between the de Gennes and Odijk regimes in slit-like confinement still remains an open question, our finding adds more experimental evidence to the side of a continuous transition.

The impact of this thesis will be two-fold. We design a DNA stretching device that is readily applicable to single molecule DNA mapping and establish guidelines for the effective operation of the device. Our fundamental results regarding both the equilibrium and non-equilibrium dynamics of DNA molecules in slit-like confinement will serve as a solid basis for both the design of future devices aiming to exploit confinement to manipulate biopolymers, and more complicated studies of confined polymer physics.

Thesis Supervisor: Patrick S. Doyle
Title: Associate Professor of Chemical Engineering

Acknowledgments

The work presented in this thesis is not the product of one person alone. It would not have been possible without the support and guidance given by many caring people. I deeply appreciate all of the individuals who have contributed directly or indirectly to this work or my graduate experience as a whole. This has truly been a rewarding and memorable endeavor.

I would first like to thank my thesis advisor Professor Patrick Doyle for providing me consistent direction and motivation throughout my Ph.D. studies. Thank you for teaching me how to think critically and scientifically about problems and to always look deeper into the task at hand. Thank you also for keeping me focused and for your patience over these years. I believe all the training I received and skills I learned in the Doyle group at MIT will continue to benefit me in the years to come. I would also like to thank my committee members Professor Gareth McKinley and Professor William Deen. Thank you for consistently showing your support and offering good advices on my research.

I also must extend my thanks to members of the Doyle group for their friendship and academic support. In particular, I owe a large debt of gratitude to Daniel Trahan who entered MIT at the same time as I did. Daniel has not only been an invaluable resource and sounding board whenever I encountered obstacles, especially in the polymer theory aspect, but also directly contributed to my research by performing all the Brownian dynamics simulations presented in this thesis. I also thank Anthony Balducci and Chih-Chen Hsieh for teaching me all the experimental techniques of working with DNA and microscopy, and for helping me establish the basic knowledge of polymer physics. In addition to being my research mentor, Anthony also worked together with me to finish one of the studies with the cross-slot channel. I thank Jeremy Jones who also works on DNA experiments for all the useful discussions we had during the past two years and for helping me with my experiments. Many thanks to Daniel Pregibon, Jason Rich, Priyadarshi Panda, Ki Wan Bong, and Steve Chapin for making being cooped up in the basement not such a bad thing after all. Thank you very much for your friendships and making the environment around here a great one to work in.

I have had the privilege of working with several talented researchers outside MIT who also deserve my gratitude. I'm grateful to Heiko Kuhn from Boston University for teaching me a lot of experimental molecular biology techniques and his contribution in designing schemes to label internal sites of DNA with quantum dots (not presented here). Furthermore, I thank Steve Levy for fabricating all the nanoslits used in the equilibrium dynamics study.

Finally, I would like to thank my girlfriend Lin Jin and my parents for their tremendous support. Lin has given more than I could ask for and I cannot express here my gratitude. Without her, I would not have been able to maintain my sanity through this process. She has been nothing but wonderful and supportive over the past five years and I am truly thankful to have her in my life. I also thank my parents for their unconditional love and support. Though they live afar in China, they never failed to encourage me to do the best that I can, to be proud of my achievements, and to offer unwavering support when I fall short.

This research was funded by NSF Career Grant No. CTS-0239012, U.S. Genomics, and Singapore-MIT Alliance for Research & Technology (SMART).

Table of Contents

Abstract **3**

Chapter 1 Introduction **17**
- 1.1 Motivation . . . 17
  - *1.1.1 Next Generation Single Molecule DNA Mapping* . . . 17
  - *1.1.2 Fundamental Polymer Physics in Confinement* . . . 20
- 1.2 Objectives . . . 22
- 1.3 Overview of Results . . . 22

Chapter 2 Background Science **23**
- 2.1 Structure of DNA . . . 23
- 2.2 General Polymer Physics . . . 25
  - *2.2.1 Equilibrium Conformation of Ideal Chains* . . . 25
  - *2.2.2 Excluded Volume Effects* . . . 29
  - *2.2.3 Entropic Elasticity* . . . 30
  - *2.2.4 Dynamic Behavior of Polymers* . . . 32
- 2.3 Electrokinetic Theories . . . 36
  - *2.3.1 Charge Transport in Electrolyte Solution* . . . 36
  - *2.3.2 Charged Surface and Electric Double Layer* . . . 37

2.3.3 Electroosmosis 39
2.3.4 Electrophoresis 39
2.4 Stretching DNA 42

Chapter 3 Experimental **45**
3.1 Single-Molecule Fluorescent Microscopy 45
3.2 Data Analysis 46
3.3 Channel Fabrications 47
3.4 DNA Sample Preparation 49
3.5 Attaching Quantum Dots to λ-DNA 53

Chapter 4 Stretching DNA in Micro T-channel **57**
4.1 Introduction 57
4.2 DNA Deformation in Electric Fields 58
4.3 Device Geometry 59
4.4 Experiments 61
4.5 Electric Field Characterization 61
4.6 Results and Discussion 64
4.7 Conclusion 65

Chapter 5 Stretching DNA in Slit-like Confinement **67**
5.1 Introduction 67
5.2 Experiments 69
5.2.1 Channel and DNA Preparation 70
5.2.2 Electric Field Characterization 70
5.2.3 Relaxation Time Measurements 72
5.2.4 T4 DNA Stretching Experiments 72
5.3 Results and Discussion 73
5.4 Conclusions 77

Chapter 6 Coil-stretch Transition of DNA in Slit-like Confinement **79**
6.1 Introduction 79
6.2 Experiments 82
6.2.1 Device Geometry 82
6.2.2 Channel and DNA Preparation 83
6.2.3 Electric Field Characterization 83
6.2.4 DNA Stretching Experiments 85
6.3 Dumbbell Model 85
6.3.1 Model Description 85
6.3.2 Spring Force Law in Confinement 87
6.3.3 Predicting Experimental Observables 91
6.4 Results and Discussion 92
6.4.1 Steady-state Extension 92
6.4.2 Extension Fluctuations 92
6.4.3 Molecular Orientation in the Extensional Electric Field 94
6.4.4 Force Balance and Effective Conformational Energy 94

6.5 Conclusions 97

Chapter 7 Equilibrium Dynamics of DNA in Strong Slit-like Confinement 99
7.1 Introduction 99
7.2 Scaling Arguments for Polymer Dynamics in Nanoslits 102
  7.2.1 Moderate Confinement: $p \ll h < R_{g,\mathrm{bulk}}$ 102
  7.2.2 Strong Confinement: $h < p$ 103
7.3 Experiments 104
  7.3.1 Channel and DNA Preparation 104
  7.3.2 Experimental Procedure 105
  7.3.3 Data Analysis 105
  7.3.4 Effects of Photobleaching 107
  7.3.5 Point Spread Function (PSF) 107
7.4 Brownian Dynamics Simulations 109
7.5 Results and Discussion 111
  7.5.1 Conformation of DNA in Nanoslit 111
  7.5.2 Measuring the Longest Relaxation Time of DNA 115
  7.5.3 Static and Dynamic Scalings vs Channel Height 115
  7.5.4 Comparison with Previous Results 118
7.6 Conclusion 121

Chapter 8 Conclusions and Outlook 123

Appendix A Appendices 127
A.1 T4 DNA Relaxation Time 127
A.2 Brownian Dynamics Simulations 128
  A.2.1 Bead-spring Chain Model 128
  A.2.2 Parameters 130
  A.2.3 Results 130
A.3 Dumbbell Model with Extension-dependent Drag Coefficient 132

Bibliography 139

List of Figures

1.1 Schematic of the process of direct linear analysis (DLA). 18
1.2 Schematic examples of methods to stretch single DNA molecules. 19

2.1 The double helix structure of double stranded DNA. 24
2.2 Schematics of a Rouse polymer (no hydrodynamic interactions) and a Zimm polymer with hydrodynamic interactions. 35
2.3 Schematics of the structure of the double layer near a negatively charged surface, and the corresponding profile of the electric potential. 38
2.4 Schematic of the electroosmosis velocity profile near a flat, negatively charged surface. 39
2.5 Schematic of a negatively charged spherical particle during electrophoresis. 40
2.6 Schematic of the dumbbell model used in the stretching analysis, the flow velocity profile is drawn in the dumbbell frame of reference. 43

3.1 Schematic of the microscope setup. 46
3.2 Examples of the raw and processed images of λ-DNA in nanoslits. 46
3.3 Schematic illustration of fabrication techniques. 48
3.4 Schematic of using streptavidin coated quantum dot to label λ-DNA termini and sample image of an end-labeled λ-DNA molecule. 55

4.1 Schematic diagrams of channel geometry, location of uniform/elongational electric fields, and stagnation point. 59
4.2 Results of finite element calculation of the electric field in the T-junction. 60
4.3 Trajectories of λ-DNA electrophoresis for electric field characterization. 62
4.4 Stretching and trapping of T4 DNA in the T channel and the mean steady state fractional extension of T4 DNA versus De. 63
4.5 Stretching of a λ DNA 10-mer in the T channel. 64

5.1 Schematic of the low extension relaxation time (τ_{II}) and the higher extension relaxation time (τ_{I}) of DNA in slit-like nanochannels and the possibility of their importance in DNA stretching. 69
5.2 Diagrams of the cross-slot stretching device geometry and experimental results of tracking the planar elongational electric field in the center region of the device. . . . 71
5.3 Individual traces and ensemble averages of the fractional extension of DNA molecule versus strain for $\mathrm{De}_{\mathrm{I}} = 1$ in a 300 nm tall channel. Snapshots of individual DNA images at steady state at different values of De_{I} are also shown. 73
5.4 Ensemble average steady state extension versus dimensional and non-dimensional measures of the strength of the deformation applied. 74
5.5 Root-mean-square angle of the principal axis of the radius of gyration relative to the x-axis (θ_{RMS}, in degrees) versus strain for several different values of $\mathrm{De}_{\mathrm{II}}$ for all three channels. 76

6.1 Schematics of the DNA stretching process in slit-like nanochannels and a comparison of the effective spring force law for DNA in confinement and in bulk. 81
6.2 Schematics of the cross-slot stretching device geometry, the motion and stretching of DNA molecules in the device, and the setup of the Brownian dumbbell model in a planar homogeneous extensional electric field. 84
6.3 Experimental confirmation of planar elongational deformation in the center region of the 300 nm device by tracking λ-DNA molecules. 86
6.4 Experimental relaxation data and relaxation of the dumbbell model with the extracted spring constant. The extracted spring constant and the corresponding dumbbell spring force as a function of the dumbbell end-to-end distance. 90
6.5 Experimental results and the dumbbell model predictions of the steady-state DNA behaviors. 93
6.6 Comparison between the stretching force exerted on a dumbbell with $\theta = 0$ at the critical De_{I} and the dumbbell spring force, and the effective conformational energy ($E/k_{\mathrm{B}}T$) of the dumbbell as a function of X at different values of De_{I}. 95

7.1 Snap shots of λ-DNA molecules confined in the 2 μm, 247 nm, and 32 nm tall nanoslits. 105
7.2 Summary of image analysis for λ-DNA in a 90 nm tall slit in the 1.5×TBE buffer. . 108
7.3 Typical image of a 50 nm fluorescent polystyrene bead under a 100× NA 1.4 objective and the corresponding 2D fluorescence intensity profile. 109
7.4 Dependence of different measurements of the DNA conformation on slit height h. . . 112
7.5 A comparison of the in-plane radius of gyration $R_{\|}$ of λ-DNA evaluated using different methods. 113

7.6 Curves of the rotational autocorrelation function C_r and the stretch autocorrelation function C_s versus the lag time δt for the 247 nm and 32 nm tall slits measured in the 1.5×TBE buffer. 114
7.7 Dynamic properties of λ-DNA measured in both the 1.5×TBE buffer and the TE buffer as functions of the slit height h. 116
7.8 Comparison of the static and dynamic properties of λ-DNA in slit-like channels measured from the current and several previous studies. 120

A.1 Comparison of the probability distribution of the equilibrium maximum extension between experiments and the BD simulation of the bead-spring chain. 131
A.2 Histograms of the the maximum extension distribution of the bead-spring chain at various values of end-to-end distance for the 150 nm tall channel case. 133
A.3 Values of the three fitting parameters in Equation A.12 as a function of the dimensionless end-to-end distance X determined from simulation data. 134
A.4 Comparison between the dumbbell model prediction of the average dumbbell end-to-end distance and the average maximum extension, and comparison between the dumbbell model prediction of the standard deviation of the end-to-end distance and that of the maximum extension. 135
A.5 Average steady-state fractional end-to-end distance and the standard deviation of the fractional end-to-end distance as functions of the Deborah number calculated using Equation A.20 and Equation A.21, respectively. 137

List of Tables

3.1 Sequences for the two overhangs of λ-DNA and the biotinylated oligonucleotides (Biotin-side-A and Biotin-side-B). 53

5.1 Channel dimensions and T4 DNA relaxation times. 72

6.1 Channel dimensions and T4 DNA relaxation times. 85

7.1 Summary of experimental conditions of several different studies. "BME" stands for β-mercaptoethanol and "Glox" stands for the anti-oxygen system of glucose, glucose oxidase and catalase. 118

A.1 Comparison of T4 DNA relaxation times measured in chapter 5 and chapter 6. . . . 127
A.2 Comparison of the T4 DNA relaxation times scaled to 1 cP. 128

CHAPTER 1

Introduction

1.1 Motivation

1.1.1 Next Generation Single Molecule DNA Mapping

It is well known that the base pair sequence of DNA molecules stores the most essential information for the development and functioning of all known living organisms and some viruses. Since early 1980's, enormous effort has been spent on developing technologies to determine the exact sequence of these basepairs of a representative human [1] and other mammalian species [2,3]. The accumulated knowledge has been extremely beneficial and inspired a variety of biomedical research as well as genomic applications. However, genomes from a much greater number of individuals are yet to be studied in order to fully understand genome variation, genetic susceptibility to disease, and pharmacogenomics of drug response [4]. The challenges faced by current state-of-the-art sequencing technologies are the large timescale and cost required to analyze an individual sample. Consequently, alternative strategies that can more rapidly characterize a genome must be developed to facilitate or even replace some of the current methods.

In fact, performing a single-base resolution sequencing of the genome might be excessive for the investigation of genome diversity, as the genomic differences among individuals within a given species (e.g., humans) can usually be discerned with a much coarser-scale (~kbp) information of the sequence [5]. Acquiring such a coarse-scale resolution of the genome is termed DNA mapping where the location of different short base pair sequences or genes relative to one another is of interest.

Mapping is much faster and cheaper to perform for an individual sample, and hence can drastically accelerate the process of identifying differences among genomes. In addition, the resolution provided by DNA mapping will also be sufficient for many comparative genomic applications such as crime investigation, food safety, breast cancer diagnostics, and pathogen identification [4, 5].

Currently, the most commonly used mapping approach is restriction mapping [6]. It is performed by cleaving DNA at specific sites using restriction enzymes which recognize a ~4-8 base length region of DNA. The size distributions of the resulting fragments are then determined using pulsed-field gel electrophoresis. This method is slow (~24 hours) [7], cumbersome and not easily automated [6]. Furthermore, the method loses information regarding the ordering of the fragments, requiring the use of multiple enzymes and complicated algorithms to construct the correct map [4]. DNA amplification is also a required step to produce enough detection signal in this bulk method. Due to these limitations, many studies have been carried out to develop alternative mapping technologies over the past several years.

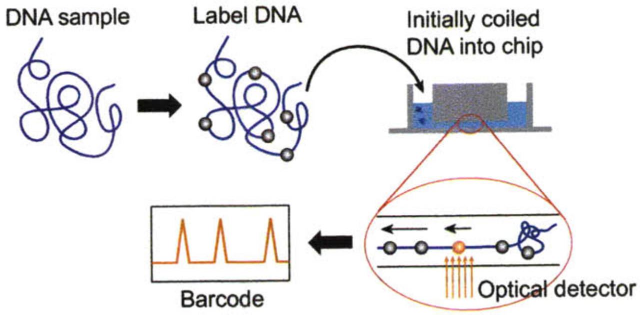

Fig. 1.1: *Schematic of the process of direct linear analysis (DLA).*

Advances in fluorescence microscopy have allowed the possibility to directly map a single DNA molecule. This concept was first described by Schwartz and coworkers [8, 9] where they stretched individual DNA molecules and then observed the specific locations at which restriction enzymes cut the DNA. Comparing to restriction mapping, the single molecule approach can greatly reduce the reagent costs as no amplification is required for the analysis. More importantly, this process is considerably faster because the physical ordering of fragments is preserved and thus there is no need for complex re-assembly of map information. Since the study of Schwartz et al., a variety of single molecule DNA mapping methods have been put explored [10, 11, 12, 13, 14, 15, 16, 17], among which one particular strategy named direct linear analysis (DLA) [11] has gained significant attention. In direct linear analysis, the DNA is first selectively tagged with fluorescent probes and then stretched into a linear optically readable "barcode" (see Figure 1.1). The resulting DNA construct is either directly imaged [9] or sent pass an optical scanner [11] to measure the physical distances between probes along the contour of the DNA. The use of sequence-specific tags that can stably attach to DNA make direct linear analysis more straightforward than the restriction enzyme approach, which is limited in both resolution and speed as one must wait for the enzyme to diffuse in and cut the DNA. There has been significant work using proteins [10, 17], short DNA segments [14,18], or peptide nucleic acid (PNA) [11] that are chemically linked to small fluorophores or fluorescent nanoparticles to mark specific loci on DNA, and a lot more studies are currently devoted to designing new ways to label DNA. On the other hand, the major challenge, and the one germane to the current thesis, is to controllably stretch the DNA far from its equilibrium coiled conformation so as to determine the linear distance between probes on the DNA backbone. Therefore, interest in direct linear analysis has inspired investigations into methods of conformation control of single DNA molecules.

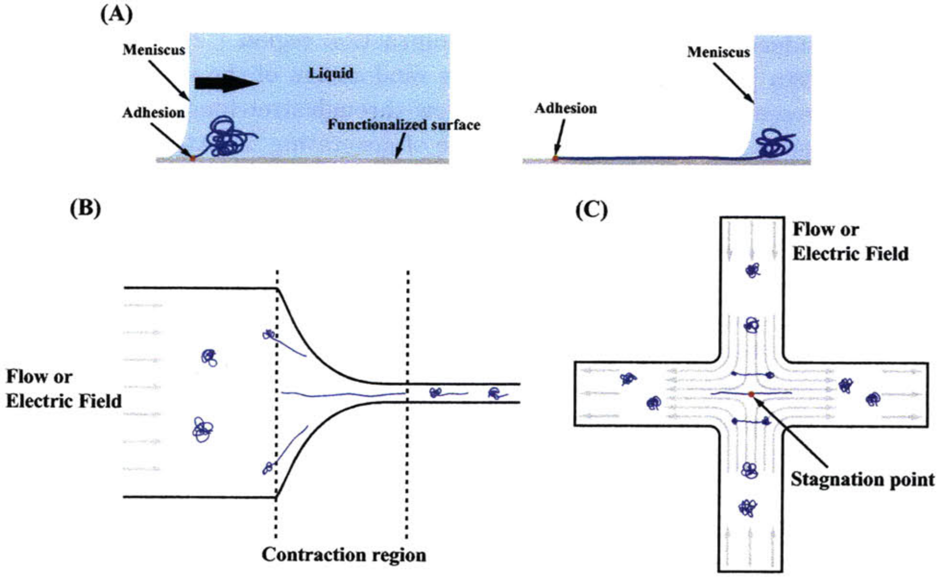

Fig. 1.2: *Schematic examples of methods to stretch single DNA molecules. (A) DNA combing. One end of the DNA is anchored to a functionalized surface and the meniscus moves across the anchoring point to stretch the DNA. (B) Flow through funnel. DNA molecules are stretched when they pass through the contraction, once they exit the contraction region they relax back into a coiled state. (C) Cross-slot channel. DNA molecules are trapped and stretched at the stagnation point.*

Currently, the most mature DNA stretching technique is DNA combing which involves absorbing and stretching DNA on functionalized surfaces using flow [14,15,19,20] or a receding meniscus [21, 22,23,24] (see Figure 1.2A). While large numbers of DNA can be attached to a surface and stretched in this manner, placement of DNA on the surface is random and prone to surface defects as well as nonspecific absorption. DNA combing also does not provide precise control over the magnitude of stretching force exerted on the DNA and thus often results in overstretching or even fragmentation of large DNA molecules [22]. Alternatively, confinement of DNA in circular or square nanochannels can be used to alter the equilibrium DNA conformation to a more linear format [13,16,25]. While this approach has much promise, the small channel features are often expensive to fabricate and are as well very sensitive to surface defects. Another strategy for stretching DNA is to use non-uniform hydrodynamic flows [11,12,17,26,27,28,29,30] or electric fields [31,32,33]. In this case the DNA molecule is extended due to the flow (or electric field) gradients that vary over the length scale of the molecule. The non-uniform flow (or electric) fields are usually created by using fluidic channels with specifically designed geometry. The precise knowledge regarding the flow (or electric field) kinematics allows the stretching process to be well controlled. So far two major types of fluidic channels have been explored. The first is the flow-through funnels (see Figure 1.2B) which were first proposed by Austin and coworkers [34] and have been investigated for some time both at the company U.S. Genomics [11, 12, 30] and in our group [32, 33, 35, 36]. This device can lead to high throughput, but suffer from incomplete and non-homogeneous DNA stretching due to the finite residence time of DNA in the contraction region [32]. This behavior, termed molecular individualism [37], results from the large randomness of the initial configuration of the DNA polymer and presents a unique challenge for flow-through stretching devices. The second type of device is the cross-slot channels that are capable of generating an extensional flow (or electric) field with a stagnation point (see Figure 1.2C) [26]. The stagnation point can be used to trap a DNA molecule [28] within the extensional field so as to provide sufficient residence time until the molecule reaches steady-state. Trapping of the DNA provides a direct solution to molecular individualism although it significantly reduces the throughput of the device. Nevertheless, considering the uniform ensemble extension that can be attained and the fact that the imaging of a trapped DNA is more precise and simple than that of a rapidly moving molecule, the cross-slot channels should not require as many individual samples as that for a flow-through system.

Although analogies exist between the deformation of a DNA molecule in non-uniform hydrodynamic flows and that in non-uniform electric fields [38], the hydrodynamic flow approach has several drawbacks with respect to DNA mapping, primarily due to its incompatibility with small channel dimensions. Direct linear analysis prefers thin channels (less than 1 μm) as they can keep DNA always in focus, and as we will see in later chapters, confinement of DNA naturally makes the molecule easier to stretch. However, pressure driven flow is extremely difficult to control at small length scales, and thus the depth of most existing hydrodynamic stretching devices is much larger than the size of a single DNA molecule [17, 28], resulting in a large fluorescent background (many out of focus molecules) and molecules that initially sit in the imaging plane frequently go out of focus. Furthermore, the shear that arises near any surfaces in hydrodynamic flows due to the no-slip condition usually lead to unstable motions or even breakage of the DNA [39]. In contrast, stretching DNA with electric field is ideal for mapping applications because electric field scales well to thin channels and are relatively easy to impose compared to pressure driven flows. At length scales much larger than the Debye length, electric field does not have any rotational component and thus does not result in shearing of the DNA [40].

To summarize, the development of next generation single molecule DNA mapping techniques, especially direct linear analysis (DLA), can greatly speed up the characterization of genome diversity and inspire novel genomic applications. In this thesis we will pursue the combination of electric field gradients and micro- or nano-fluidic channels to build a DLA device. As the performance of such devices relies strongly on the ability to uniformly stretch DNA in a sample ensemble, it is important to understand the fundamental physics that govern DNA deformation in electric field gradients and under confinement.

1.1.2 Fundamental Polymer Physics in Confinement

Beside their fundamental biological role as carriers of genetic information, double-stranded DNA molecules have also served as an ideal model polymer system for the experimental investigation of polymer physics [41, 42]. With the recent advance of nanofabrication technology, fluidic channels with well-defined dimensions that are smaller than typical DNA molecules can now be readily constructed. These small-scale devices have provided an unprecedented opportunity to directly examine polymer behavior under geometric confinement. The major motivation for studying confined polymer physics is provided by the capability of confinement to substantially alter the conformation and dynamics of polymer chains [43,44,45,46]. Such unique nature of confinement has established the basis of various novel technologies that promise inexpensive and more efficient methods for the separation and analysis of DNA [16,47,48]. In addition to application driven interests, a detailed understanding of confined polymer physics also provides better insight into many fundamental biological problems including chromosome segregation in bacteria [49], DNA packaging in viral phages [50], and the expression of genes based on chromatin conformation [51].

Although scaling theories for the properties of polymers under confinement have been proposed since late 1970's [43,44,45,46,52,53], they have only recently begun to be experimentally tested in well-defined geometries. Broadly speaking, two major types of confinement geometry have been put explored: tube-like confinement and slit-like confinement. Tube-like confinement is defined when a polymer is placed in a tube with diameter smaller than its natural size ($R_{g,\mathrm{bulk}}$). In reality, this type of confinement is usually realized with a square or rectangular channel with both its height (h) and width (d) smaller than $R_{g,\mathrm{bulk}}$. Similarly, slit-like confinement is defined when a polymer is confined between two parallel plates separated by height $h < R_{g,\mathrm{bulk}}$ and it is experimentally realized with a high aspect ratio rectangular channel. The tube-like geometry is the most widely studied confinement geometry to date, most probably because of its application to DNA mapping as discussed in the previous section. Slit-like micro- and nano-channels have recently received more and more attention as they are not only an interesting new confinement geometry but also hold special interest for the development of lab-on-chip bioseparation devices [54].

Several previous studies from our group [55,56,57,58] and others [59,60,61,62,63] have probed equilibrium polymer dynamics in slit-like confinement using single molecule DNA experiments. These studies have provided a sound understanding of the equilibrium conformation as well as transport coefficients (diffusivity, relaxation time, etc.) of single DNA molecules in moderate confinement, $p < h < R_{g,\mathrm{bulk}}$, where p is the DNA persistence length. However, for equilibrium dynamics in both weak confinement ($h \sim R_{g,\mathrm{bulk}}$) and strong confinement ($h < p$), existing results are currently somewhat contradictory [64], and a clear picture regarding polymer behavior in these two regimes of confinement is yet to be established. Non-equilibrium dynamics of DNA confined in slits are even less well studied and understood. Two quantitative studies [65,66] have so far probed the relaxation of initially stretched DNA back to equilibrium in slit-like confinement. It was shown that while the equilibrium states of confined and unconfined DNA are very different, highly deformed DNA molecules confined in slits behave qualitatively similar to unconfined DNA except with screened hydrodynamic interactions. This unique conformation-dependent behavior of confined polymer suggests a strong possibility that confinement can dramatically affect the coil-stretch transition process. While the coil-stretch transition of unconfined DNA has been been extensively studied over the past 20 years [26,27,28,29,67], there are no direct and/or systematic investigations of this non-equilibrium process in confinement prior to the work presented in this thesis. In a word, despite the fast progress made toward the understanding of confined polymer physics, there is still a wealth of open areas that remain unexplored or require more detailed characterization. This thesis will attempt to provide insight into some of these problems.

1.2 Objectives

The goal of the following research is to design micro- and nano-fluidic DNA stretching devices that can be used in direct linear analysis and to build a sound fundamental foundation for the use of confinement in the manipulation and conformational control of single DNA molecules. Our focus will be on DNA deformation in electric field gradients and DNA dynamics (both when the molecule is at equilibrium and when it is highly deformed) in slit-like confinement. For our experiments, we will construct both microscale PDMS (polydimethylsiloxane) channels and nanoscale glass channels with custom geometry, and fluorescence microscopy to track single molecules of DNA in these devices. An overall theme of this thesis is:

- Design of micro- and nano-channels for single molecule DNA stretching.
- Investigation of non-equilibrium dynamics of DNA in slit-like confinement.
- Investigation of equilibrium dynamics of DNA in slit-like confinement with specific focus on regimes of weak confinement and strong confinement.

1.3 Overview of Results

In chapter 2, we present a background of unconfined polymer physics, polymer deformation, confinement theory, and electrokinetic theory to provide the very general foundation upon which we build our experimental results. Chapter 3 provides a detailed description of our experimental methods and procedures. Chapter 4 introduces the design of a microscale T channel that is capable of trapping and stretching single DNA molecules. The focus in this chapter is to demonstrate the general concept and feasibility of using a planar elongational electric field with a stagnation point to effectively trap and stretch DNA. Chapter 5 presents the first detailed experimental investigation of DNA stretching in slit-like confinement. We demonstrate the capability of confinement to facilitate the stretching of single DNA molecules and identify the correct time scale that should be used to predict the deformation rate required to achieve a certain DNA extension. Chapter 6 presents the results of a consecutive study where the coil-stretch transition process in slit-like confinement is characterized in details. Here, with both single molecule DNA experiments and kinetic theory modeling, we find that the coil-stretch process of confined DNA becomes quantitatively different and is characterized by two distinct critical strain rates while in the unconfined case a single critical strain rate exists. Chapter 7 investigates the equilibrium conformation and dynamics of DNA under weak ($h \sim R_{g,\mathrm{bulk}}$) and strong ($h < p$) slit-like confinement where existing studies show inconsistent results. Chapter 8 summarizes commentary of the impact of this research on the field, as well as future directions for research concerning deformation and confinement.

CHAPTER 2

Background Science

This chapter reviews the essential background science to understand polymer conformation and dynamics as well as DNA motion and deformation in electric field gradients. Specifically, we will introduce:

- Chemical structure of DNA
- General Polymer Physics describing both the static and dynamic properties of unconfined polymer at equilibrium
- Electrokinetic theories
- Stretching DNA in non-uniform hydrodynamic flows or electric fields

2.1 Structure of DNA

Large DNA molecules are linear polymers (i.e., molecules consisting of many elementary and often structural repeating units) specialized for the storage and transmission of information. A single DNA strand is composed of monomers called nucleotides, each of which consists of a sugar (deoxyribose), a phosphate group, and a nitrogenous base – adenine (A), guanine (G), cytosine (C), or thymine (T). These nucleotides are connected in a unique sequence by the phosphodiester linkage between the sugar of one nucleotide and the phosphate of the next to form a single stranded DNA (ssDNA) chain. In a double-stranded DNA (dsDNA), two single strands are held together antiparallely by hydrogen bonding between specifically paired bases (A to T and G to C) to form up the famous double helix structure (Figure 2.1). Because the AT and GC pairs are of equal length and fit identically into the double helix, the diameter of the helix is uniform (~2 nm).

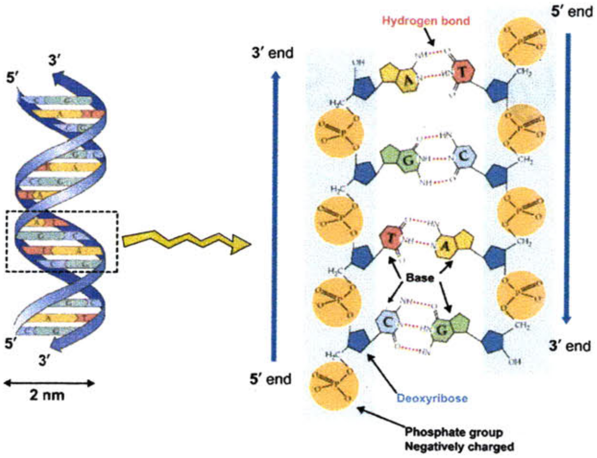

Fig. 2.1: *The double helix structure of double stranded DNA. Drawings taken and modified from http://bcs.whfreeman.com/thelifewire/default.asp.*

Despite the distinct chemical structure of the four nucleotides, the *physical* properties of a long DNA generally do not depend strongly on the particular nucleotide sequence it carries and can be modeled with classical polymer models. However, the double-helix backbone does make dsDNA unique among synthetic polymers: it is much stiffer than common linear industrial polymers (e.g., polystyrene). This stiffness is characterized by the persistence length (p), a characteristic length scale over which the polymer appears to be locally straight. The persistence length of dsDNA is considerably larger ($\sim 50\,\mathrm{nm}$) than it is for common industrial polymers ($\sim 1\,\mathrm{nm}$). In addition, as will be discussed below, a larger persistence length also corresponds to a larger equilibrium coil size ($R_{g,\mathrm{bulk}}$) given the same contour length (L_c). For genomic length DNA (kbp-Mbp), this coil size is large enough to be routinely observable with optical microscopy, making it an ideal model polymer for experimental studies. Another important property of DNA is that it is strongly charged under moderate pH as each phosphate group in the backbone can carry a negative charge. These charges can result in electrostatic repulsions between nucleotides and thus local stiffening of the backbone. However, in the typical biological environment of DNA, these electrostatic interactions decay over a very small length scales due to the high salt concentration, and consequently do not contribute significantly to the stiffness of the DNA. Finally, we note that the charged nature of DNA allows one to use electric fields or electric field gradients to manipulate DNA molecule, a technique widely used in genomic studies.

2.2 General Polymer Physics

In this section we review the general polymer physics to quantitatively model the conformation and dynamics of a single, unconfined DNA in aqueous solutions. The analysis presented follows closely that of Rubenstein and Colby [68] chapters 2 and 3, and Doi and Edwards [69] chapters 2 and 4.

2.2.1 Equilibrium Conformation of Ideal Chains

The equilibrium state of a thermodynamic system is determined when the system has maximum entropy S and minimum free energy A. The entropy of a system at a given state is equal to $k_B \ln \Omega$ where k_B is the Boltzmann constant and Ω is the number of ways that the molecules can occupy the given state, and a system tends to reside in the state where the maximum number of configurations can be achieved. As a result, a polymer at equilibrium in solution adopts a coiled configuration at which it has the largest conformational freedom. The size of the coil can be described by three variables: the contour length L_c of the chain, the persistence length p (flexibility), and the quality of the solvent, a description of monomer-solvent interactions. There are three possibilities in terms of solvent qualities: 1, a poor solvent in which monomers would rather be near each other than in contact with surrounding solvent, 2, a good solvent in which the monomer tend to avoid each other, and 3, a theta solvent in which monomer-monomer interactions and monomer-solvent interactions are equally favored. In this section we will first neglect these interactions and focus on the case of an ideal polymer chain. The effects of solvent quality on the equilibrium conformation of a polymer chain will be discussed in section 2.2.2.

Ideal Chain Models

The simplest model of an ideal chain is a series of n rigid rods (modeling the chemical bonds between monomers) with equal length and connected at joints in which we incorporate information about the monomer chemistry. It is assumed that there are no net interactions between monomers separated by a sufficiently large distance along the chain and thus the chain contour can pass through itself. Let $\mathbf{r}_i$ denote the bond vector going from joint i to joint $i+1$ $(1 \leq i \leq n)$, the end-to-end vector of the chain is given by

$$\mathbf{R} = \sum_{i=1}^{n} \mathbf{r}_i \tag{2.1}$$

The ensemble average end-to-end vector is related to the isotropy of the chain, and as for an ideal chain there is no preferred orientation of individual bonds, its average end-to-end vector is zero:

$$\langle \mathbf{R} \rangle = \mathbf{0} \tag{2.2}$$

The mean-square end-to-end distance provides information regarding the coil size and is given by

$$\langle R^2 \rangle = \langle \mathbf{R} \cdot \mathbf{R} \rangle = \left\langle \left(\sum_{i=1}^{n} \mathbf{r}_i \right) \cdot \left(\sum_{i=1}^{n} \mathbf{r}_i \right) \right\rangle = \sum_{i=1}^{n} \sum_{j=1}^{n} \langle \mathbf{r}_i \cdot \mathbf{r}_j \rangle = l^2 \sum_{i=1}^{n} \sum_{j=1}^{n} \langle \cos \theta_{ij} \rangle \tag{2.3}$$

where $l = |\mathrm{r}_i|$ is the bond length and θ_{ij} is the angle between bond vector r_i and r_j.

The value of $\langle \cos\theta_{ij} \rangle$ in Equation 2.3 depends on the local flexibility (usually determined by local chemical structure) of the chain. In the limit of an extremely flexible polymer (i.e., the freely jointed chain model), there is no correlation between the direction of even successive bonds along the backbone, $\langle \cos\theta_{ij} \rangle = 0$ for $i \neq j$, and thus the mean-square end-to-end distance is simply given by:

$$\langle R^2 \rangle = nl^2 \tag{2.4}$$

The root-mean-square end-to-end distance is then $R_{\mathrm{RMS}} = \sqrt{\langle R^2 \rangle} = n^{1/2}l = n^{-1/2}L_c$. This characteristic length of the equilibrium polymer coil is much smaller than the chain's contour length, $R_{\mathrm{RMS}} \ll L_c$, especially for long polymer chains (large n).

In reality, however, the directions of bond vectors especially the neighboring ones are usually correlated and $\langle \cos\theta_{ij} \rangle \neq 0$. But for an ideal chain, these correlations are only important for small separations of bond vectors and die out with distance along the chain, $\langle \cos\theta_{ij} \rangle \to 0$ as $|i-j| \to \infty$. In fact, it can be shown that the sum in Equation 2.3 converges and the consequence of the correlations between bond vectors is simply to increase the mean-square end-to-end distance by a constant C_n ($C_n > 1$) comparing to the result in Equation 2.4, $\langle R^2 \rangle = C_n N l^2$, where the coefficient C_n is called Flory's characteristic ratio. The characteristic ratio increases with n and saturates at a finite value C_∞ for large number of bonds ($n \to \infty$). As a result, the mean-square end-to-end distance can be approximated for long chains

$$\langle R^2 \rangle \approx C_\infty n l^2 \tag{2.5}$$

Given the similarity between the result of Equation 2.5 and that for a freely jointed chain, it is convenient to rescale the chain in terms of N "effective" freely jointed bonds of length b, the Kuhn length, such that Equation 2.5 can be rewritten as $\langle R^2 \rangle = Nb^2$. As the contour length of the chain is constant $L_c = Nb = nl$, we have

$$N = \frac{L_c^2}{C_\infty n l^2} \tag{2.6}$$

$$b = \frac{C_\infty n l^2}{L_c} \tag{2.7}$$

Now we introduce polymer models that take into account of the local correlations between bond vectors. The simplest model to incorporate such correlations is the freely rotating chain in which all angles between neighboring bonds are assumed to be fixed at a constant $\theta_{i,i+1} = \theta$, and the $i + 1^{\mathrm{th}}$ bond is allowed to rotate along the axis of the ith bond. In this model, the average angle between the ith and j^{th} bond vector is given by

$$\langle \cos\theta_{ij} \rangle = (\cos\theta)^{|j-i|} \tag{2.8}$$

Considering the fast decay of $(\cos\theta)^{|j-i|}$ with increasing separation of the two bond vectors, the above equation can be rewritten as

$$\langle \cos\theta_{ij} \rangle = \exp[|j-i| \ln(\cos\theta)] = \exp\left[-\frac{|j-i|}{s_{\mathrm{p}}}\right] \tag{2.9}$$

where

$$s_{\mathrm{p}} = -\frac{1}{\ln(\cos\theta)} \tag{2.10}$$

is the number of segments over which the chain persists in one direction, which is the characteristic scale at which local correlations between bond vectors decay. The mean-square end-to-end distance of the freely rotating chain can now be written as

$$\begin{aligned}\langle R^2\rangle &= \sum_{i=1}^{n}\sum_{j=1}^{n}\langle \mathbf{r}_i\cdot\mathbf{r}_j\rangle = \sum_{i=1}^{n}\langle r_i^2\rangle + l^2\sum_{i=1}^{n}\left(\sum_{k=1}^{i-1}\cos^k\theta + \sum_{k=1}^{n-i}\cos^k\theta\right)\\ &\approx nl^2 + 2n\sum_{k=1}^{\infty}\cos^k\theta = nl^2\frac{1+\cos\theta}{1-\cos\theta}\end{aligned} \tag{2.11}$$

As a result, the Flory characteristic ratio of the freely rotating chain is

$$C_\infty = \frac{1+\cos\theta}{1-\cos\theta} \tag{2.12}$$

For very stiff polymers such as double-stranded DNA, the bond angle is small ($\theta \ll 1$) such that $\cos\theta \approx 1-\theta^2/2$ and the quantity s_{p} can be rewritten as

$$s_{\mathrm{p}} \approx -\frac{1}{\ln(1-\theta^2/2)} \approx \frac{2}{\theta^2} \tag{2.13}$$

where the approximation $\ln(1-x) \approx -x$ is used for small x. The persistence length of the chain, defined as the characteristic length of the segment that remains straight, is given by

$$p = s_{\mathrm{p}} l = l\frac{2}{\theta^2} \tag{2.14}$$

The Flory characteristic ratio of the chain is

$$C_\infty = \frac{1+\cos\theta}{1-\cos\theta} \approx \frac{2-\theta^2/2}{\theta^2/2} \approx \frac{4}{\theta^2} \tag{2.15}$$

and the corresponding Kuhn length is twice the persistence length

$$b = \frac{C_\infty n l^2}{L_c} \approx l\frac{4}{\theta^2} = 2p \tag{2.16}$$

At the limit of $l \to 0$ and $\theta \to 0$ while both the persistence length p and contour length L_c of the chain are kept constant, the polymer becomes a worm-like chain which can also be viewed as a continuous thread with a bending potential. At this continuous limit, the mean-square end-to-end distance can be evaluated using

$$\begin{aligned}\langle R^2\rangle &= \int_0^{L_c}\int_0^{L_c}(\cos\theta)^{|u-v|/l}\,du\,dv = \int_0^{L_c}\int_0^{L_c}\exp\left(-\frac{u-v}{p}\right)du\,dv\\ &= 2pL_c - 2p^2\left[1-\exp\left(-\frac{L_c}{p}\right)\right]\end{aligned} \tag{2.17}$$

The DNA molecules that are of direct interest to this thesis are always much longer than their persistence length $L_c \gg p$. At this limit Equation 2.17 can be reduced to $\langle R^2 \rangle \approx 2pL_c = Nb^2$, suggesting that the static configuration of a long worm-like chain with a persistence length p can be thought of as a freely jointed chain with equal contour length and a Kuhn length $b = 2p$.

All the ideal chain models presented above use the end-to-end distance to quantify the size of the equilibrium coil. This quantity, however, is not experimentally measurable because the two endpoints of a linear polymer are difficult to observe and cannot be distinguished from the cloud of monomers. Instead, in the light scattering experiments [68, 69] and single molecule fluorescence microscopy experiments [70], an alternative characteristic size of the equilibrium polymer called the radius of gyration $R_{g,\text{bulk}}$ (the subscript "bulk" is used to denote the chain is not confined) is measured. The squared radius of gyration is defined as the second moment of the distribution of monomers around the center of mass of the polymer:

$$R^2_{g,\text{bulk}} = \frac{1}{N}\sum_{i=1}^{N}(\mathbf{x}_i - \mathbf{x}_{\text{com}})^2 \tag{2.18}$$

where $\mathbf{x}_i$ is the position vector of the ith monomer, the center of mass position $\mathbf{x}_{\text{com}}$ is defined as

$$\mathbf{x}_{\text{com}} = \frac{1}{N}\sum_{i=1}^{N}\mathbf{x}_i \tag{2.19}$$

The mean-square radius of gyration is then given by

$$\langle R^2_{g,\text{bulk}} \rangle = \frac{1}{N^2}\sum_{i=1}^{N}\sum_{j=i}^{N}\langle(\mathbf{x}_i - \mathbf{x}_j)^2\rangle \tag{2.20}$$

For an ideal linear chain, the mean-square radius of gyration is proportional to the mean-square end-to-end distance with a constant numerical factor, $\langle R^2_{g,\text{bulk}} \rangle = \langle R^2 \rangle/6$. Thus, the experimentally measured the radius of gyration can be used to infer the behavior of the chain's end-to-end distance.

Free Energy of an Ideal Chain

Based on the statistics of a 3D Gaussian random walk, the probability distribution function for the end-to-end vector $\mathbf{R}$ of an ideal chain with N Kuhn steps can be derived:

$$P(N, \mathbf{R}) = \left(\frac{3}{2\pi Nb^2}\right)^{3/2} \exp\left(-\frac{3\mathbf{R}^2}{2Nb^2}\right) \tag{2.21}$$

The probability distribution function $P(N, \mathbf{R})$ is directly related to the number of possible conformations of the chain, $\Omega(N, \mathbf{R})$:

$$P(N, \mathbf{R}) = \frac{\Omega(N, \mathbf{R})}{\int \Omega(N, \mathbf{R})d\mathbf{R}} \tag{2.22}$$

The entropy of an ideal chain can thus be expressed in terms of the probability distribution function as

$$\begin{aligned} S(N,\mathbf{R}) &= k_B \ln P(N,\mathbf{R}) + k_B \ln \left[\int \Omega(N,\mathbf{R}) d\mathbf{R} \right] \\ &= -\frac{3}{2} k_B \frac{\mathbf{R}^2}{Nb^2} + S(N,0) \end{aligned} \tag{2.23}$$

where $S(N,0)$ denotes the component that only depend on the number of Kuhn steps but not on the end-to-end vector $\mathbf{R}$. The free energy of the chain is $A(N,\mathbf{R}) = U(N,\mathbf{R}) - TS(N,\mathbf{R})$ where $U(N,\mathbf{R})$ is the internal energy of an ideal chain. Because the monomers of an ideal chain do not have any interaction energy, the internal energy $U(N,\mathbf{R})$ is independent of the equilibrium conformation of the polymer. As a result, the only $\mathbf{R}$ dependence of the free energy originates from the entropy of the chain (first term in Equation 2.23), and the free energy can be written as

$$A(N,\mathbf{R}) = \frac{3}{2} k_B T \frac{\mathbf{R}^2}{Nb^2} + A(N,0) \tag{2.24}$$

2.2.2 Excluded Volume Effects

The above section discussed the equilibrium conformation of an ideal polymer chain that has no long-range interactions between monomers and can pass through itself. In fact, this situation is never realized for real chains as they always interact with both the solvent and themselves. The relative strength of these interactions determines whether the monomers effectively attract or repel one another, and thus affects the size of the equilibrium coil. The balance between the monomer-monomer interaction and monomer-solvent interaction is theoretically described with an excluded volume parameter v. In a theta solvent where monomers do not have a preference of being near or away from each other, this excluded volume parameter is zero ($v = 0$) and the chain adopts a nearly ideal conformation (the chain is still not entirely ideal as its segments cannot pass through one another). In a poor solvent where the net interaction is attractive, polymer chains have a negative excluded volume parameter ($v < 0$) and tend to clump into a tightly packed globule. Finally, in a good solvent, the excluded volume parameter is positive ($v < 0$) and the equilibrium coil swells due to net repulsions between monomers.

Most aqueous buffers (e.g., the ones used in this thesis) have been found to be very good solvents for double-stranded DNA [71]. At this limit the major contribution to the excluded volume parameter comes from the hard-core repulsions between chain segments, and it can be shown that $v \approx wb^2$ for each Kuhn segment in a freely jointed chain where w is the diameter of the segment and b is the Kuhn length. Following this thought, a scaling of the end-to-end distance R of the chain can be obtained with the Flory theory [68]. First, we assume that monomers are uniformly distributed within the volume R^3. The probability that a monomer overlaps the excluded volume of a second monomer is then expected to be vN/R^3, and each overlap gives rise to an energy increase of k_BT. Therefore, for all N monomers in the chain, the total energy due to excluded volume interactions is given by

$$A_{\mathrm{EV}} \sim k_B T v \frac{N^2}{R^3} \tag{2.25}$$

The energy gain due to the loss in entropy with increasing coil size is given by Equation 2.24, and the total free energy of a real chain in the Flory approximation is

$$A \sim k_B T \frac{R^2}{Nb^2} + k_B T v \frac{N^2}{R^3} \tag{2.26}$$

Note that for the total free energy we only kept the terms that are R dependent. Also, for the scaling analysis we have neglected all the numerical prefactors. Taking the minimum of the total free energy with end-to-end distance gives the optimum size of the real chain:

$$R \sim v^{1/5} b^{2/5} N^{3/5} \tag{2.27}$$

Comparing Equation 2.27 to Equation 2.3, the size of a long real chain in a very good solvent scales as $N^{3/5}$ and is indeed larger than that of an ideal chain (scale as $N^{1/2}$) with the same contour length. We should note that the above analysis is only valid when the total interaction energy A_{EV} of the chain at its ideal conformation ($R_0 = bN^{1/2}$) is greater than $k_B T$ and we define a chain interaction parameter as

$$z = \frac{A_{\mathrm{EV}}(R_0)}{k_B T} \sim \frac{v}{b^3} N^{1/2} \tag{2.28}$$

Excluded volume interactions only swell the chain when z is greater than unity, otherwise the chain's conformation remains nearly ideal. We also note that result of Equation 2.27 is obtained through the cancelation of two errors made in the derivation by using results from the ideal chain models. The repulsive interaction energy is overestimated as the number of monomer to monomer contacts in a chain that can pass through itself is significantly larger than that in a real chain. Secondly, the elastic energy is overestimated as well because it too was calculated using the ideal chain conformation. Nevertheless, the predictions of Flory theory are in good agreement with both experiments and with more sophisticated theories (e.g., renormalization group calculations give $R \sim N^{0.588}$) [69].

In general, the inclusion of long-range interactions changes the scaling of the equilibrium polymer size with molecular weight as

$$R \sim N^{\nu_d} \tag{2.29}$$

where ν_d is the Flory-Edwards scaling exponent. By analogy with a self avoiding random walk (SAW), it has been shown that $\nu_d \approx 3/(d+2)$ where $d \leq 4$ is the dimensionality of the system [72]. For a 3D system, we recover the exponent predicted by Flory theory $\nu_{3d} = 3/5$. In a 2D system which is more relevant to polymer confinement, the exponent is $\nu_{2d} = 3/4$.

2.2.3 Entropic Elasticity

When a polymer is deformed away from equilibrium, its conformational freedom becomes restricted, giving rise to an entropic spring force that opposes the deformation. From simple thermodynamics arguments, this force is given by

$$\mathbf{F}_{\mathrm{S}} = -\frac{\partial A}{\partial \mathbf{R}} \tag{2.30}$$

where A is the free energy of the chain. If a polymer chain is only slightly perturbed from its equilibrium conformation, the entropic spring force can be derived using its equilibrium free energy.

For an ideal chain, we take the result of Equation 2.24 and arrive at

$$\mathbf{F}_S = -\frac{\partial}{\partial \mathbf{R}}\left(\frac{3k_BT\mathbf{R}^2}{2Nb^2}\right) = -\frac{3k_BT}{Nb^2}\mathbf{R} \tag{2.31}$$

Equation 2.31 indicates that the spring force near equilibrium, for any polymer that can be accurately modeled with Kuhn segments, is Hookean with a spring constant

$$H_{\text{bulk}} = \frac{3k_BT}{Nb^2} \tag{2.32}$$

This linear force regime is strictly valid only very near equilibrium. Recent experiments with double-stranded DNA molecules [73] have found that the linear regime extends to about 30% relative extension.

As the polymer stretches beyond the linear force regime, the finite extensibility of the chain comes into play, that is, the extension must saturate at the full contour length, and the spring force becomes nonlinear: it diverges as the chain approaches full extension. The nonlinear spring force can still be calculated with Equation 2.30. However, the polymer no longer follows the Gaussian random walk statistics at large extensions and its free energy now relies on the nature of the local, small length scale detail of the chain. The free energy of a freely jointed chain can be evaluated by computing the probability distribution function of the end-to-end distance under a constant given force. Such an analysis has been performed by Flory [74], and the resulting average end-to-end distance given a constant force is

$$\frac{\langle R\rangle}{L_c} = \coth\left(\frac{F_S b}{k_BT}\right) - \frac{k_BT}{F_S b} \tag{2.33}$$

The high-extension spring force of a worm-like chain behaves quantitatively different from that of a freely jointed chain due to the large bending potential. The bending energy of a worm-like chain is related to the persistence length p as

$$U_{\text{bend}} = k_BT\frac{p}{2}\int_0^{L_c}\left|\frac{\partial^2\mathbf{R}}{\partial s^2}\right|^2 ds \tag{2.34}$$

The total effective free energy of a worm-like chain under a constant force F_S is given by [75]

$$A = U_{\text{bend}} - F_S R \tag{2.35}$$

The average end-to-end distance of a worm-like chain at a given force may be calculated assuming the probability of the end-to-end distance scales as $P(R) \sim \exp(-A(R)/k_BT)$. The exact calculation has been done numerically by Marko and Siggia [76]. Although no closed form analytical solution exists to describe to the worm-like chain spring force law, a useful interpolation formula that captures the correct behavior at large and small extensions was suggested by Marko and Siggia:

$$\frac{F_S p}{k_BT} = \frac{1}{4}\left(1 - \frac{R}{L_c}\right)^{-2} - \frac{1}{4} + \frac{R}{L_c} \tag{2.36}$$

Equation 2.36 has been experimentally shown to match the entropic spring force law of double-stranded DNA [77].

2.2.4 Dynamic Behavior of Polymers

The previously introduced polymer models all focused on the static properties of a polymer's conformation. In this section we discuss the dynamic behavior of a polymer in solution, which will also be important in our study of DNA deformation in non-uniform electric fields.

Bead-Spring Model

The dynamics of an unconfined polymer are governed by the net effect of any externally applied forces, the Brownian motion of chain segments, tensions generated within the chain due to entropic elasticity, and intrachain hydrodynamic interactions (HI). To model the large length scale motion (relative to the size of the coil) of a polymer, it is convenient to represent the chain with a series of N beads connected by $N-1$ springs. Each spring models a portion of the full chain and has a contour length $L_s = L_c/(N-1)$. The beads are centers of interaction with the solvent (i.e., all drag between the polymer and solvent occurs at the beads) and the springs are used to describe the tension that arises when a subsection of the polymer is stretched. Since inertial at these microscopic scales is small, the motion of the ith bead can be simply described by the force balance

$$\mathbf{F}_i^{\text{external}} + \mathbf{F}_i^{\text{D}} + \mathbf{F}_{i-1,i}^{\text{S}} + \mathbf{F}_{i,i+1}^{\text{S}} + \mathbf{F}_i^{\text{B}} + \mathbf{F}_i^{\text{HI}} = \mathbf{0} \tag{2.37}$$

where $\mathbf{F}_i^{\text{external}}$ is the force externally applied to the bead, $\mathbf{F}_i^{\text{D}}$ is the drag force exerted by the solvent due to motion of the bead, $\mathbf{F}_{i-1,i}^{\text{S}}$ and $\mathbf{F}_{i,i+1}^{\text{S}}$ are the tensile forces of the spring connecting the $i-1^{\text{th}}$ and i^{th} bead, and that connecting the ith and $i+1^{\text{th}}$ bead, respectively, $\mathbf{F}_i^{\text{B}}$ is the Brownian force, and $\mathbf{F}_i^{\text{HI}}$ is the force due to HI.

For now we neglect external forces to observe the dynamics of polymers at rest. The drag force on a bead is given by Stokes' law:

$$\mathbf{F}_i^{\text{D}} = -\zeta_b \frac{\partial \mathbf{x}_i}{\partial t} \tag{2.38}$$

where ζ_b is the hydrodynamic drag coefficient of the bead. The tensile force between neighboring beads can be assumed to remain Hookean at small deformations

$$\mathbf{F}_{i-1,i}^{\text{S}} = H_s(\mathbf{x}_{i-1} - \mathbf{x}_i) \tag{2.39}$$

$$\mathbf{F}_{i,i+1}^{\text{S}} = H_s(\mathbf{x}_{i+1} - \mathbf{x}_i) \tag{2.40}$$

where $H_s = 3k_BT/bL_s$ is the spring constant for each spring. The Brownian force follows a Gaussian profile characterized by the moments

$$\langle \mathbf{F}_i^{\text{B}}(t) \rangle = 0 \tag{2.41}$$

$$\langle \mathbf{F}_i^{\text{B}}(t)\mathbf{F}_j^{\text{B}}(t') \rangle = 2\zeta_b k_B T \delta_{ij} \delta(t-t') \mathbf{I} \tag{2.42}$$

where $\delta(t-t')$ is the Dirac delta function, δ_{ij} is the Kronecker delta and $\mathbf{I}$ is the identity tensor. Equation 2.37 can now be rewritten as

$$\frac{\partial \mathbf{x}_i}{\partial t} = \frac{1}{\zeta_b}\left[H_s(\mathbf{x}_{i-1} - 2\mathbf{x}_i + \mathbf{x}_{i+1}) + \mathbf{F}_i^{\text{B}} + \mathbf{F}_i^{\text{HI}}\right] \tag{2.43}$$

HI is the interaction between chain segments due to the motion of one segment creating a flow field which propagates to the position of another segment. The flow disturbance from bead j on bead i can be mediated using a mobility tensor $\mathbf{H}_{ij}$ which converts Equation 2.43 into

$$\frac{\partial \mathbf{x}_i}{\partial t} = \sum_j \mathbf{H}_{ij} \cdot \left[H_s(\mathbf{x}_{j-1} - 2\mathbf{x}_j + \mathbf{x}_{j+1}) + \mathbf{F}_j^{\mathrm{B}}\right] \tag{2.44}$$

Equation 2.44, also called the Langevin equation, provides a starting point for our analysis of chain dynamics. We now introduce two models that represent the limiting case of no intrachain HI (Rouse model) and dominating HI (Zimm model), respectively.

Rouse Model

The Rouse model assumes no excluded volume interaction and intrachain hydrodynamic interaction. The mobility tensor is given by

$$\mathbf{H}_{ij} = \frac{\mathbf{I}}{\zeta_b}\delta_{ij} \tag{2.45}$$

and Equation 2.44 reduces to a linear partial differential equation:

$$\zeta_b \frac{\partial \mathbf{x}_i}{\partial t} = H_s(\mathbf{x}_{i-1} - 2\mathbf{x}_i + \mathbf{x}_{i+1}) + \mathbf{F}_i^{\mathrm{B}} \tag{2.46}$$

For a Gaussian chain, the subscript i can be regarded as a continuous variable. In the continuous limit the spring constant $H_s = 3k_BT/b^2$ and Equation 2.46 can be written as

$$\zeta_b \frac{\partial \mathbf{x}_i}{\partial t} = \frac{3k_BT}{b^2}\frac{\partial^2 \mathbf{x}_i}{\partial i^2} + \mathbf{F}_i^{\mathrm{B}} \tag{2.47}$$

with the boundary conditions that there is no tension in the chain at the chain endpoints:

$$\left.\frac{\partial \mathbf{x}_i}{\partial i}\right|_{i=1,N} = \mathbf{0} \tag{2.48}$$

The resulting linear, stochastic partial differential equations can be solved through the use of normal coordinates that can decouple the modes of motion of the chain. In terms of the coordinates $\mathbf{X}_q$ defined by

$$\mathbf{X}_q = \frac{1}{N}\int_0^N \cos\left(\frac{q\pi i}{N}\right)\mathbf{x}_i(t)di \quad \text{with} \quad q = 0,\ 1,\ 2,\ ... \tag{2.49}$$

Equation 2.47 can be transformed to

$$\zeta_n \frac{\partial \mathbf{X}_n}{\partial t} = -H_q\mathbf{X}_q + \mathbf{F}_q^{\mathrm{B}} \tag{2.50}$$

where

$$\zeta_0 = N\zeta_b \quad \text{and} \quad \zeta_q = 2N\zeta_b \quad \text{for} \quad q = 1,\ 2,\ ... \tag{2.51}$$

$$H_q = \frac{6\pi^2 k_BT}{Nb^2}q^2 \quad \text{for} \quad q = 0,\ 1,\ 2,\ ... \tag{2.52}$$

Since the random forces $\mathbf{F}_q^{\mathrm{B}}$ are independent of each other, the motion of each $\mathbf{X}_q$ is also independent of all other $\mathbf{X}_q$. As a result, the dynamical motion of the polymer is decomposed into independent modes. Generally speaking, $\mathbf{X}_0$ is the center of mass of the polymer and $\mathbf{X}_q$ (for $q > 0$) represents the local motion of the chain which includes N/q segments [69]. The dynamic properties of the polymer can be extracted from the time correlation functions of these normal coordinates. Specifically, it can be shown that the mean square displacement of the center of mass is given by

$$\langle (x_{\mathrm{com}}(t) - x_{\mathrm{com}}(0))^2 \rangle = 6\frac{k_B T}{N\zeta_b} t \tag{2.53}$$

The diffusivity of the polymer is therefore

$$D = \frac{k_B T}{N\zeta_b} \tag{2.54}$$

and the drag coefficient of a rouse chain is $\zeta = N\zeta_b$. Similarly, the time correlation function of the end-to-end vector $\mathbf{R}$ can be calculated

$$\langle \mathbf{R}(t) \cdot \mathbf{R}(0) \rangle = Nb^2 \sum_{q,\,\mathrm{odd}} \frac{8}{q^2\pi^2} \exp\left(-\frac{tq^2}{\tau_1}\right) \tag{2.55}$$

where

$$\tau_1 = \frac{\zeta_b N^2 b^2}{3\pi^2 k_B T} \tag{2.56}$$

is called the longest rotational relaxation time of the polymer. We see that this time correlation function is described by a series of modes each of which decays exponentially with a characteristic time scale $\tau_q = \tau_1/q^2$. Thus, the long-time ($t > \tau_1$) rotational motion of the end-to-end vector is primarily governed by the first mode ($\mathbf{X}_1$) and contributions from higher-order modes are minor. It is worthwhile to note that the longest rotational relaxation time is proportional to the ratio of the drag coefficient and spring constant of the entire chain (i.e., the first normal mode):

$$\tau_1 \sim \zeta / H_{\mathrm{bulk}} \tag{2.57}$$

We also distinguish τ_1 from the longest stress relaxation time τ_{s}, which is the characteristic time for the stress relaxation of a stretched polymer in the linear spring force regime. These two characteristic time scales are related by a factor of 2 [68]: $\tau_1 = 2\tau_{\mathrm{s}}$.

Zimm Model

The Rouse model predicts the molecular weight dependence of D and τ_1 to be $D \sim N^{-1}$ and $\tau_1 \sim N^2$, which does not reproduce experimental results with dilute polymer solutions. The main deficiency comes from the neglect of HI. In fact, the flow field in the solvent induced by the motion of one chain segment can significantly affect the motion of nearby segments. Such effects can be add to the polymer dynamics model by modifying the mobility tensor to account for the solvent disturbance due to a point force, giving a form for $\mathbf{H}_{ij}$ (the Oseen tensor):

$$\mathbf{H}_{ii} = \frac{\mathbf{I}}{\zeta_b}, \quad \mathbf{H}_{ij} = \frac{1}{8\pi\eta|\mathbf{r}_{ij}|}\left(\frac{\mathbf{r}_{ij}\mathbf{r}_{ij}}{|\mathbf{r}_{ij}|^2} + \mathbf{I}\right) \tag{2.58}$$

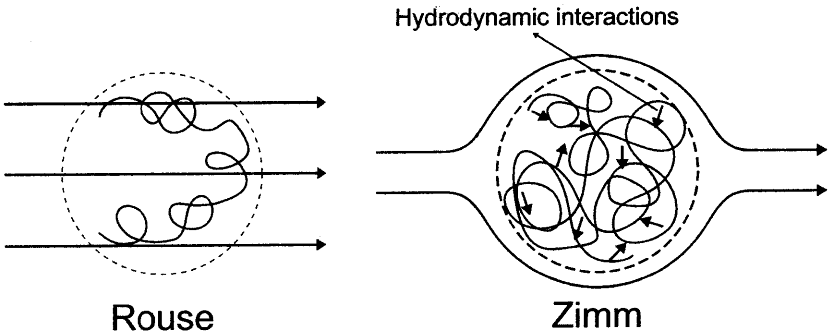

Fig. 2.2: *Schematics of a Rouse polymer (no hydrodynamic interactions) and a Zimm polymer with hydrodynamic interactions. The dashed circle implies that the Zimm polymer entrains solvent and its drag scales like a solid sphere with radius* $R \sim N^{\nu} b$.

where $\mathbf{r}_{ij} = \mathbf{x}_i - \mathbf{x}_j$ is the vector from bead j to bead i and η is the solvent viscosity. However, the Langevin equation 2.44 now becomes highly nonlinear and is difficult to handle. To simplify the analysis, Zimm [78] used a pre-averaging approximation, which approximates $\mathbf{H}_{ij}$ by its equilibrium average as:

$$\mathbf{H}_{ij} \to \langle \mathbf{H}_{ij} \rangle_{\mathrm{eq}} = \frac{\mathbf{I}}{6\pi\eta} \left\langle \frac{1}{|\mathbf{r}_{ij}|} \right\rangle_{\mathrm{eq}} \tag{2.59}$$

where the equilibrium distribution of r_{ij} is usually known. Using the pre-averaging approximation, Equation 2.44 can be linearized and it is again In a theta solvent, the distribution of r_{ij} is Gaussian with variance $|i-j|b^2$ and hence

$$\langle \mathbf{H}_{ij} \rangle_{\mathrm{eq}} = \frac{\mathbf{I}}{(6\pi^3|i-j|)\eta b} \tag{2.60}$$

With the pre-averaging approximation, Equation 2.44 becomes linear and it is again possible to obtain normal mode correlation functions as outlined for the Rouse model. If the mobility tensor is pre-averaged with the equilibrium conformation of an ideal chain, the resulting diffusivity and longest rotational relaxation time are given by

$$D = 0.196 \frac{k_B T}{\eta N^{1/2} b} \quad \text{and} \quad \tau_1 = 0.325 \frac{\eta N^{3/2} b^3}{k_B T} \tag{2.61}$$

For polymers in a good solvent, the Zimm dynamic properties can also be computed by including excluded volume in the pre-averaging step. The results, however, are very similar to Equation 2.61 with the inclusion of the Flory-Edwards exponent [69]:

$$D \sim \frac{k_B T}{\eta N^{\nu} b} \quad \text{and} \quad \tau_1 \sim \frac{\eta N^{3\nu} b^3}{k_B T} \tag{2.62}$$

The results of Equation 2.61 and 2.62 are both quantitatively different from those of the Rouse model. Specifically, we notice that the presence of HI mediates the the effective drag length of a polymer. In a Rouse chain, the drag coefficient scales proportionally to its contour length ($\zeta \sim \eta L_c \sim \eta N$), indicating the chain is "free-draining" (i.e., the flow can penetrate into the coil and acts individually on each segment). In contrast, the drag coefficient of a Zimm chain scales proportionally to the equilibrium coil size ($\zeta \sim \eta R \sim \eta N^{\nu}$), suggesting the chain moves more like a solid sphere of size R (see Figure 2.2). As a result, the presence of HI reduces the tendency of the flow to penetrate into the coil: chain segments near the outer surface of the coil tend to "shield" the inner segments from the flow. In the limit of dominant HI within the coil, the polymer effectively drags with it the the solvent within its pervaded volume when it moves.

2.3 Electrokinetic Theories

In this section we introduce theories describing the transport of ions in electrolyte solutions and two electrokinetic phenomena: electroosmosis and electrophoresis under an applied electric field.

2.3.1 Charge Transport in Electrolyte Solution

The electric current in an electrolyte solution is carried by the dissolved ions rather than by free electrons. The ion fluxes are described by the Nernst-Planck equation [79]

$$\mathbf{N}_i = \frac{|z_i|}{z_i} u_i C_i \mathbf{E} - D_i \nabla C_i + C_i \mathbf{v} \tag{2.63}$$

where the subscript i denotes ion species, z_i, u_i, C_i, and D_i are the valence, mobility, concentration, and diffusivity of ion species i, $\mathbf{E}$ is the electric field, and $\mathbf{v}$ is the solvent velocity. The ion mobility and diffusivity are related via $D_i/u_i = RT/|z_i|F$ where F is the Faraday constant. The total current density due to the ion fluxes is then given by

$$\begin{aligned} \mathbf{J} &= \sum_i z_i F \mathbf{N}_i = \frac{F^2}{RT}\mathbf{E}\sum_i z_i^2 D_i C_i - \sum_i z_i F D_i \nabla C_i + \sum_i z_i F C_i \mathbf{v} \\ &= \sigma \mathbf{E} - \sum_i z_i F D_i \nabla C_i + \rho_e \mathbf{v} \end{aligned} \tag{2.64}$$

where σ is the electrical conductivity of the electrolyte solution defined as $\sigma = \frac{F^2}{RT}\sum_i z_i^2 D_i C_i$, and ρ_e is the net space charge density $\rho_e = \sum_i z_i F C_i$. The change of ρ_e is governed by the law of conservation of charge

$$-\frac{\partial \rho_e}{\partial t} = \nabla \cdot \mathbf{J} \tag{2.65}$$

The electric field $\mathbf{E}$ in Equation 2.65 depends on the concentrations of the ions according to Gauss' law

$$\epsilon \nabla \cdot \mathbf{E} = \rho_e \tag{2.66}$$

where ϵ is the dielectric permittivity of the solution and is assumed to be a constant in our analysis. We see that Equation 2.65 and 2.66 are coupled through the interdependence of the ion concentration and the electric field. The most common approach to decouple these two equations is to assume that the electrolyte solution is locally electroneutral ($\rho_e = 0$) and the electric field can then be specified independently ($\nabla \cdot \mathbf{E} = 0$) with given boundary conditions. In fact, electroneutrality is an excellent approximation for most situations, failing only in the vicinity of charged interface as we will discuss below. The validity of this assumption can be verified by examining the decay of any free charge in the bulk (i.e., far away from any interfaces) of a homogeneous, static electrolyte solution. Under these conditions the current density is simply given by $\mathbf{J} = \sigma\mathbf{E}$ and Equation 2.65 can be rewritten as

$$\frac{\partial \rho_e}{\partial t} + \nabla \cdot \sigma\mathbf{E} = \frac{\partial \rho_e}{\partial t} + \frac{\sigma}{\epsilon}\rho_e = 0 \tag{2.67}$$

The solution to the above equation is $\rho_e(t) = \rho_e(0)\exp(-t/\tau_{\mathrm{RC}})$ where $\tau_{\mathrm{RC}} = \epsilon/\sigma$, suggesting that unless there is a steady source of bulk free charge, ρ_e will decay to zero exponentially. The characteristic time for the exponential decay, τ_{RC}, is called the charge relaxation time which is usually extremely small (e.g., $\tau_{\mathrm{RC}} \approx 10^{-9}\,\mathrm{s}$ in a 0.1 M NaCl solution). As a result, any free charge in the bulk solution would vanish almost instantaneously and the system always stays electroneutral at time scales larger than τ_{RC}.

In an electroquasistatic system where either the local magnetic field or the time rate of change of the magnetic field is negligibly small, the electric field does not have any rotational component $\nabla \times \mathbf{E} = 0$, and thus can be expressed in terms of the gradient of an electric potential Φ: $\mathbf{E} = -\nabla\Phi$. Equation 2.66 can be rewritten in terms of Φ which leads to Poisson's equation

$$-\epsilon\nabla^2\Phi = \rho_e \tag{2.68}$$

2.3.2 Charged Surface and Electric Double Layer

When a charged surface is immersed in an electrolyte solution, the distribution of nearby ions in the solution will be affected. Counterions are attracted toward the surface while conions are repelled from the surface. This attraction and repulsion leads to the formation of an electric double layer, within which there are both an induced ion concentration gradient and induced electrostatic potential. Electroneutrality is broken in the double layer as an excess of counterions over coions is required to neautralize the surface charge. The electric double layer (see Figure 2.3) is composed of an inner Stern layer where counterions are permanently adsorbed to the charged surface and an outer diffuse layer where all the ions remain mobile [80]. Determination of the ion concentration and electric potential profiles in the double layer is important to developing models of how charged objects move in an externally applied electric field.

If we assume the distribution of all ions in the diffuse layer can be adequately described by Boltzmann distribution (at equilibrium) $C_i = C_{i,\infty}\exp(-z_iF\Phi/RT)$, the Poisson's equation can be rewritten as

$$-\epsilon\nabla^2\Phi = F\sum_i z_iC_{i,\infty}\exp\left(-\frac{z_iF\Phi}{RT}\right) \tag{2.69}$$

where $C_{i,\infty}$ is the bulk concentration of ion species i. Equation 2.69 can be further linearized using the Debye-Hückel approximation [81] of small potentials $z_iF\Phi/RT \ll 1$, giving

$$\nabla^2\Phi = \kappa^2\Phi \quad \text{where } \kappa^{-1} = \sqrt{\frac{\epsilon RT}{F^2\sum_i z_i^2C_{i,\infty}}} \tag{2.70}$$

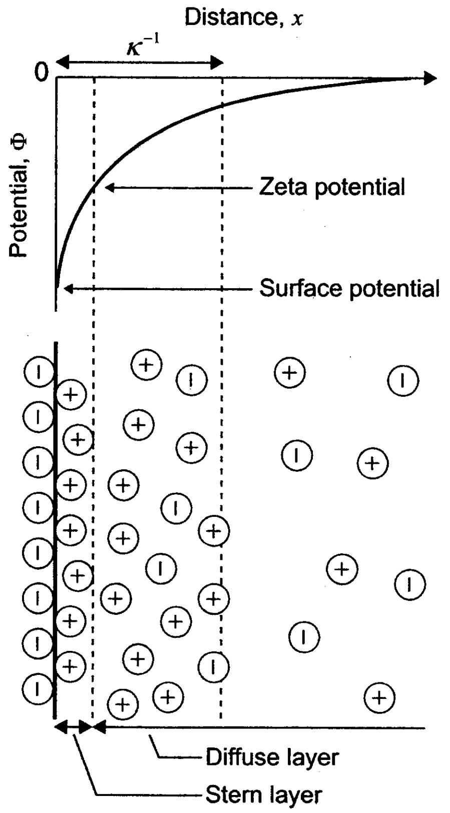

Fig. 2.3: *Schematics of the structure of the double layer near a negatively charged surface, and the corresponding profile of the electric potential.*

For a flat charged surface (or small local surface curvature), the solution to Equation 2.70 is $\Phi(x) = \Phi(0)\exp(-\kappa x)$ where x is a coordinate that determines distance into solution from the surface (see Figure 2.3). The length scale κ^{-1} is called the Debye length and is the characteristic length scale for the decay of the electric potential induced by charged object. Consequently, at distances much larger than the Debye length, electrostatic interactions between charged objects are effectively screened. We note that the Debye length is only a solution property and has a strong dependence on the ionic strength of the solution $I = \frac{1}{2}\sum_i z_i^2 C_i$. In the salt concentrations used in this thesis $I \approx 0.01$ to $0.1\,\mathrm{M}$, $\kappa^{-1} \approx 1$ to $3\,\mathrm{nm}$. Since charge screening occurs over distances much smaller than the persistence length of dsDNA ($p \approx 50\,\mathrm{nm}$), the electrostatic potentials will not result in significant stiffening of the molecule. However, the diameter of the dsDNA is $2\,\mathrm{nm}$ (comparable to κ^{-1}), and it has very recently been shown [58] that these electrostatic potentials can slightly affect physics where the diameter of the DNA is important (e.g., the excluded volume parameter v, see section 2.2.2). Finally, for strongly charged objects (e.g., dsDNA in common electrophoresis buffer), the Debye-Hückel approximation is not strictly valid as $zF\Phi/RT \sim 1$, and Equation 2.69 needs to be solved more generally with Gouy-Chapman theory [81]. Nevertheless, the Debye-Hückel solution closely captures the most important physics of the screening length scale κ^{-1}.

2.3.3 Electroosmosis

We have just shown the existence of a local region with a net charge density (excess counterions) near a charged surface. When an electric field is applied along the surface, the electric body forces acting on the charged fluid will initiate an electroosmotic flow (EOF). The velocity profile of EOF near a flat, stationary surface is given by

$$\mathbf{v}(x) = -\frac{\epsilon\Phi_\zeta\mathbf{E}}{\eta}[1 - \exp(\kappa x)] \tag{2.71}$$

where $\mathbf{E}$ is the electric field applied parallel to the surface, Φ_ζ is the zeta potential defined as the electric potential at the surface separating the stern layer and the diffuse layer (see Figure 2.3). At distances much larger than the Debye length κ^{-1}, the EOF profile is plug-like (see Figure 2.4) with a uniform velocity $\mathbf{v} = -\epsilon\Phi_\zeta\mathbf{E}/\eta$.

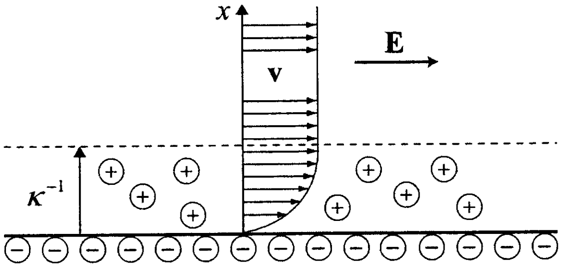

Fig. 2.4: *Schematic of the electroosmosis velocity profile near a flat, negatively charged surface.*

Since the surfaces used in the micro- and nano-fluidic devices in this thesis (i.e., glass and PDMS) carry a negative charge in aqueous solution, the resulting EOF will oppose the electrophoresis of negatively charged DNA. Consequently, EOF must be sufficiently quenched in these devices in order to conduct proper electrophoresis experiments. This is especially important in the microchannels which are hybrid PDMS/glass channels (bottom surface of the channel is glass and all other surfaces are PDMS) as the EOF will have a shear profile due to the different zeta potentials of the PDMS and glass surfaces [82] and thus can lead to unstable motion of DNA. Because the magnitude of the electroosmosis velocity at a given electric field strength depends on both the ionic strength (higher ionic strength results in lower zeta potential) and viscosity of the solution, EOF can be suppressed by operating at high ionic strengths or by selectively increasing the solution viscosity near the channel walls. The method used throughout this thesis is to dynamically adsorb surface-active polymers to the channel walls, drastically increasing the local viscosity and therefore decreasing the velocity of EOF.

2.3.4 Electrophoresis

The term "electrophoresis" refers to the migration of a charged object induced by an applied electric field. Physically, this motion is closely related to the charged surface physics and is fundamentally different from purely hydrodynamic motion caused by non-electric forces. An electric field exerts simultaneous forces both on the charged object and on the surrounding fluid via the excess counterions in the double layer (retardation effect, see Figure 2.5), whereas in a purely hydrodynamic motion the applied force acts only on the object. Consequently, in order to properly describe electrophoresis, the extra hydrodynamic drag force due to surface electroosmotic flows must be taken into account in addition to the electric body force on the charged object and the hydrodynamic drag force due to motion of the object.

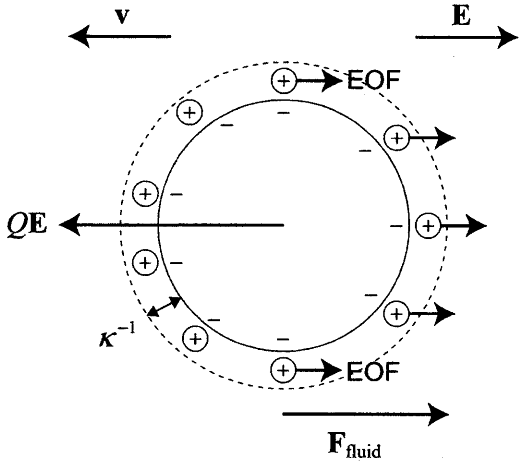

Fig. 2.5: *Schematic of a negatively charged spherical particle during electrophoresis.*

Mathematically, electrophoresis is a complicated problem because the local electric potential, ionic concentrations, and fluid flow are all coupled to one another. Henry [83] first calculated the electrophoretic velocity $\mathbf{v}_\infty$ of a spherical, insulating particle with radius R and uniformly distributed charge Q. The analysis begins in the particle frame of reference, in which the particle is stationary and the fluid has a uniform velocity $-\mathbf{v}_\infty$ at infinity. The critical assumption made by Henry to simplify the analysis is that the double layer of the particle is undistorted by the applied electric field and hence the electric potential (ψ) arising from the particle charge can be superimposed onto the electric potential (ϕ) due to the externally applied electric field. As a result, the two electric potentials can be solved independently with the equations $\nabla^2\phi = 0$ and $\nabla^2\psi = -\rho_e/\epsilon$, respectively, where ρ_e is the equilibrium charge distribution within the double layer of the particle. In the case of small surface potentials, ψ can be evaluated using the Debye-Hückel approximation for the spherical geometry, giving $\psi = \phi_\zeta \frac{R}{r}\exp[-\kappa(r-R)]$ where r ($r > R$) is the radial coordinate that determines distance into solution from the center of the particle. With the electric potential and the ion concentration profiles known, the pressure and fluid velocity distribution around the particle can be determined by solving the Navier-Stokes equation together with the continuity equation

$$\eta\nabla^2\mathbf{v} + \nabla p + \rho_e\nabla(\phi + \psi) = 0 \tag{2.72}$$

$$\nabla\cdot\mathbf{v} = 0 \tag{2.73}$$

(2.74)

where $\mathbf{v}$ is the fluid velocity and p is the hydrostatic pressure. We note that inertial terms in Equation 2.72 have been neglected given the small particle size. The electrophoretic velocity of the particle is calculated from the force balance on the sphere $\mathbf{F}_{\text{fluid}} + Q\mathbf{E} = 0$ where $\mathbf{F}_{\text{fluid}}$ is the total drag force exerted onto the particle by the fluid due to both motion of the particle and surface EOF, and $Q\mathbf{E}$ is the electric body force directly acting on the particle. The total drag force can be found from integrating all the viscous and pressure forces around the particle

$$\mathbf{F}_{\text{fluid}} = -6\pi\eta R\mathbf{v}_\infty + 4\pi R\epsilon\phi_\zeta \mathbf{E} f(\alpha) - Q\mathbf{E} \tag{2.75}$$

where $f(\alpha)$ is the Henry's function for a sphere [80] with $\alpha = \kappa R$. Interestingly, we see that the electric body force cancels out the last term in Equation 2.75 and the resulting electrophoretic velocity is given by

$$\mathbf{v}_\infty = \frac{2}{3}\frac{\epsilon\phi_\zeta \mathbf{E}}{\eta} f(\alpha) \tag{2.76}$$

In the limit of small Debye length comparing to the particle radius ($\alpha \gg 1$), $f(\alpha) = 3/2$, the electrophoretic velocity of the particle becomes independent of its size and is given by the Smoluchowski equation

$$\mathbf{v}_\infty = \frac{\epsilon\phi_\zeta}{\eta}\mathbf{E} \tag{2.77}$$

The electrophoretic mobility of the spherical particle is then $\mu = \epsilon\phi_\zeta/\eta$.

DNA is a polyelectrolyte with negative charges evenly distributed along its backbone. Since the conformation of a long (kbp–Mbp) DNA molecule must be described using multiple length scales (e.g., the radius of gyration R_g, the persistence length p, and the diameter of the chain), the above analysis for a single particle with well defined shape is not suitable to model the electrophoresis of DNA. A more reasonable description of DNA electrophoresis is given by long et al. [84] using a bead-spring model as described in section 2.2.4, but now with all the beads carrying a constant negative charge q. Considering effects from flows, electric fields, Brownian motions, intrachain tensions, and hydrodynamic interactions, the Langevin equation for bead i under a uniform external electric field $\mathbf{E}$ is given by:

$$\frac{\partial \mathbf{x}_i}{\partial t} = \sum_j \mathbf{H}_{ij} \cdot (\mathbf{F}^{\mathrm{S}}_{j-1,j} + \mathbf{F}^{\mathrm{S}}_{j,j+1} + \mathbf{F}^{\mathrm{B}}_j) + \mu_b \mathbf{E} + \sum_{j \neq i} \mathbf{H}^{\mathrm{EL}}_{ij} \cdot q\mathbf{E} \tag{2.78}$$

where μ_b is the electrophoretic mobility of a bead and $\mathbf{H}^{\mathrm{EL}}_{ij}$ is the mobility tensor that mediates the flow disturbances to bead i due to electrophoresis of bead j, very much like the Oseen tensor $\mathbf{H}_{ij}$ defined in Equation 2.58. Long et al. [84,85] suggested that this mobility tensor $\mathbf{H}^{\mathrm{EL}}_{ij}$ decays approximately as r_{ij}^{-3}, much faster than the Oseen tensor $\mathbf{H}_{ij}$ which decays as r_{ij}^{-1}. The physical reason for the drastically faster decay of the perturbed flow velocity in electrophoresis is that the the long range fluid disturbance induced by the electrophoretic motion is exactly canceled by the long range fluid disturbance due to the surface EOF [85,86]. Consequently, the hydrodynamic interactions due to electrophoretic motion of the beads can be neglected at large length scales, and Equation 2.78 can be simplified into

$$\frac{\partial \mathbf{x}_i}{\partial t} = \sum_j \mathbf{H}_{ij} \cdot (\mathbf{F}^{\mathrm{S}}_{j-1,j} + \mathbf{F}^{\mathrm{S}}_{j,j+1} + \mathbf{F}^{\mathrm{B}}_j) + \mu_b \mathbf{E} \tag{2.79}$$

The above equation can again be solved using normal modes as done for the Zimm model. In the case of thin Debye length (or high buffer ionic strength), it turns out that the electrophoretic mobility of the polyelectrolyte in free solution is size-independent and equal to the local mobility μ_b, and the chain moves without average deformation. Experimental studies have confirmed that the mobility of DNA is indeed constant at low electric fields and independent of molecular weight for large (>1 kbp) DNA in various buffers [87]. The remaining question is that whether the DNA mobility can be directly related to the Smoluchowski equation (Equation 2.77) which requires the size of the object to be significantly larger than κ^{-1}, as the diameter of the DNA ($\approx 2\,\mathrm{nm}$) is about the same as κ^{-1}. Stigter [88] argued that as long as the persistence length of the DNA is much larger than κ^{-1}, the Smoluchowski equation is still a good approximation for a persistence segment that movies parallel to the electric field. However, theoretical studies by Henry [83], Ohshima [89], and Stigter [88] all suggested that the electrophoretic mobility of a charged rod is anisotropic and varies with the orientation of the rod with respect to the applied field. van den Heuvel et al. [86] recently experimentally measured the mobility of individual microtubules and showed a relatively weak orientation dependence of the mobility: the mobility of a microtubule oriented parallel to the field ($\mu_{||}$) is about 20% larger than that of a microtubule oriented perpendicular to the field ($\mu_{\perp}$). So far no experimental work has been carried out to quantitatively characterize the importance of the mobility anisotropy to DNA electrophoresis. Nevertheless, we can take the DNA mobility μ as an experimentally measured constant so that the velocity of all sections of the DNA under a uniform external electric field is $\mu\mathbf{E}$. In the micro- or nano-channels used in this thesis, the measured mobility contains contributions from both DNA electrophoresis and electroosmotic flow in the channel. Consequently, this mobility will depend on the channel material (determines surface charge), the amount of EOF quenching, and the buffer ionic strength.

2.4 Stretching DNA

Due to the entropic elasticity, an external force must be applied to extend a single DNA molecule. Oftentimes this is achieved by placing the DNA chain in a non-uniform hydrodynamic flow or electric field. In a bead-spring chain model, the Langevin equation governing the motion of each bead under the simultaneous action of hydrodynamic and electric forces is given by

$$\frac{\partial \mathbf{x}_i}{\partial t} = \sum_j \mathbf{H}_{ij} \cdot \left(\mathbf{F}^{\mathrm{S}}_{j-1,j} + \mathbf{F}^{\mathrm{S}}_{j,j+1} + \mathbf{F}^{\mathrm{B}}_{j}\right) + \mathbf{u}_\infty(\mathbf{x}_i) + \mu_b \mathbf{E}(\mathbf{x}_i) \tag{2.80}$$

where $\mathbf{u}_\infty(\mathbf{x}_i)$ and $\mathbf{E}(\mathbf{x}_i)$ are the unperturbed flow velocity and electric field evaluated at the position of bead i, respectively. Again, the intrachain hydrodynamic interactions due to the electrophoretic motion of the beads are neglected. Note that the pure hydrodynamic deformation occurs when $\mathbf{E} = \mathbf{0}$ and both $\mathbf{u}_\infty$ and $\nabla\mathbf{u}_\infty$ are nonzero, and pure electrophoretic deformation occurs when $\mathbf{u}_\infty = \mathbf{0}$ and both $\mathbf{E}$ and $\nabla\mathbf{E}$ are nonzero. In Equation 2.80 we see the electrohydrodynamic equivalence proposed by Long et al. [38, 90], that is, the motion of a DNA chain under an electric field $\mathbf{E}$ is equivalent to that of the same DNA in a hydrodynamic flow with velocity $\mathbf{u} = \mu\mathbf{E}$. Implicit in this argument is that even though the HI due to electrophoretic motion is effectively screened by the surface EOF, the tensions generated within the chain and Brownian motions of chain segments will still give rise to HI (mediated by the Oseen tensor $\mathbf{H}_{ij}$) in electrophoretic deformation. This theory has been experimentally verified with tethered DNA [65, 91], however experiments for free

DNA do not exist at this time. Nevertheless, we invoke electrohydrodynamic equivalence to treat $\mu\mathbf{E}$ as a velocity field so that we can only consider DNA deformation in pure hydrodynamic flows for our analysis below.

The process of DNA extension in non-uniform fields is closely related to the detailed kinematics of the gradient of the flow (or electric field): $\nabla\mathbf{u}_\infty$ (or $\nabla\mu\mathbf{E}$). It is convenient to further decompose the velocity gradient tensor into a symmetric rate-of-strain tensor $\mathbf{\Gamma}$ and antisymmetric vorticity tensor $\mathbf{\Omega}$: $\nabla\mathbf{u}_\infty = \mathbf{\Gamma} + \mathbf{\Omega}$. The rate-of-strain tensor $\mathbf{\Gamma}$ solely governs the local deformation of fluid elements whereas the vorticity tensor $\mathbf{\Omega}$ controls the local rotation of fluid elements [79]. The rotational component in the velocity gradient tensor is generally not desired for stretching DNA as it results in unstable motions of DNA molecules (e.g., tumbling motion) [39]. Consequently, the most widely used non-uniform flow field to stretch single DNA is the extensional flow in which $\mathbf{\Omega} = \mathbf{0}$. In a 2D extensional flow, the local deformation can be characterized by the the positive eigenvalue of $\nabla\mathbf{u}_\infty$, termed the strain rate $\dot{\varepsilon}$, and the orthogonal eigenvectors $\mathbf{p}_+$ and $\mathbf{p}_-$ [40]. A fluid element will exponentially extend along the axis of extension $\mathbf{p}_+$ and exponentially compress along the axis of compression $\mathbf{p}_-$ at a rate governed by $\dot{\varepsilon}$. For a flexible object that can deform affinely with the fluid, the degree of extension is determined by the strain ε which is defined as the accumulated strain rate over the object's trajectory $x(t)$, $\epsilon = \int \dot{\epsilon}[x(t)]dt$. In a homogeneous extensional flow where the strain rate is constant, the strain is simply given by $\varepsilon = \dot{\varepsilon}t_{\text{res}}$ where t_{res} is the residence time of the molecule in the flow. An affinely deforming object with initial size object with initial size x_i will stretch to a length $x_i \exp(\varepsilon)$ after experiencing a strain of ε.

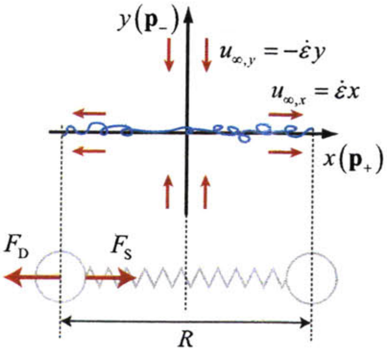
$y(\mathbf{p}_-)$
$u_{\infty,y} = -\dot{\varepsilon}y$
$u_{\infty,x} = \dot{\varepsilon}x$
$x(\mathbf{p}_+)$
F_D
F_S
R

Fig. 2.6: *Schematic of the dumbbell model used in the stretching analysis, the flow velocity profile is drawn in the dumbbell frame of reference.*

A real polymer chain usually does not deform affinely with the non-uniform flow field because the entropic elasticity will always arise to oppose stretching. In a 2D homogeneous extensional flow (constant $\dot{\varepsilon}$), the competition between the stretching force exerted by the velocity gradient and the polymer's elastic spring force trying to recoil the molecule can be characterized using a single dimensionless group termed the Deborah number De. The Deborah number is defined as the product of the strain rate $\dot{\varepsilon}$ and the polymer's longest stress relaxation time τ, $\mathrm{De} = \dot{\varepsilon}\tau$. It is essentially the ratio of two different time scales: the time scale of polymer relaxation back to equilibrium and the time scale of the flow deformation rate. The advantage of using De is that it is simple to determine and yet captures the two most important forces governing the stretching process. Experimental results [26, 27, 28, 29, 67] of the steady-state extensions of polymers with vastly different contour lengths have showed universal behavior with respect to De in a homogeneous extensional flow. Specifically, a sharp coil-stretch transition occurs near a critical value of Deborah number $\mathrm{De_c} = 0.5$. This unique behavior is related to the presence of a linear regime at small extensions in the spring force law [26] and can be demonstrated using a Rouse chain with only two beads and no Brownian motions (a non-Brownian dumbbell, see Figure 2.6). In the dumbbell frame of reference, the drag force exerted by the homogeneous extensional flow on each bead is written as $F_\mathrm{D} = (\frac{1}{2}\zeta)(\dot{\varepsilon}\frac{1}{2}R) = \frac{1}{4}\zeta\dot{\varepsilon}R$ where ζ is the drag coefficient of the entire chain and R is the end-to-end distance of the dumbbell. The spring force acting on each bead is given by $F_\mathrm{S} = H_\mathrm{bulk}R$ in the linear force regime and the spring constant H_bulk is given by Equation 2.32. Both the stretching force and spring force are linear with the dumbbell extension and their ratio is thus independent of R

$$\frac{F_\mathrm{D}}{F_\mathrm{S}} = \frac{\frac{1}{4}\zeta\dot{\varepsilon}R}{H_\mathrm{bulk}R} = \dot{\varepsilon}\frac{\zeta}{4H_\mathrm{bulk}} \tag{2.81}$$

We recall that the stress relaxation time of a Hookean dumbbell is given by $\tau = \zeta/8H_\mathrm{bulk}$ [92] and arrive at $F_\mathrm{D}/F_\mathrm{S} = 2\mathrm{De}$. It can now be seen that the critical Deborah number $\mathrm{De_c} = 0.5$ represents the condition when the stretching force exactly balances the entire linear portion of the spring force. At $\mathrm{De} < 0.5$, the stretching force is not strong enough to overcome the entropic elasticity and the dumbbell remains unextended. As soon as De exceeds 0.5, the stretching force becomes larger than the linear spring force and the molecule will stretch into a significantly extended state until the nonlinear elasticity limits any further extension. Similar analyses with the inclusion of HI have been performed by Larson and Magda [93, 94]. However, the resulting value of the critical Deborah number remains very similar to that in the case of a Rouse chain: $\mathrm{De_c} \approx 0.54$.

Finally we address one practical concern of using non-uniform flow or electric field to stretch single DNA molecules, that is, the strong dependence of the stretching rate on the initial configuration of the equilibrium coil, also known as "molecular individualism" [37]. Both single DNA experiments [26, 27] and simulations [95] have shown that the stretching dynamics vary widely from molecule to molecule due to the random initial conformation of the polymer: some coils can be elongated quickly, others, such as folded conformations, require much higher strain for full extension. Often a strain of at least 10 is needed for the majority of DNA in an ensemble to reach steady-state extension [96] which is difficult to achieve in most finite strain devices [32]. However, it is possible to control molecular individualism effects by preconditioning the initial configurational distribution [95]. Preconditioning technologies such as applying obstacle arrays [33] or hydrogel [32] have been developed and proven to be effective.

CHAPTER 3

Experimental

This chapter details the experimental methods, equipment, and procedures that we use to study single DNA dynamics in micro- and nano-channels. The main experimental techniques covered are DNA sample preparation and channel fabrication. Additionally, we summarize our microscope setup and methods for data acquisition.

3.1 Single-Molecule Fluorescent Microscopy

With current state of the art video microscopy techniques it is possible to directly observe the dynamics of single molecules of DNA. This is based on the observation of emitted light from excited fluorescent dyes that are attached homogeneously to the DNA backbone. The underlying approximation is that the observed dye emission intensity is directly proportional to DNA mass. Fluorescent dye YOYO-1 was used to visualize the dsDNA for all experiments in this thesis. The side effect of using YOYO-1 dye is that it slightly unwind the double-stranded backbone and therefore increase dsDNA's contour length. It is generally assumed that the contour length of the DNA increases linearly with the amount of bound YOYO-1 up to about 35% at a saturating dye concentration of 1 dye per 4 base pairs [97, 98].

The setup of the optical path to detect single DNA molecules is shown schematically in Figure 3.1. A light source is first filtered by the excitation filter to ~ 490 nm. The beam is then nearly completely reflected by the dichroic mirror towards the microscope objective and excites YOYO-1

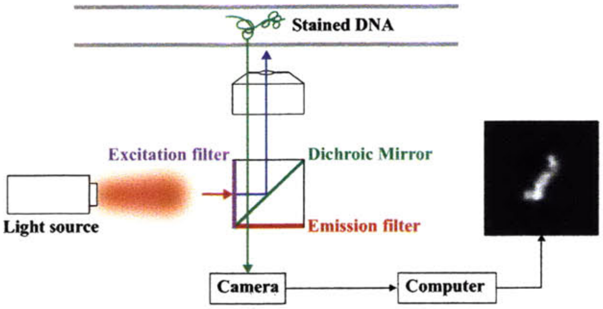

Fig. 3.1: *Schematic of the microscope setup.*

molecules bound to DNA. These dye molecules then emit light at ~ 510 nm which returns through the objective and passes through the dichroic, as 510 nm is in the high transmission portion of its spectrum. The emitted light is then sent to the camera through a final emission filter, which ensures that no stray transmitted excitation light can pass. The camera collects the emitted photons and converts them into electrons. As a result, the shape of the DNA backbone is transformed into digital images displayed in Scion Image software in a computer. Image or movie data are either recorded on digital video tapes or directly saved into computer hard drive using Scion Image software.

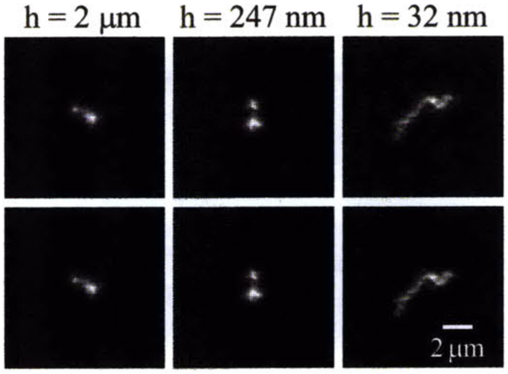

Fig. 3.2: *Examples of the raw (top) and processed (bottom) images of λ-DNA in the 2 μm, 247 nm, and 32 nm tall nanoslits.*

3.2 Data Analysis

We used custom-developed code in Interactive Data Language (IDL) to analyze experimental images and movies. These algorithms alow us to extract the DNA's center-of-mass position, radius of gyration tensor, orientation, and extension. Before these calculations we first remove the background of a raw DNA image. The background subtraction was performed for a selected square or rectangular region of the image (ROI) that encompasses the DNA feature and consists of two steps: (1) initial subtraction, and (2) individual noise spot removal. In step (1), the mean intensity of the pixels along the boundary of the ROI were calculated and subtracted from all pixels within the ROI. We also computed the standard deviation (σ) of the intensity for the pixels along the boundary of the raw ROI which will be used in step (2). In the second step we identified and removed the individual pixels that have non-zero intensity values but do not belong to the DNA signal. The criterion used to determine whether a certain pixel belongs to the DNA or is a noise spot is to examine the mean intensity of the adjacent pixels. Specifically, we calculated the mean intensity of the 6 pixels along the boundary of a 3×3 square centered at the pixel of interest as well as that of the 12 pixels along the boundary of a 4×4 square that surrounds the pixel of interest. If either of the mean intensities is less than 3σ, we took the pixel of interest to be a noise spot and set its intensity value to be zero. This routine was performed for all the pixels that have non-zero intensity values after the initial subtraction step. Figure 3.2 shows examples of both the raw images and the background removed images of λ-DNA confined in three nanoslits with different heights. It is seen that our algorithm effectively eliminates the background noise in the raw DNA image.

3.3 Channel Fabrications

Soft Lithography

We used soft lithography to construct channels taller than 1 μm. A schematic of the process is shown in Figure 3.3(A). Silicon master wafers containing the inverse channel structure protruding from the surface were fabricated by photolithography with the negative photoresist SU-8. Here we briefly summarize the photolithography procedure:

- Clean the silicon wafer in a piranha solution (H_2SO_4(%):H_2O_2(%)=3:1) for 10 min, rinsed in DI water and spin dry with nitrogen gas.
- Dehydrate the silicon wafer at about 100°C for 30 min.
- Apply adhesion promoter hexamethyldisilazane (HMDS) to the silicone wafer.
- Spin coat SU-8 onto the wafer, the spin speed varies depending on the thickness of the coating that is desired.
- Prebake at 90°C for 30 min.
- Expose the resist with near-UV light through a patterned photomask.
- Postbake at about 100°C for 30 min.
- Develop for the resist (i.e. dissolving the regions not exposed).
- Flood exposure of wafer with near-UV light.
- Deposit a monolayer of a silanizing agent ($Si\text{-}Cl_3\text{-}(CH_2)_2\text{-}(CF_2)_5\text{-}CF_3$) onto the wafer to allow easy peeling of PDMS later on. CAUTION: Hazardous solvent.

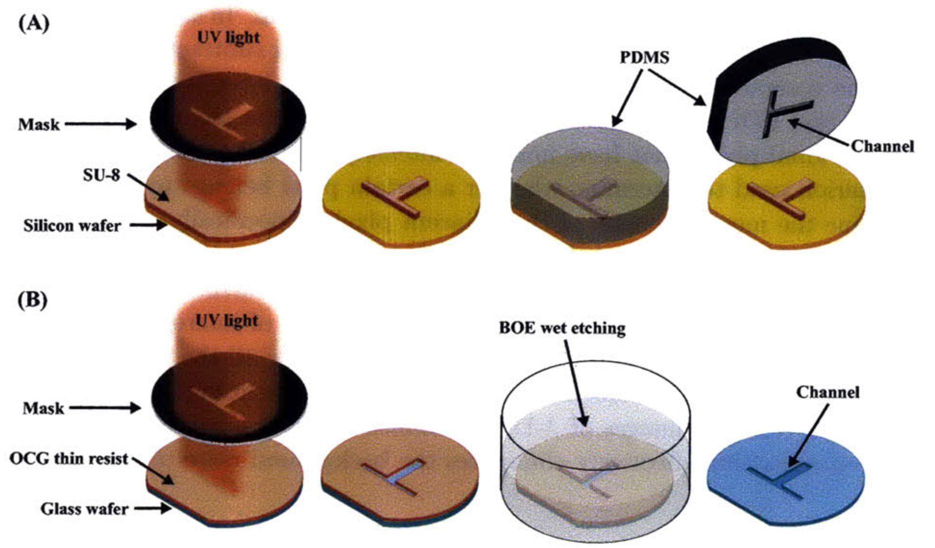

Fig. 3.3: *Schematic illustration of fabrication techniques. (A) Soft lithography. A negative photoresist SU-8 is spin-coated onto a silicon wafer, and exposed to UV light through a patterned mask, excess resist is removed and an inverse channel is formed. PDMS is poured over the master, cured and then peeled off from the master. (B) Fabrication of glass channels. A positive photoresist OCG is spin-coated onto a glass wafer, and exposed to UV light through a mask, exposed resist is removed so an channel is inserted into the resist layer. The wafer is etched in BOE etchant, remaining resist is removed after wet etching.*

To construct the PDMS channel, well mix 10 parts PDMS silicone elastomer and 1 part PDMS elastomer curing agent and pour onto the silicon master wafer. Leave the wafer at room temperature for about 1 hour until all the air bubbles have left the PDMS. Cure and mold the PDMS at 65°C for 24 hours. After peeling the PDMS, cut ~4 mm×4 mm holes at each end of a channel with a scalpel to serve as reservoirs. Cut around the borders of the channel to remove it from the mold. The PDMS channels are then cleaned by rinsing under ethanol and MQ. In most experiments, we soak the PDMS channels in diluted TBE (0.5×) or TE (1×) buffer at 45°C overnight to prevent permeation driven flow [99]. After soaking, the PDMS should be visibly foggy. We then gently dry the PDMS channel and seal it to a clean glass slide.

Glass Nanochannel Fabrication

We used the method developed by Mao and Han [100] to fabricate nanochannels on borosilicate glass wafers (Sensor Prep Services Inc., IL). A schematic of the process is shown in Figure 3.3(B). Here We briefly summarize the fabrication procedure:

- Clean the glass wafer in a piranha solution (H_2SO_4(%):H_2O_2(%)=3:1) for 10 min, rinsed in DI water and spin dry with nitrogen gas.

- Dehydrate the wafer at about 100°C for 30 min.
- Apply adhesion promoter hexamethyldisilazane (HMDS) to the glass wafer.
- Spin coat the wafer with OCG 825 positive resist.
- Prebake at 90°C for 30 min.
- Expose the resist with near-UV light through a patterned photomask.
- Postbake at about 100°C for 30 min.
- Develop for the resist (i.e. dissolving the regions exposed).
- Immerse the glass wafer in a commercial buffered oxide etchant (BOE 7:1) without agitation. The depth of the nanochannel can be well controlled by tuning the etching time. It is shown that BOE etches glass very fast initially (within 1 min) and then reaches a stable etch rate of 24 nm/min [100].
- Clean the glass wafers in piranha solution for 10 min to remove the remaining photoresist.
- Clean the glass wafer with another glass cover in piranha solution for 10 min.
- Soak both wafers in 28% ammonium hydroxide at 50°C for 30 min, rinse in DI water and spin dry with nitrogen gas.
- Align and press the two wafers together to make a spontaneous bonding. Carefully drive out all the air bubbles left in between the wafers.
- Thermally bond the wafers in a programmable furnace (Model BF51894C-1, Lindberg/Blue M, NC) at 550°C for about 15 hours with a ramp rate of 1.1°C/min and a cool down rate of 1.75°C/min.

3.4 DNA Sample Preparation

Required chemicals

- *MilliQ Ultrapure Water (MQ)*: The water we use is from the MilliQ Biocel A10 (Millipore). It provides deionized, filtered, UV treated water with a resistivity of 18.2 MΩ-cm, TOC 1-10 ppb, and filtered with 0.22 μm filters.
- *Concentrated buffer*: 5× TBE buffer (0.45 M Tris Base, 0.45 M Boric acid, and 10 mM EDTA), 100× TE buffer (1 M Tris-HCl and 100 mM EDTA), and 1 M Tris-HCl buffer. All buffers were filtered with a 0.2 μm filter before use.
- *Concentrated DNA (500 μg/mL λ DNA and 390 μg/mL T4 DNA)*: λ-DNA (48.5 kbp) was purchased from New England Biolabs and T4 DNA (165.6 kbp) was purchased from Nippon Gene. Both stock solutions were kept at -20°C.

- *1000 μM YOYO-1 dye*: The dye was purchased from Invitrogen in a solution of DMSO. The stock dye solution is continuously kept at -20°C and 15 μm samples are partitioned and kept at 4°C for 3-month use. Extreme care must be taken to ensure that the 1000 μM stock solution is well-mixed before partitioning.

- *β-mercaptoethanol (BME)*: This oxygen scavenger performs best when not exposed to air. Consequently, we limit the number of times that the stock container is opened and closed by partitioning smaller 2 mL aliquots for monthly use. CAUTION: Hazardous chemical.

- *Polyvinylpyrrolidone (PVP), Mw 10000*: PVP (Polysciences) is a nonionic polymer used to quench electroosmotic flow. We prepared 1% (wt/vol) stock solution for daily usage.

- *Glucose oxidase and catalase*: The enzymes glucose oxidase (Sigma, Catalog No. 49180) and catalase (Sigma, Catalog No. C100) were used to slow down the oxidative damage to stained DNA molecules.

Preparing Diluted DNA Stock Solution

The concentrated DNA stock solutions were diluted to 10 μg/mL in desired buffer and stored at 4°C for further staining procedures.

- Thaw the 500 μg/mL λ-DNA and 390 μg/mL T4 DNA stock solution at higher temperature and let sit at 4°C for one or two days to equilibrate the solution so that the DNA concentration is uniform.

- Make 10 μg/mL DNA solution: pipette

Buffer	490 μL
500 μg/mL λ DNA	10 μL

  or

Buffer	487.18 μL
390 μg/mL T4 DNA	12.82 μL

  into a 2 mL centrifuge tube (flat bottom). Use a cut-tip to slowly pipette the DNA solution in order to reduce shearing of the DNA, drag out the tip from the master solution very slowly to avoid viscoelastic recoil.

- Purge headspace with Argon and wrap in Aluminum foil. Let sit for a few weeks (one week at least) to allow the DNA concentration to be homogeneous.

- To ensure a uniform concentration of the 10 μg/mL DNA solution, make sure to let the solution sit for long enough time. For λ-DNA, the solution can be manually mixed to shorten the time required before the sample is ready for use. Simply use a 200 μL pipette with a cut-tip to pipette liquid off the buttom of the tube and pipette it back out while making a swirling motion. Since T4 DNA is much longer than λ DNA and thus more fragile, it is not advised to perform the manual mixing step, instead, gently swirl the solution and let it sit.

- For λ-DNA, heat the diluted sample on a hotplate set at 65°C for 1 hour to eliminate any possible hybridized DNA concatemers, and rapidly cool down using an ice pack. This heating step is not necessary for T4 DNA sample.
- The diluted DNA solution is ready for use.

Staining DNA with YOYO-1

- Degas and filter buffer.
- Prepare 10 μM YOYO-1 solution: pipette 0.4 μL 1000 μM YOYO-1 into 39.6 μL buffer, purge headspace with Argon and wrap in Aluminum foil. Vortex the solution for about 15 s. The final solution displays a light yellow color that can be visually identified if the YOYO-1 stock solution is still good. **It is advised to always prepare fresh diluted YOYO-1 solution when staining DNA.**
- Stain DNA: pipette

Buffer	129.8 μL
10 μM YOYO-1	3.9 μL
BME	6.0 μL
10 μg/mL DNA solution	10.3 μL

into a 0.6 mL centrifuge tube. Purge headspace with Argon and vortex the tube after adding BME. Slowly pipette 10 μg/mL DNA solution with a cut-tip. The dye molecule to basepair ratio for this recipe is 1:4. The final composition for the stained DNA solution is 4% (vol/vol) BME and 0.6867 μg/mL DNA.

- When pipetting 10 μg/mL DNA stock solution into the tube, it is advised to pipette it out into different regions of the solution inside the tube in order to shorten the time needed to achieve a uniform DNA concentration. Also, for λ-DNA, the final solution can be gently swirled to enhance mixing.
- Purge headspace with Argon and wrap in foil, let the solution sit at room temperature overnight.
- Before use, heat the stained DNA to 55°C for 1 hour and cool down with an ice pack.

Anti-Oxidant Enzymes

In all the experiments with glass channels, we have incorporated an anti-oxidant enzyme system consisting of glucose, glucose oxidase, and catlase to slow down the oxidant damage to the stained DNA molecules. The combination of glucose oxidase and catalase, in the presence of glucose, can consume 1/2 mole of O_2 per mole of glucose:

$$C_6H_{12}O_6 + O_2 \xrightarrow{\text{Glucose oxidase}} C_6H_{10}O_6 + H_2O_2 \tag{3.1}$$

$$H_2O_2 \xrightarrow{\text{Catalase}} H_2O + \frac{1}{2}O_2 \tag{3.2}$$

Reactive oxygen formed from molecular oxygen in solution causes both photobleaching of the dye and damage of DNA bases. Including glucose, glucose oxidase, and catalase in the solution can significantly suppress these effects in glass channels. Note that the enzymes do not work in the PDMS channels, possibly due to that the enzymes denature on a PDMS surface [101]. We summarize the procedures for incorporating the enzymes below. The protocol was developed for 0.5× TBE and should be modified accordingly when using different buffers.

- Prepare 30% (wt/vol) glucose solution in 0.5× TBE:
    1. "Solution A": dissolve 6 g glucose into 14 mL 1× TBE, mix well. The final volume of the solution becomes about 17.5 mL.
    2. "Solution B": dissolve 6 g glucose into 14 mL water, mix well. The final volume of the solution becomes about 17.5 mL.
    3. Add about 10.5 mL "Solution B" to "Solution A" to make a final volume of 28 mL. Mix well.
    4. Syringe the final solution through a 0.2 μm filter into a 50 mL Falcon tube.
- Degas and filter 0.5× TBE buffer.
- Prepare catalase solution: 7.8 μL catalase (aqueous suspension, Sigma, Catalog No. C100) + 154.2 μL 0.5× TBE.
- Dissolve glucose oxidase (powder, Sigma, Catalog No. 49180) into 0.5×TBE to make a final concentration of 0.1 mg/60 μL.
- **Both the glucose oxidase and catalase solution should be stored at 4°C and are only good for daily usage.**
- Add glucose, glucose oxidase, and catalase solutions into stained DNA sample before loading the sample into glass channels. In a final solution volume of 500 μl, include

30% glucose	19 μL
Catalase solution	5 μL
Glucose oxidase solution	50 μL

  add glucose oxidase at last. **For the correct functioning of these enzymes, make sure to include BME in the solution.**

λ-DNA Ligation

λ-DNA has 12 complimentary nucleotides at each end of the backbone that are single-stranded overhangs. The ends of multiple λ-DNA molecules can link together to form concatemers. The linking is a self-assembly process where first the complimentary nucleotides come into contact and hybridize. Then a ligase enzyme and ATP act to chemically bond one piece of λ-DNA to another. The procedures we developed to prepare λ-DNA concatemers are summarized below:

- Add 80 μL MQ, 10 μL 10× T4 DNA Ligase buffer, and 10 μL 500 μg/mL λ-DNA into a 0.6 mL centrifuge tube.

- Heat the mixture on a hotplate set at 65°C for 10 min and let the solution slowly cool down (usually by letting the solution cool down with the hotplate) until it reaches room temperature. This step hybridizes the λ-DNA molecule.
- Add 3 μL T4 DNA ligase, gently mix, and incubate at room temperature. The incubation time can vary based on the desired final length of the concatemer although the resulting concatemers are always highly polydisperse. Our past experience suggests that a 30 min incubation will result in mostly λ-DNA 3-mer to 7-mer, and a 60 min incubation can generate a majority of much longer concatemers (10-mer and above).
- Heat to 65°C for 20 min to denature the enzyme and break any non-ligated DNA.

The resulting ligated DNA sample can either be directly diluted to 10 μg/mL by adding 400 μL of 0.5× TBE for short term use (one week) or be purified by centrifugation (see section 3.5 for detailed protocol) and then stored in 0.5× TBE for longer term usage (one month).

3.5 Attaching Quantum Dots to λ-DNA

In this section we summarize the experimental protocols we developed to label the two termini of λ-DNA with quantum dots. The protocol for end-labeling λ-DNA is adopted from the work of Perkins [102] and relies on the existence of the two 12 bp overhangs at the ends of λ-DNA. The overhangs can not only be used to construct concatemers but also be differentiated with functionalized oligonucleotides. For the attaching of quantum dots, we first ligate biotinylated oligonucleotides to both overhangs, and then add in streptavidin coated quantum dots. Streptavidin is a multimeric protein consisting of four identical domains, each of which can bind a biotin molecule (see Figure 3.4A). Therefore, the quantum dot will attach to the ends of the DNA via this biotin-streptavidin linkage. In table 3.5 we list the sequences of the two overhangs of λ-DNA and the biotinylated oligonucleotides used to differentiate the ends. The oligonucleotides were synthesized by Integrated DNA Technologies (IDT) and stored in 1×TE buffer at a concentration of 100 μM.

Table 3.1: *Sequences for the two overhangs of λ-DNA and the biotinylated oligonucleotides (Biotin-side-A and Biotin-side-B).*

Name	Sequence (5' to 3')
λ-DNA end A	GGGCTGCGACCT
λ-DNA end B	AGGTCGCCGCCC
Biotin-side-A	Phosphate-AGGTCGCCGCCC-Biotin
Biotin-side-B	Phosphate-GGGCTGCGACCT-Biotin

A detailed protocol for end-labeling λ-DNA with quantum dots is given below:

1. Ligating oligonucleotide Biotin-side-A to λ-DNA:
   - Add 180 μL 10 mM Tris-HCl (pH 8.0) and 20 μL 500 μg/mL λ-DNA into a 0.6 mL centrifuge tube.

- Heat the mixture on a hotplate set at 65°C for 10-15 min to break any naturally formed concatemers, and rapidly cool down to room temperature on an ice pack. ("Solution A")
- Add 67 μL MQ, 30 μL 10× T4 DNA ligase buffer into another 0.6 mL centrifuge tube, mix well, and then add 3 μL 100 μM oligonucleotide Biotin-side-A to make 100 μL solutions, mix well. ("Solution B")
- Add "Solution B" to "Solution A", gently pipette the whole solution several times using a 200 μL pipette with a cut-tip. The final concentration of oligonucleotide is about 1000 fold that of λ-DNA. Let the solution sit overnight at room temperature to allow the oligonucleotide to hybridize to DNA.
- Add 10 μL T4 DNA ligase, gently mix using a 200 μL pipette with a cut-tip, and incubate at room temperature for 2 hours.
- Heat to 65°C for 20 min to denature the enzyme. ("Solution C")

2. Remove excess oligonucleotides by centrifugation using Centricon filters (100000 MWCO, Amicon):
    - For each centricon, measure the total weight of the cup and cap.
    - Pre-spin the centricon with 1× TE buffer to prevent non-specific sticking of the DNA to the centricon. Add 2 mL 1× TE to the centricon, spin at 2000G for 5 min at room temperature. There should be about 100 μL of liquid in the retenate of the centricon.
    - Fill centricon with 1 mL 1× TE buffer, add "Solution C" and then fill up to 2 mL with 1× TE. Spin at 1800G until there is 100-200 μL of liquid in the retenate of the centricon. Usually this requires 15-20 minutes of spin.
    - Slowly fill the centricon up to 2 mL with 10 mM Tris-HCl, spin again at 1800G until there is 100-200 μL of liquid in the retenate of the centricon. Repeat this step for another three times.
    - Add the cup to the top of the centricon, flip it over and spin at 600G for 2 min. Cover the cup with cap and measure the weight of the resulting sample. Subtracting the weight of the cup and cap gives the weight of the solution. Assuming the density of the solution is equal to that of water, the final volume of the solution, as well as DNA concentration (assuming all the original DNA is recovered), can thus be estimated.
3. Ligating oligonucleotide Biotin-side-B to λ-DNA:
    - Based on the volume of DNA solutions from the previous step, make adequate amount of buffer solutions containing 10× T4 DNA ligase buffer and 3 μL 100 mM oligonucleotide Biotin-side-B. Mix the buffer with DNA solutions. The final salt concentration should be 1× T4 DNA ligase buffer. Let the solution sit overnight at room temperature.
    - Add 10 μL T4 DNA ligase, gently mix using a 200 μL pipette with a cut-tip, and incubate at room temperature for 2 hours. Heat to 65°C for 20 min to denature the enzyme.
    - Repeat the centrifugation step to remove excess oligonucleotides. Control the final volume of solution to be between 150 and 200 μL. ("Solution D")

4. Attach biotinylated DNA to streptavidin coated quantum dots:

    - Based on the concentration of DNA in "Solution D", add suitable amount of streptavidin coated quantum dots (Invitrogen) such that the concentration of quantum dots is about twice the DNA concentration. Also, add NaCl to the solution to make a final concentration of 50 mM. Incubate the resulting solution at 4°C at least overnight, incubation for 2-3 days is recommended.

Results of the end-labeling protocol are examined by staining and then combing DNA on a polystyrene coated glass slide and imaging them using fluorescence microscopy. Figure 3.4B shows a typical image of λ-DNA molecules with either one or both ends attached to quantum dots. Currently the labeling yield is still not ideal: about 90% for single-end labeling and less than 50% for dual-end labeling. The protocol has yet to be optimized to increase labeling yields.

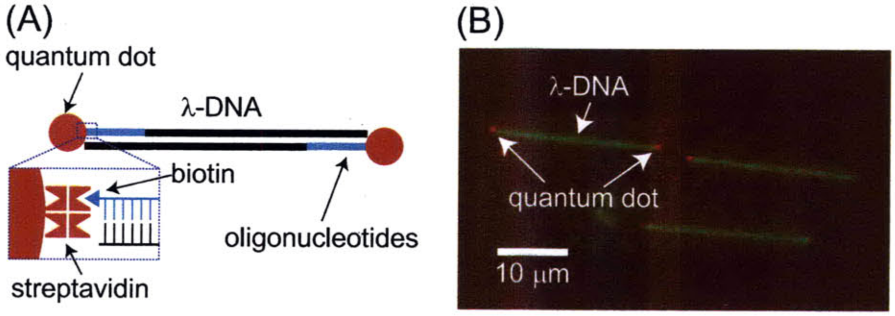

Fig. 3.4: *(A) Schematic of using streptavidin coated quantum dot to label λ-DNA termini. (B) Sample fluorescent image of end-labeled λ-DNA molecules. The quantum dots are in red and the DNA in green.*

CHAPTER 4

Stretching DNA in Micro T-channel

Controlled trapping and stretching of DNA molecules is critical for single molecule genomic studies. In this chapter we present a microfabricated T-junction which can trap and stretch single, free DNA molecules using electrophoretic forces. The device does not require special end-functionalization of the DNA. We show that two physical mechanisms of stretching can occur depending on the length of the DNA relative to the channel width in the junction region. Stable trapping and stretching of DNA molecules up to lengths of 485 kilobasepairs is demonstrated.

4.1 Introduction

The ability to trap and stretch biopolymers is important for a number of applications ranging from single molecule DNA mapping [11] to fundamental studies of polymer physics [41]. Optical or magnetic tweezers can be used to trap and stretch single DNA molecules, but they rely on specific modification of the DNA ends [103]. Alternatively, one end of the DNA can be held fixed and the molecule stretched with an electric field [91] or hydrodynamic flow [97]. Untethered *free* DNA can be driven into nanochannels to partially stretch molecules [16, 104]. Hydrodynamic planar elongational flow generated in a cross-slot geometry has been used to stretch free DNA [26] but trapping a molecule for a long time at the stagnation point is not trivial [28]. Electric fields have been used to either confine molecules in a small region in a fluidic channel [105] or to partially stretch molecules as they electrophorese past obstacles [40,65,106], into contractions [32] or through cross-slot devices [31]. Partial stretching occurs in these aforementioned electrophoresis devices because the molecule has a finite residence time [32]. Currently, simple methods do not exist to trap *and* stretch DNA or other charged biomolecules.

DNA can be physically envisioned as a series of charges distributed along a semiflexible Brownian string. Molecules can be electrophoretically stretched due to field gradients that vary over the length scale of the DNA. Ajdari and coworkers [38] have previously shown that analogies exist between the deformation of a DNA molecule in hydrodynamic flow and deformation due to electrophoresis in an electric field. Deformation of a DNA will depend upon the details of the kinematics of the electric field [40, 106]. Electric fields are quite unusual in that they are purely elongational [31, 40, 106]. Here we present a microfluidic device which is able to trap and stretch biomolecules using electric field gradients.

4.2 DNA Deformation in Electric Fields

Our group has previously characterized DNA dynamics in electric fields in micro- and nano-devices [40, 56, 107], which we briefly summarize here. Our analysis considers large double-stranded DNA molecules, typically of size 50-1000 kbp ($\sim$ 0.01-1% of a typical human chromosome), and free of all *in vivo* proteins. The DNA molecule can be modeled as a polymer and can be characterized using its contour length L_c, persistence length p, diffusivity D, and longest relaxation time τ. The diffusivity D is given by $D = k_\mathrm{B}T/\zeta$ where k_B is Boltzmann constant, T is absolute temperature and ζ is the drag coefficient of the molecule. The large DNA molecules considered here have $L_c/p \gg 1$ thus still act like flexible polymers and adopt coiled configurations at equilibrium in aqueous solvents. At moderate pH, DNA is also a uniformly negatively charged polymer due to its phosphate backbone. Consequently, they perform electrophoresis under an applied electric field. In a thin Debye length (κ^{-1}) solvent with $\kappa^{-1} \ll p$, the motion of the free counterions in the double layer outside DNA's backbone screens the hydrodynamic interactions between chain segments due to electrophoresis [40] and cancels out all size-dependent components in the motion of each chain segment. As a result, in a pure uniform electric field, the coil moves without average deformation at a size-independent velocity $\mu\mathbf{E}$ where μ is the electrophoretic mobility. In electric field gradients or the simultaneous presence of forces and uniform electric fields where a DNA molecule deforms, the hypothesis of electrohydrodynamic equivalence [38] applies, suggesting that the effect of an electric field $\mathbf{E}$ is equivalent to a flow field with velocity $\mu\mathbf{E}$. Therefore, at low fields, we can use the same kinematic approach to study electrophoretic deformation as has been used in the past to study hydrodynamic deformation. In electric field gradients, the governing dimensionless group is the Deborah number $\mathrm{De} = \dot{\epsilon}\tau$ where $\dot{\epsilon}$ is the electrophoretic strain rate (positive eigenvalue of $\mu\nabla\mathbf{E}$). In a homogeneous elongational electric field where the strain rate $\dot{\varepsilon}$ is constant everywhere, theory [94] suggests the coil-stretch transition occurs when Deborah number is above a critical value of $\mathrm{De} = 0.5$. If a DNA tethered at one end is stretched in a uniform electric field, by balancing the electric force exerted on the chain and the entropic restoring force of the chain, we can obtain a dimensionless electric Peclet number which governs the stretching of the chain [107]: $\mathrm{Pe} = \mu|\mathbf{E}|p/D$.

4.3 Device Geometry

We investigate the stretching of DNA molecules in a symmetric channel consisting of a narrow T-shape part in the center and three identical wide parts outside as shown in Fig. 4.1(a). The vertical part and horizontal part of the T-junction have the same length l_2 while the width of the vertical part is twice the width of the horizontal part: $w_2 = 2w_3$. Hence the T-junction is equivalent to half of a cross-slot channel. The dimensions used in this study were: $l_1 = 1\,\text{mm}$, $l_2 = 3\,\text{mm}$, $w_1 = 80\,\mu\text{m}$, $w_2 = 40\,\mu\text{m}$, and $w_3 = 20\,\mu\text{m}$. In order to suppress the local electric field strength maximum, the two corners of the T-junction were rounded using an arc with radius $R = 5\,\mu\text{m}$ (Fig. 4.1(c)). When symmetric potentials are applied to the channel in a manner as shown in Fig. 4.1(b), a local planar elongational electric field with a stagnation point can be obtained within the T-junction and uniform fields in the three straight arms. We use $\mathbf{E}_1$ and $\mathbf{E}_2$ to represent the uniform electric field obtained in uniform region 1 and uniform region 2, respectively.

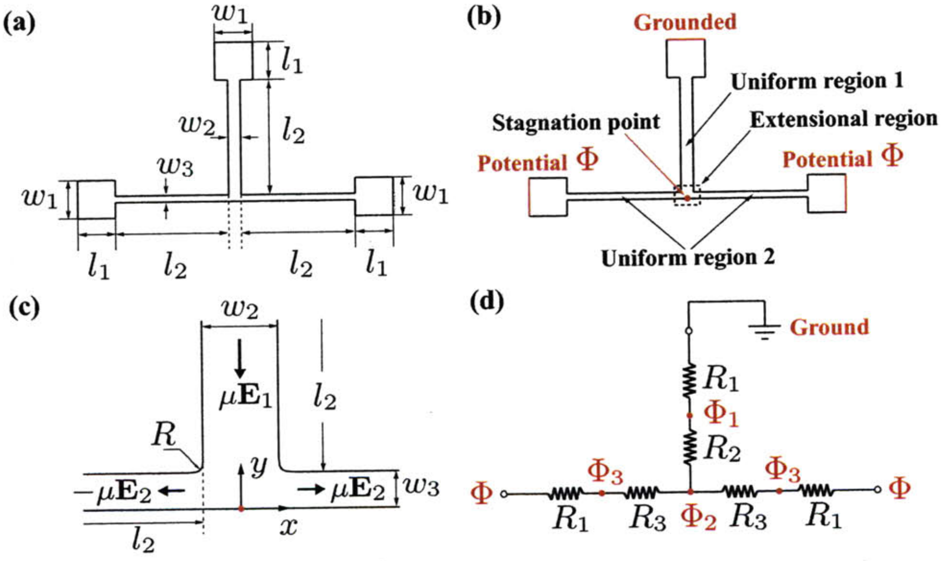
(a)
w_1
l_1
w_2
l_2
w_3
w_1
w_1
l_1
l_2
l_2
l_1
(b)
Grounded
Uniform region 1
Stagnation point
Extensional region
Potential Φ
Potential Φ
Uniform region 2
(c)
w_2
$\mu\mathbf{E}_1$
l_2
R
y
$-\mu\mathbf{E}_2$
$\mu\mathbf{E}_2$
w_3
x
l_2
(d)
Ground
R_1
Φ_1
R_2
Φ_3
Φ_3
Φ
Φ
R_1
R_3
Φ_2
R_3
R_1

Fig. 4.1: *Schematic diagrams of (a) channel geometry, (b) location of uniform/ elongational fields and stagnation point, (c) expanded view of T-junction, and (d) circuit analogy of the channel.*

Because l_1, $l_2 \gg w_3$, a simple circuit as shown in Fig. 4.1(d) can be used to analogize this channel. The center T-junction region is neglected and each straight part of the channel is represented with a resistor with resistance proportional to l/w. The potential at each point indicated in

Fig. 4.1(d) can be solved analytically. Results are given by:

$$\begin{aligned}
\Phi_1 &= \frac{2l_1(w_3/w_1)}{3l_1(w_3/w_1)+2l_2}\Phi \\
\Phi_2 &= \frac{2l_1(w_3/w_1)+l_2}{3l_1(w_3/w_1)+2l_2}\Phi \\
\Phi_3 &= \frac{2l_1(w_3/w_1)+2l_2}{3l_1(w_3/w_1)+2l_2}\Phi
\end{aligned} \tag{4.1}$$

The resulting field strengths in uniform region 1 and 2 are given by:

$$|\mathbf{E}_1| = |\mathbf{E}_2| = \frac{\Phi}{3l_1(w_3/w_1)+2l_2} \tag{4.2}$$

As a result, the resulting extensional field in the T-junction is nearly homogeneous. The electrophoretic strain rate is approximately given by $\dot{\epsilon} \approx \mu|\mathbf{E}_1|/w_3$ where μ is the electrophoretic mobility. For the remaining analysis, we non-dimensionalize the variables:

$$\widehat{x} = \frac{x}{w_3}, \quad \widehat{y} = \frac{y}{w_3}, \quad \widehat{\mathbf{E}} = \frac{\mathbf{E}}{|\mathbf{E}_1|}, \quad \widehat{\dot{\epsilon}} = \dot{\epsilon}\frac{w_3}{\mu|\mathbf{E}_1|} \tag{4.3}$$

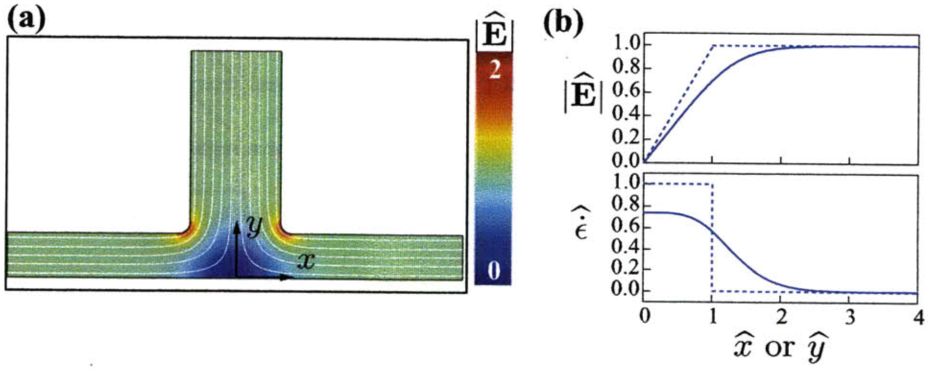

Fig. 4.2: *(a) Dimensionless electric field strength in the T-junction region from finite element calculation. The white lines are the electric field lines. (b) Dimensionless electric field strength and strain rate along the* $\widehat{y} = 0$ *or* $\widehat{x} = 0$ *trajectory. The dotted lines are for an ideal T-junction without entrance or exit effects.*

In Fig. 4.2(a) we show a finite element calculation of the dimensionless electric field strength $|\widehat{\mathbf{E}}|$ in the region around the T-junction. We assume insulating boundary conditions for the channel walls. Although the corners have been rounded, there is still a small local maximum in field strength at the corners. The magnitude of this maximum is ~ 2 times greater than $|\mathbf{E}_1|$. If no rounding is applied, this magnitude is much higher (~ 20 times greater than $|\mathbf{E}_1|$, data not shown). Fig. 4.2(b) shows the dimensionless field strength and strain rate in the junction. Due to symmetry, the data along $\widehat{y} = 0$ and $\widehat{x} = 0$ overlap. The electric field and strain rate for an idealized T channel without any end effects are indicated by the dotted lines. The entrance (or exit) region starts at about 30% of the length w_3 before the entrance (or exit) of the T-junction and extends a full length of w_3 into the uniform straight region. Within the T-junction, there is a homogeneous elongational field, but the strain rate is $\approx 0.74\mu|\mathbf{E}_1|/w_3$ due to entrance/exit effects.

4.4 Experiments

We use soft lithography [108] to construct $2\,\mu$m tall PDMS (polydimethylsiloxane) microchannels. A 10:1 PDMS crosslinking agent (Sylgard 184, Dow) was mixed and poured onto a Si master wafer containing positive-relief microchannels patterned in SU-8 photoresist (Microchem). The Si wafer was pretreated with a fluorinated silane monolayer (United Chemical Technologies) to prevent cured PDMS from sticking to the Si master. After pouring, the PDMS was cured at 65 °C for 20 h. Reservoirs (4 mm×4 mm) were cut at each end of the PDMS microchannel with a scalpel. The channels were soaked for 20 h at 45 °C in 5×TBE buffer to eliminate permeation driven flow [99]. T4 DNA (165.6 kbp, Nippon Gene), λ-DNA (48.5 kbp, New England Biolabs), and λ-DNA concatomers (integer multiples of 48.5 kbp from end-to-end ligation) were used in this study. DNA were stained with YOYO-1 (Invitrogen) at 4:1 bp:dye molecule and diluted in 5×TBE (0.45 M Tris-Borate, 10 mM EDTA) with 4 vol% β-mercaptoethanol (CabioChem). The stained contour lengths are $70\,\mu$m for T4 DNA and integer multiples of $21\,\mu$m for λ-DNA concatomers. Glass slides were first rinsed in 95% ethanol and deionized water (Milli-Q, Millipore), soaked in 1 M NaOH for 1 h, rinsed in water again, and then plasma treated at 100 W for 30 s, charge equilibrated for 15 h. The PDMS channel was rinsed in deionized water and dried in Argon stream, and applied to the cleaned glass slide. We then immediately loaded DNA solution into the channel. One platinum electrode was placed into each reservoir. The bottom two electrodes were connected to two separate DC power supplies, and the top electrode was grounded. We observed single DNA molecule dynamics using an inverted fluorescence microscope (Axiovert 200, Zeiss) with either a 63× NA 1.4 oil-immersion objective (Zeiss) or a 40× NA 0.75 air objective (Zeiss). Images were captured at 30 frames per second with an EB-CCD camera (C7190-20, Hamamatsu) and NIH software.

4.5 Electric Field Characterization

The electric field generated in the T-junction was experimentally verified by tracking the center of mass of DNA under conditions in which they do not appreciably deform. We chose to use λ-DNA (48.5 kbp) as it is large enough to easily track, but small enough to not appreciably deform at the conditions used below. Tracking was performed at an applied electric field $|\mathbf{E}_1| = |\mathbf{E}_2| = 30\,\mathrm{V/cm}$. Fig. 4.3(a) shows the trajectories of 34 λ-DNA molecules passing through the T-junction. We determined the ensemble average electrophoretic velocity in the two uniform regions to be $\langle \mu|\mathbf{E}_1| \rangle = 40 \pm 4\,\mu\mathrm{m/s}$. The electrophoretic mobility of λ-DNA is thus $\mu = 1.35 \pm 0.14 \times 10^{-4}\,\mathrm{cm^2/(s\,V)}$. According to the results of the finite element calculation, the strain rate in the extensional region should be $\dot{\epsilon} \approx 0.74\langle \mu|\mathbf{E}_1| \rangle / w_3 = 1.48 \pm 0.15\,\mathrm{s^{-1}}$. The relaxation time of λ-DNA in the experimental buffer has been previously measured [40] to be $\tau = 0.19\,\mathrm{s}$. Therefore, the Deborah number for the λ-DNA is $\mathrm{De} = \tau\dot{\epsilon} = 0.3$, smaller than 0.5.

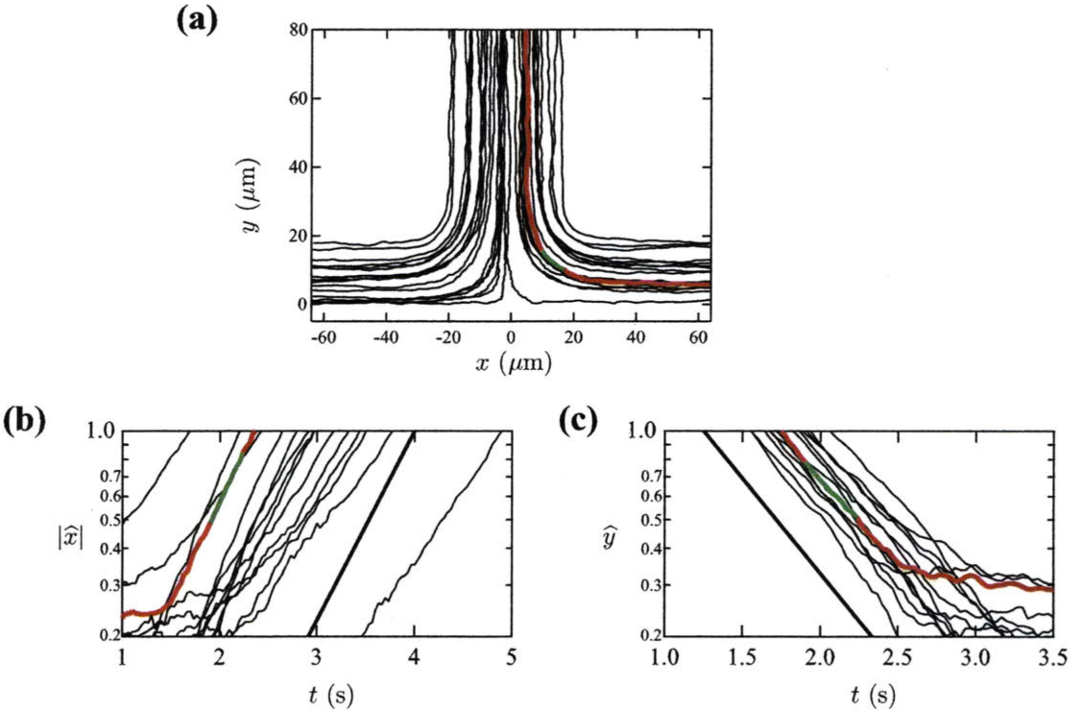

Fig. 4.3: *(a) Trajectories of 34 λ-DNA electrophoresis for field characterization (*$|\mathbf{E}_1| = 30\,\mathrm{V/cm}$*). (b) Semilog* $\widehat{x}(t)$ *traces for 15 of the above trajectories which have crossed the homogeneous extensional region. (c) Semilog* $\widehat{y}(t)$ *traces for the same 15 trajectories. The red thick line is an example λ-DNA trajectory that has experienced the homogeneous extensional field and the green line is the part used to extract the experimentally observable strain rate* $\dot{\epsilon}_{\mathrm{obs}}$*. The black thick lines in (b) and (c) are the affine scaling using* $\dot{\epsilon} = 1.49\,\mathrm{s}^{-1}$.

An experimentally observable strain rate was extracted from the data independently. 15 molecules which have experienced the extensional field were selected, and the portion of their trajectories located in the homogeneous extensional region was cropped and the $\widehat{x}(t)$ and $\widehat{y}(t)$ data were fit to the exponential functions $\widehat{x}(t) = \widehat{x}(0)\exp(\dot{\epsilon}_{\mathrm{obs}}t)$ and $\widehat{y}(t) = \widehat{y}(0)\exp(-\dot{\epsilon}_{\mathrm{obs}}t)$, respectively. Based on the results of the finite element calculation, we only selected the portion of the trajectory with both $|\widehat{x}|$ and $\widehat{y}$ in the range of $[0,\, 0.8]$ for the fitting. In Fig. 4.3 we showed an example of the fitting using the red line to indicate a qualified DNA trajectory and the green line to indicate the part used for the fitting. The fitted ensemble average strain rate is $\langle\dot{\epsilon}_{\mathrm{obs}}\rangle = 1.49 \pm 0.4\,\mathrm{s}^{-1}$, in accord with the predicted value of $1.48 \pm 0.4\,\mathrm{s}^{-1}$. This result confirms that the field within the T-junction is nearly homogeneous and the magnitude is in quantitatively agreement with the simulation. Figure 4.3(b) and (c) show the semi-log plots of the $\widehat{x}$ and $\widehat{y}$ data of the 15 trajectories. The thick black line is the affine scaling using $\dot{\epsilon} = 1.49\,\mathrm{s}^{-1}$.

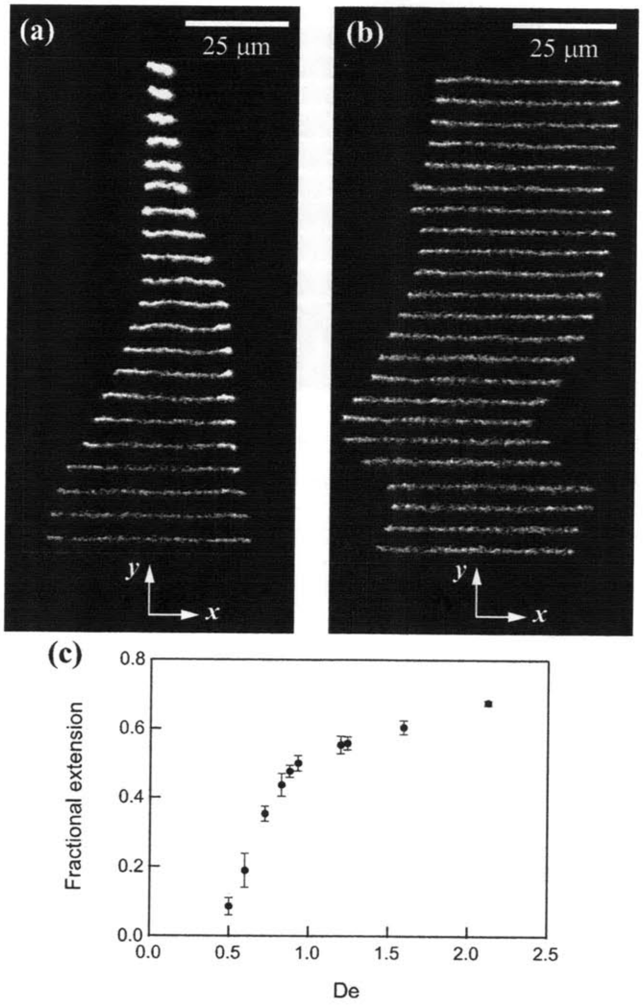

Fig. 4.4: *(a) Stretching of a T4 DNA trapped at the stagnation point in the T channel (0.17 s between images) at* De = 2.0. *(b) The steady state behavior of a T4 DNA (0.33 s between images). The molecule began to drift towards the left, then was pulled back by stagnation point control. (c) The mean steady state fractional extension of T4 DNA versus* De. *Each point represents the average of 15 to 30 molecules.*

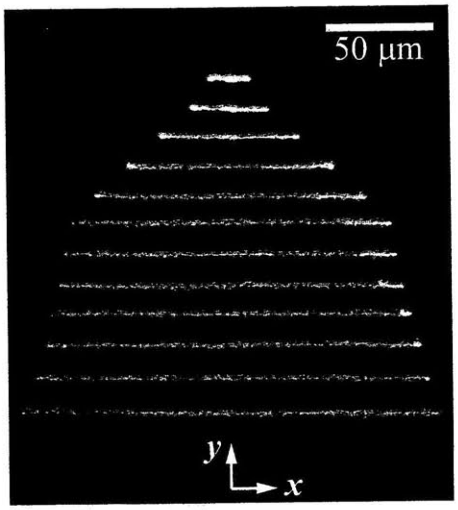

Fig. 4.5: *Stretching of a λ DNA 10-mer in the T channel (0.33 s between images) at* $|\mathbf{E}_1| = 45\,\mathrm{V/cm}$ *(*$\mathrm{Pe} \approx 52$*). For ease of presentation, each frame was centered at* $x = 0$.

4.6 Results and Discussion

In a typical experiment, we first applied symmetric potentials to electrophoretically drive DNA molecules into the T-junction region and then trapped one molecule of interest at the stagnation point of the local extensional field (Fig. 4.4(a)). With the application of two power supplies we were able to adjust the two potentials individually and therefore freely move the position of the stagnation point. This capability of stagnation point control allowed us to trap any DNA molecules in the field of view even it initially did not move toward the stagnation point. Furthermore, we could also overcome fluctuations of a trapped molecule. For example, if a trapped DNA begins to drift toward the right reservoir, the potential applied in the left reservoir can be increased so that the position of the stagnation point would reverse the direction of the drifting molecule (Fig. 4.4(b)).

The T4-DNA in Fig. 4.4 has a maximum stretch of $\approx 50\,\mu\mathrm{m}$ and extends just slightly beyond the region in the T-junction where homogeneous electrophoretic elongation is generated. The dimensionless group which determines the extent of stretching in this region is the Deborah number $\mathrm{De} = \tau\dot{\epsilon}$ where τ is the longest relaxation time of the DNA (measured to be $1.3 \pm 0.2\,\mathrm{s}$). In Fig. 4.4(c) we see that strong stretching occurs once $\mathrm{De} > 0.5$, similar to what is observed in hydrodynamic flows [26].

We next tried to stretch molecules which have contour lengths much larger than $2 \times w_3$ ($40\,\mu\mathrm{m}$). In Fig. 4.5 we show the stretching of a concatomer of λ-DNA which has a contour length of $210\,\mu\mathrm{m}$ (10-mer, 485 kilobasepairs). As the molecule enter the T-junction it is in a coiled stated with mean radius of gyration $\approx 2.7\,\mu\mathrm{m}$ [56]. Initially the stretching is governed by De due to the small coil size. However, as the arms of the DNA begin to extend into regions of constant electric field, stretching occurs due to a different mechanism. For stretched lengths $\gg 2 \times w_3$, the chain resembles a set of symmetrically tethered chains (with contour lengths one half that of the original chain) in a homogeneous electric field. Stretching still occurs, but is now governed by the $\mathrm{Pe} = \mu E p / D_{1/2}$ where μ is the electrophoretic mobility $(1.35 \pm 0.14 \times 10^{-4}\,\mathrm{cm}^2/(\mathrm{s\,V})\ )$, p is the persistence length $(\approx 53\,\mathrm{nm})$ and $D_{1/2}$ is the diffusivity of a chain with a contour length half that of the original chain ($\approx 0.062\,\mu\mathrm{m}^2/\mathrm{s}$ for this 10-mer [56]). The molecule in Fig. 4.5 reaches a final steady state extension which is 94% of the full contour length.

4.7 Conclusion

Our DNA trapping and stretching device has several advantages over other methods. Electric fields are much easier to apply, control and their connections have smaller lag-times than hydrodynamic fields in micro/nano channels. Further, the purely elongational kinematics of electric fields are advantageous for molecular stretching. The field boundary conditions also allow for the use of only 3 connecting channels to generate a homogenous elongational region and straightforward capture of a molecule by adjusting the stagnation point. Stretching can occur even beyond the elongational region due to a molecule straddling the T-junction and feeling a tug-of-war on the arms by opposing fields. The fabrication is also quite simple compared to nanochannels and the design allows for facile capture, stretch and release of a desired molecule.

CHAPTER 5

Stretching DNA in Slit-like Confinement

In this chapter we designed and fabricated a nanofluidic cross-slot device to investigate the effects of slit-like confinement on the electrophoretic stretching of single DNA molecules. The device is capable of trapping and stretching single DNA molecules at the stagnation point of a homogeneous planar elongational electric field. Different from studies of unconfined DNA, the longest relaxation time in slit-like confinement is extension dependent and we find the *higher extension* relaxation time allows better prediction of the drastic increase of extension with applied strain rate in confinement. The low extension relaxation time is important in polymer rotation and small deviations from equilibrium. This work was done in collaboration with Anthony G. Balducci.

5.1 Introduction

The development of nanofabricated devices capable of confining single DNA molecules creates the potential to alter and control the DNA shape and dynamics [43, 44, 45, 46]. A series of recent single molecule studies has characterized DNA conformation and dynamics at equilibrium in different types of confinement, for instance, tube-like [16, 25, 98, 109, 110, 111] (quasi 1-dimensional) confinement, and slit-like [56, 57, 59, 112] (quasi 2-dimensional) confinement. However, in a number of applications ranging from DNA separation [47, 113] to genomic mapping [8, 30], significantly deformed molecules are important. Recently, nanoconfinement in one-dimensional (tube-like) channels has been used to create highly extended DNA of interest in particular to direct mapping methods [16, 25, 98, 109, 110]. Here, we report a facile method for dynamically trapping and stretching single molecules in *slit-like* nanoconfinement at a stagnation point. The molecular extensions attained here match those in the most extreme tube-like confinement, but in slit-like channels with photolithographically defined dimensions three orders of magnitude larger than the tube-like case. Also, since stretching the polymer can alter the interactions of the polymer with the confining walls [66, 114], the dynamics of the molecule can vary with extension, making this problem interesting from a fundamental polymer physics standpoint. Even with a recent surge in the research being done in this area (see ref. [115] for a recent review), a complete understanding of polymer dynamics in confinement is lacking.

Recently, we found that in slit-like confinement the time scale governing the slowest stress relaxation of single DNA molecules depends on the molecule's extension [66]. Unlike Rouse or Zimm modes, the relaxation of the molecule very near equilibrium and at higher extensions is best described by two different time constants (see Figure 5.1): the low extension relaxation time τ_{II} and the higher extension relaxation time τ_{I}. In contrast, experiments on unconfined DNA show that a single time constant governs relaxation dynamics in the entire linear force regime (from equilibrium to approximately 30% fractional extension) [73]. We found that the emergence of the extension-dependent relaxation time is due to the presence of the confining walls. An initially stretched molecule is not sterically confined by the channel walls, but as it relaxes, the lateral dimensions of the molecule grow and the steric confining effects eventually become important. In a simple model which describes the polymer relaxation using a tension-blob framework (see Figure 5.1), the crossover point where the relaxation time changes occurs when the dimension of the blobs is equivalent to the height of the channel [66]. Before this point, relaxation happens through increasing the size of the tension blobs along the chain. During this process, the molecule is not sterically confined and the channel walls only act to alter the hydrodynamic drag through hydrodynamic screening [56]. After the crossover point, the blobs are sterically confined and can no longer grow. The confining walls also change the spring force of the molecule, in addition to modulating the hydrodynamic drag. The extension at the crossover point, termed as the crossover extension (X_{ex}^*, see Figure 5.1), can be estimated as $X_{\text{ex}}^* = hN_{\text{blobs}}$ where h is the channel height and N_{blobs} the number of blobs. By assuming good solvent quality within blobs, a scaling relationship for X_{ex}^* was derived [66] as $X_{\text{ex}}^* \sim h^{-2/3}p^{1/3}w^{1/3}L_c$, where p, w and L_c are the persistence length, effective width and contour length of the DNA, respectively. The crossover extension depends on the channel height, the size of the DNA, solvent quality, and ionic strength through dependencies in w and p. It is important to note that both relaxation times in confinement are significantly greater than the unconfined relaxation time, pointing to the fact that confinement may allow stretching of DNA molecules at smaller deformation rates, as described below. The purpose of this article is to examine the effects of these newly observed relaxation physics on the electrophoretic stretching of single DNA molecules in slit-like nanoconfinement.

Polymer deformation in homogeneous extensional flows or fields is a balance of the stretching forces applied by the flow or field and the polymer's entropic elasticity tending to recoil the molecule [116]. In the unconfined case, a dimensionless group termed the Deborah number is typically used to characterize this balance. The Deborah number is defined as the product of the deformation rate of the flow or field (the strain rate $\dot{\varepsilon}$) and the polymer's longest relaxation time (τ): De $= \dot{\varepsilon}\tau$. A large change in extension with De is found [26, 27, 117] to occur near the theo-

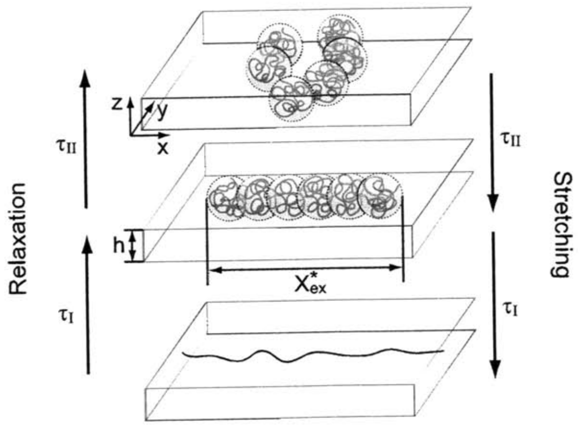

Fig. 5.1: *Schematic of the low extension relaxation time* (τ_{II}) *and the higher extension relaxation time* (τ_{I}) *of DNA in slit-like nanochannels and the possibility of their importance in DNA stretching. Extended molecules are no longer sterically confined, and thus have different stretching and relaxation dynamics.*

retically predicted [94] critical value of $\mathrm{De}_{\mathrm{crit}} \approx 0.5$. The fact that the longest relaxation time is extension-dependent in slit-like confinement brings some ambiguity to the prediction of where this drastic deformation occurs. Therefore, we define two Deborah numbers for the current problem and characterize the role of each in determining the DNA behavior. $\mathrm{De}_{\mathrm{I}} = \dot{\varepsilon}\tau_{\mathrm{I}}$ is defined using the higher extension relaxation time, which governs relaxation above the crossover extension X^*_{ex} to the onset of the linear force regime (approximately 30% fractional extension). $\mathrm{De}_{\mathrm{II}} = \dot{\varepsilon}\tau_{\mathrm{II}}$ is defined using the low extension relaxation time, which governs dynamics near equilibrium. The correct prediction of the required deformation rate to achieve a certain extension is important in the design of devices aiming to exploit confinement to manipulate DNA molecules [57,65].

5.2 Experiments

To investigate confinement-induced changes on stretching DNA, we place single DNA molecules in homogeneous extensional electric fields under varying degrees of confinement. Electric fields are employed to move and stretch DNA because the kinematics are purely elongational at lengthscales larger than the Debye length (here $\sim 3\,\mathrm{nm}$) and deformation due to shear can be neglected [40]. In addition, electric fields are much easier to implement than pressure-driven flows for nano-scale devices. In planar elongational electrophoretic deformation, the electrophoretic velocity of a point charge varies linearly with position:

$$v_x = \mu E_x = \dot{\varepsilon} x \tag{5.1}$$

$$v_y = \mu E_y = -\dot{\varepsilon} y \tag{5.2}$$

where v_x, v_y, are the velocities in the x and y directions, respectively, E_x and E_y are the electric fields in the x and y directions, respectively, μ is the electrophoretic mobility, and $\dot{\varepsilon}$ is the strain rate. Previous studies have used cross-slot [26, 27, 28, 31] and T [117] channels to achieve these kinematic conditions. In tall channels the large spans used to create O(100 μm) regions of constant strain rate are not an issue. However, even slight sagging due to large spans in nanochannels affects the strength of the field and may cause pinch-off of the channel. Cross-slot nanoslit channels with the incorporation of hyperbolically curved sidewalls (see Figure 5.2) are implemented in this study. Since the shape of the sidewalls matches exactly the streamlines in homogeneous extensional fields, there are no inhomogeneities to disrupt the linear electric field profile over the entire intersection region [79]. This development minimizes the span needed to create O(100 μm) regions of homogeneous deformation. Independent control of the potential applied to the side reservoirs allows movement of the stagnation point via manually providing slight perturbations to the field [117]. These small adjustments allow the entrapment of DNA molecules at the stagnation point for very high accumulated strains (up to 50 Hencky strain units = $\dot{\epsilon}t_{\mathrm{res}}$, where t_{res} is the molecule's residence time in the field). Furthermore, confinement of the molecule within the focal plane ensures it remains in focus for the entire observation.

5.2.1 Channel and DNA Preparation

The channels were prepared using two methods. Microchannels ($h = 2\,\mu$m) were constructed in polydimethylsiloxane (PDMS, Sylgard 184, Dow Corning) using soft-lithography on a silicon master (SU8-2 photoresist). The PDMSchannels were soaked in 0.5 × Tris-borate-EDTA (TBE, Omnipure) buffer at 40 °C overnight to eliminate permeation driven flow through the PDMS [99], rinsed and dried briefly, and sealed to a glass cover-slide. Glass nanochannels with two different heights ($h = 300\,$nm and $150\,$nm) were created by a photo-resist protected etch in buffered oxide etchant and thermally bonded to a glass cover slide as described previously [100]. The glass nanochannels were filled with filtered RO-water and rinsed overnight via application of potentials at the fluid reservoirs before use. All channels were rinsed with the experimental buffer prior to exposure to DNA molecules. The buffer contained 4% betamercaptoethanol (BME, Cabiochem) and 0.1% 10 kDa polyvinylpyrrolidone (PVP, Polysciences) in 0.5 × TBE. The experimental buffer in the glass nanochannels also incorporated a glucose (Mallinckrodt)/glucose oxidase (Roche) /catalase (Roche) ($12.5, 0.16, 7.4 \times 10^{-3}$ mg/mL, respectively) oxygen scavenging system to allow prolonged exposures required in the small channels. The channel was flushed with new buffer every two hours during experiments to ensure a constant ionic strength environment [58]. T4GT7 DNA molecules (165.6 kbp, radius of gyration $R_{\mathrm{g,unconfined}} = 1.46\,\mu$m [56], Nippon gene) and λ-DNA molecules (48.502 kbp, $R_{\mathrm{g,unconfined}} = 0.69\,\mu$m [56], New England Biolabs) were stained with YOYO-1 (Invitrogen) dye at a basepair to dye ratio of 4:1 and allowed to sit at least overnight. The persistence length of the DNA molecules under the experimental buffer condition is $p \approx 53\,$nm [58]. Our epifluorescence microscopy and detection setup as well as data analysis and extraction of the extension and principal axis of the radius of gyration tensor are described elsewhere [57, 66].

5.2.2 Electric Field Characterization

The electric field kinematics generated in the intersection region of all cross-slot devices were verified by tracking the center of mass of electrophoresing DNA under conditions in which they do not appreciably deform. λ-DNA was used as the tracer since both relaxation times (τ_{I} and τ_{II}) are not large enough to yield significant deformation at the electric fields employed. Figure 5.2C shows the center of mass position of 189 λ-DNA molecules as they electrophorese through the 2 μm tall

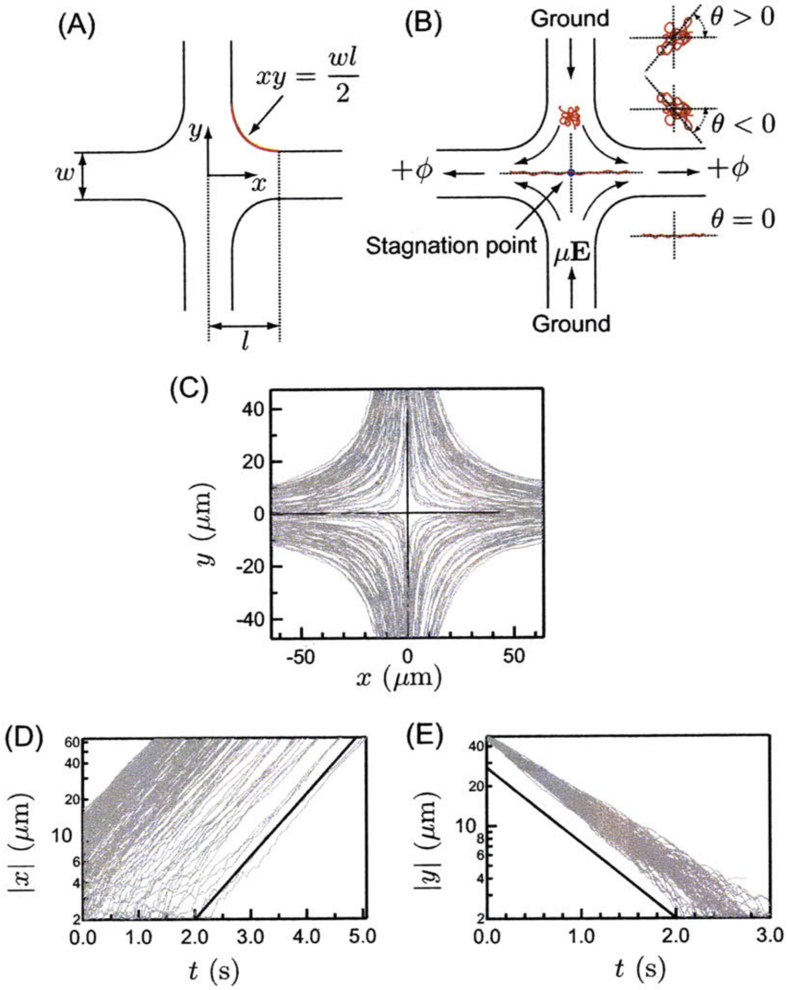

Fig. 5.2: *(A) Diagram of the cross-slot stretching device geometry. (B) Schematic of the motion and stretching of DNA molecules in the device. Independent applied voltages to the left and right arms of the channel allow adjustment of the location of the stagnation point and trapping of the DNA molecules. Also shown is the geometrical setup for the measurement of the angle of the principal axis of the radius of gyration. (C-E) Confirmation of planar elongational deformation in the center region of the 2 μm device by tracking of λ-DNA molecules (C) Trajectories of the center of mass of each λ-DNA molecule illuminate the electric field streamlines in the device. (D) and (E) display the* x *and* y *locations (respectively) of each molecule with time. The solid lines are the average of the fitted slopes of the individual traces, yielding a strainrate of* $\dot{\varepsilon} = 1.2 \pm 0.1\,\mathrm{s}^{-1}$. *The relaxation time of λ-DNA in a 2 μm tall channel is* $\tau_{\mathrm{I}} = \tau_{\mathrm{II}} = 0.2\,\mathrm{s}$ *[40], yielding* $\mathrm{De}_{\mathrm{I}} = \mathrm{De}_{\mathrm{II}} = 0.24 < \mathrm{De}_{\mathrm{crit}}$.

Table 5.1: *Channel dimensions and T4 DNA relaxation times.*

h	τ_{I} (s)	τ_{II} (s)	$\mathrm{De_{II}}/\mathrm{De_{I}}$	l (μm)	w (μm)
2.0 μm	1.5	1.5	1	100	40
300 nm	2.7	5.4	2	50	40
150 nm	4.6	18.3	4.0	50	40

channel. The role of the hyperbolically shaped sidewall is easily observed as no disruption to the streamlines occurs even very near the walls. Panels D and E show the experimental determination of the strain rate as the slope of the position versus time plots on semi-log scales. The strain rate is indeed uniform in the intersection region of the channel, and experiments at different applied voltages confirmed that the strain rate is linear with applied electric field for all channel heights used (data not shown). The strain rate was calibrated against applied voltage prior to each experiment.

5.2.3 Relaxation Time Measurements

Measurement of the longest relaxation time occurred in the same channel used for the stretching experiments. A T4 DNA molecule was stretched to nearly full extension in a high field gradient at the stagnation point, the field was switched off, and the relaxation of the molecule was observed. Two distinct time constants were obtained for the two nanochannels, as expected [66]. In the 2 μm tall channel, T4 DNA is not sterically confined [66] and thus only one time constant exists. The relaxation time was fit using the equation:

$$\frac{\langle X_{\mathrm{ex}}^2\rangle - \langle X_{\mathrm{ex,eq}}^2\rangle}{L_c} = A\exp\left(\frac{-t}{\tau}\right) \tag{5.3}$$

where X_{ex} is the extension of the molecule in the stretched (x) direction, $X_{\mathrm{ex,eq}}$ is the equilibrium extension in the stretched direction (measured after more than 10 relaxation times after turning off the field), L_c is the contour length of the T4 DNA molecule (70 μm) and t is time. A and τ are fitted parameters. Fitting regions for the two time constants are the same as those described previously [66]. Relaxation times for T4 DNA measured here are summarized in Table 5.1.

5.2.4 T4 DNA Stretching Experiments

T4 DNA was used for the stretching experiments. A typical molecule was moved into the channel intersection and allowed to rest for typically 10 longest relaxation times τ_{II} for the nanochannels). The field was then switched on and the molecule observed for 6 minutes or at least 20 units of strain. The time constraint is to limit photo-bleaching of and photo-induced damage to the stained DNA molecules. The extension of the molecule in the x-direction (X_{ex}) was measured via a simple threshold. Steady-state averages were obtained by sampling individual traces at time intervals equal to the higher extension relaxation time τ_{I} after the molecule has experienced a strain of 10 (except for the case of $\mathrm{De_I} = 0.1$ in the 150 nm tall channel, a strain of 5 was used because 10 units of strain can not be attained under this very small applied strain rate, due to the observation time constraint). Ensemble averages were taken over at least 10 molecules (at the lowest strain rates) to more than 50 (at the highest strain rates).

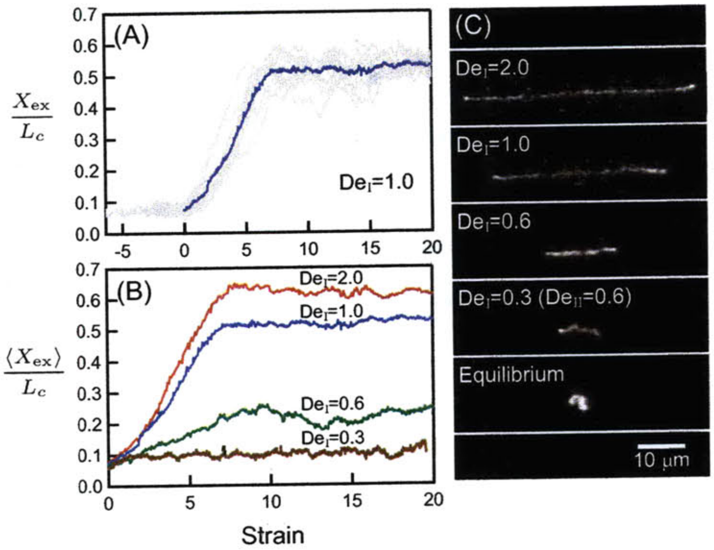

Fig. 5.3: *(A) Gray lines indicate individual traces of the fractional extension of each molecule versus strain applied (residence time in the field times the strain rate) for* $\mathrm{De_I} = 1$ *in a 300 nm tall channel. The bold line is the ensemble average extension with strain. (B) Ensemble average extension as a function of strain for selected* $\mathrm{De_I}$ *in the 300 nm tall device. (C) Snapshots of individual DNA images at steady state at the given* $\mathrm{De_I}$ *in the 300 nm tall device.*

5.3 Results and Discussion

Figure 5.3A shows the fractional extension (normalized by the contour length) with strain for individual molecules (gray lines) as well as their ensemble-average (bold line) for the 300 nm tall channel at $\mathrm{De_I} = 1$. Figure 5.3B shows the ensemble-average extension for four $\mathrm{De_I}$ in the 300 nm tall channel. It is clearly observed, even for low $\mathrm{De_I}$, that the molecules reach steady state after an applied strain on order 10. Thus, the trapping ability and residence times afforded by our device is sufficient for experimental observation of the steady state stretch at these deformation rates. The fact that steady state is reached after approximately 10 units of strain is interesting in its own right. This is the same order of magnitude as observed in studies of unconfined DNA [95], implying that while confinement may alter the level of stretch that can be attained at a given strain rate, it does not necessarily significantly increase the rate of stretching. More careful studies focusing on the stretching transients are needed to fully characterize these effects.

Figure 5.4 shows the steady state extension versus dimensional and non-dimensional measures of the strength of the deformation applied. Figure 5.4A shows very clearly that confinement does indeed aid DNA stretching. The stretch increases at a given strain rate with decreasing channel height, more than 7-fold between the 2 μm and 150 nm tall devices at a strain rate of $0.2\,\mathrm{s}^{-1}$. Importantly, at high extensions, the strain rate required to achieve a given extension can be decreased

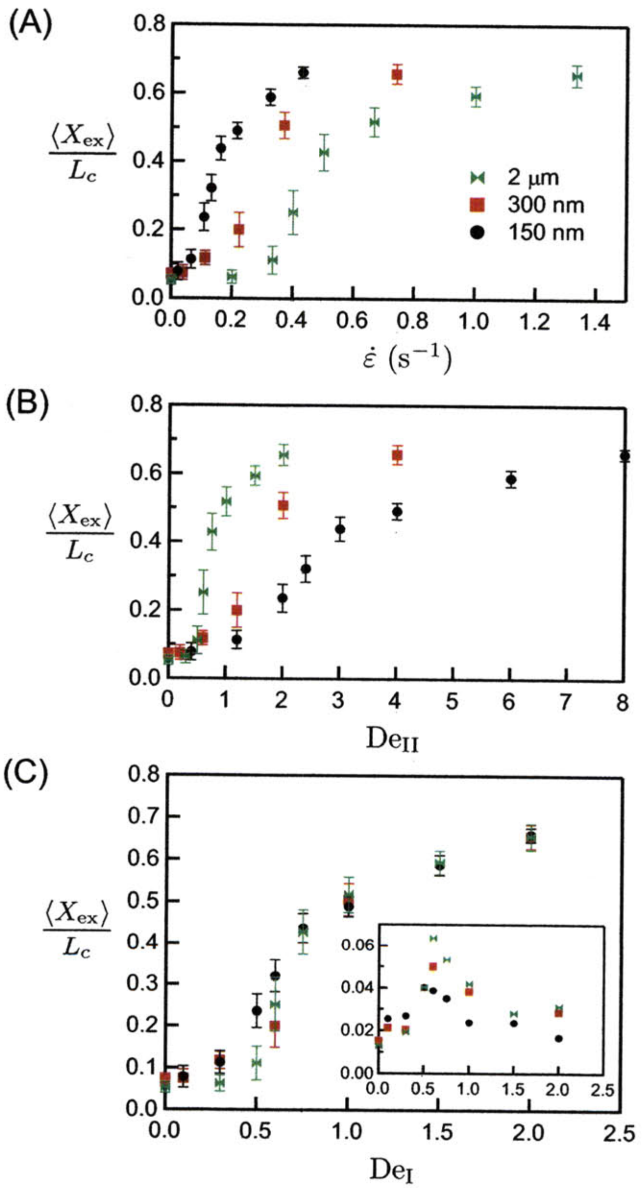

Fig. 5.4: *(A) Ensemble average steady state extension versus the dimensional strain rate for three channel heights. (B) Ensemble average steady-state extension versus* $\mathrm{De}_{\mathrm{II}}$*, the strain rate normalized by the low extension relaxation time. (C) Ensemble average steady-state extension versus* De_{I}*, the strain rate normalized by the higher extension relaxation time. Inset: Standard deviation* (σ/L_c) *of the steady-state stretch versus* De_{I}.

by more than 70% by exploiting confinement at these scales.

Figure 5.4B displays the same steady-state average extension versus $\mathrm{De}_{\mathrm{II}}$, the Deborah number using the low extension relaxation time (τ_{II}) to normalize the strain rate. The data do not collapse, and the location where the large increase in extension occurs does not agree with the predicted value of $\mathrm{De}_{\mathrm{crit}} = 0.5$. We conclude that the low extension relaxation time does not govern the coil-stretch transition in slit-like confinement. These results are in accord with our previous data [66] where the dynamics of relaxation are governed by the low extension relaxation time only very near equilibrium. We will return to this point below.

Figure 5.4C displays the steady-state average extension versus De_{I}, the Deborah number using the higher extension relaxation time to normalize the strain rate. It is clearly seen that this second slow timescale collapses the data quite well, and the drastic increase in extension occurs at approximately $\mathrm{De}_{\mathrm{I}} = 0.5$. The coil-stretch transition and stretch at higher extensions are better described by the second-longest relaxation time, a phenomenon unique to confinement in polymer physics. This data collapse is also seen in the inset of Figure 5.4 where the standard deviation of the average extension (σ/L_c) is plotted against De_{I}. Recent studies [67] have shown that the peak in this plot is a very good indicator of the location of the coil-stretch transition, and here we note that the peak is well-aligned on the abscissa. This alignment confirms that the higher extension relaxation time governs the large increase in the stretch of the molecule with applied strain rate. This finding provides a fundamental basis for the design of devices aiming to utilize slit-like confinement to attain highly extended DNA molecules. In these devices the higher extension relaxation time (τ_{I}) is the correct time scale that should be used for the prediction of the deformation rates required to achieve certain extensions because τ_{I} allows data collapse in the high extension regime.

However, at low De_{I}, Figure 5.4C does show some differences in steady state extension between the three channel heights. Specifically, the coil-stretch transition becomes more gradual in the more confined channels: we observe significant stretching at sub-critical $\mathrm{De}_{\mathrm{I}} < 0.5$, but where $\mathrm{De}_{\mathrm{II}} > 0.5$ (see Figure 5.3C). The more gradual transition may also account for the decreasing amplitude of the peak in the standard deviation with De_{I} plot (inset of Figure 5.4C) [67]. As expected, τ_{II} appears to affect stretching at low extensions, below the predicted relative crossover extensions [66] of $X^*_{\mathrm{ex}}/L_c = 0.17$ and 0.27 for the 300 and 150 nm tall channels respectively. Note that these predicted crossover extensions over-estimate the region governed by τ_{II} because they predict the center of a gradual transition [66]. Since the changes of steady state extensions involved here are small, it is helpful to examine other indicators of behavior departing from equilibrium dynamics.

Figure 5.5 shows the root-mean-square angle (θ_{RMS}) of the principal axis of the in-plane DNA radius of gyration (see Figure 5.2) as a function of strain. θ_{RMS} indicates the degree of orientation towards the axis of elongation (x-axis, $\theta_{\mathrm{RMS}} = 0°$) from the equilibrium average of $\theta_{\mathrm{RMS,eq}} = 52°$ (the horizontal solid line in Figure 5.5). The angle reaches steady state at relatively low strain and fluctuates about the average. Figure 5.5A shows ensemble average θ_{RMS} traces and the steady state averages for the three channel heights at similar sub-critical $\mathrm{De}_{\mathrm{II}}$ (≈ 0.3). The data collapse well and DNA molecules in three channel heights all show similar degree of orientation. All three traces show clear orientation from equilibrium, suggesting that θ_{RMS} can provide a strong measureable signal even very near equilibrium. Figure 5.5B shows the same quantities for the three channel heights at the same De_{I} ($= 0.3$). Data collapse is not as good and DNA molecules in the two nanochannels display significantly more orientation than those in the $2\,\mu$m tall channel. This observation is consistent with the fact that although De_{I} is sub-critical for all channel heights in Figure 5.5B, $\mathrm{De}_{\mathrm{II}}$ are above 0.5 for the two nanochannels (0.6 and 1.2 for the 300 and 150 nm tall

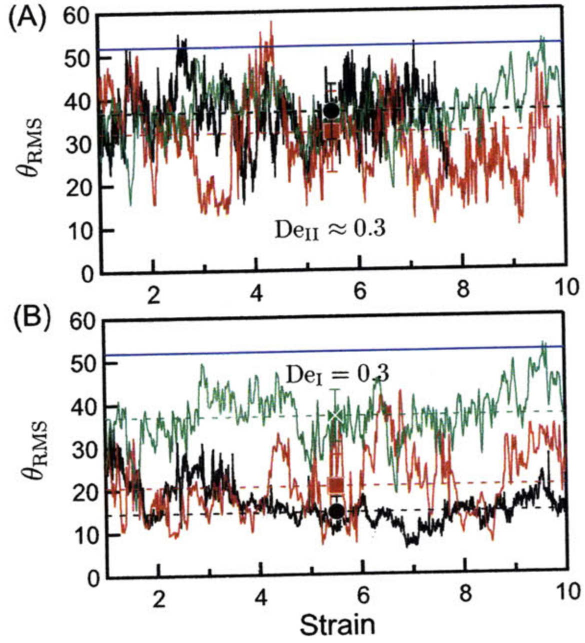

Fig. 5.5: *(A) Root-mean-square angle of the principal axis of the radius of gyration relative to the x-axis (θ_{RMS}, in degrees) versus strain for* $\mathrm{De}_{\mathrm{II}} \approx 0.25$ *for the three channel heights. Green, red, and black solid lines denote the 2 µm, 300 nm, and 150 nm tall channels, respectively; colored dashed lines and markers denote the steady state ensemble average RMS angle.* $\mathrm{De}_{\mathrm{II}} = 0.3$*, 0.2, and 0.4 for the 2 µm, 300 nm, and 150 nm channels respectively. The horizontal solid line denotes the equilibrium average ($\theta_{\mathrm{RMS,eq}} = 52\,°$). (B) θ_{RMS} for the three channel heights for* $\mathrm{De}_{\mathrm{I}} = 0.3$*, corresponding* $\mathrm{De}_{\mathrm{II}}$ *is 0.3, 0.6, and 1.2 for the 2 µm, 300 nm, and 150 nm channels respectively.*

channels, respectively). Thus, the low extension relaxation time (τ_{II}) more adequately describes behavior close to equilibrium and should be used to predict the first deviations from equilibrium.

5.4 Conclusions

We have designed a cross-slot device which yields large regions of homogeneous extensional deformation with limited spans amenable to the nanofluidic environment. Thus, we are able to exploit changes to the polymer dynamics induced by nanoslit confinement in order to facilitate dynamic manipulation of single molecules. We are able to easily select, trap, and stretch individual DNA molecules to steady state in this device. The confinement ensures the entire molecule remains in focus during the process, unlike other much taller microfludic stretching devices [26,27,28,31,118]. From the stretching results presented here, we conclude that confinement does aid the stretching of single DNA molecules by allowing the use of much smaller strain rates to achieve the same amount of extension. However, the time scale governing the large change in extension with applied strain rate is the higher extension relaxation time (τ_{I}). This finding is important since the prediction of this transition often forms the crux of design specifications for processes involving stretching or deforming DNA molecules, and naive application of unconfined theory to confined systems would significantly under-predict the strain rates required to deform DNA molecules. The low extension relaxation time (τ_{II}) governs the orientation and small deviations from equilibrium of the molecule. Our results are important for future studies of DNA dynamics in confinement, especially those concerned with the measurement of relaxation times or dynamic manipulation of extended DNA.

CHAPTER 6

Coil-stretch Transition of DNA in Slit-like Confinement

In this chapter we experimentally investigate the influence of slit-like confinement on the coil-stretch transition of single DNA molecules in a homogeneous planar elongational electric field. We observe a more gradual coil-stretch transition characterized by two distinct critical strain rates for DNA in confinement, different from the unconfined case where a single critical strain rate exists. We postulate that the change in the coil-stretch transition is due to a modified spring law in confinement. We develop a dumbbell model to extract an effective spring law by following the relaxation of an initially stretched DNA. We then use this spring law and kinetic theory modeling to predict the extension and fluctuations of DNA in planar elongational fields. The model predicts that a two-stage coil-stretch transition emerges in confinement, in accord with experimental observations. The Brownian dynamics simulations presented in this chapter were performed by Daniel W. Trahan.

6.1 Introduction

Advances in nanofabrication technologies have inspired interest in nanodevices that promise to provide fast and accurate methods for the analysis of genomic length DNA. Many such applications, including DNA separation [47, 113] and single molecule mapping [11, 16], rely on the ability to stretch individual DNA molecules from their initial coiled configurations into extended states.

Understanding how polymer deforms under confinement, is therefore of considerable importance for device design and optimization. Meanwhile, such knowledge can also aid to the development of fundamental polymer physics. The unique advantage of using nanoconfinement to stretch DNA lies in its capability to alter the shape and dynamics of polymers through both steric interactions and modulation of intramolecular hydrodynamic interactions (HI) [43, 44, 45, 46]. Recent studies have used tube-like confinement (representing channels with height $\approx$ width) to substantially change the equilibrium DNA conformation from a coil to a highly extended state [16, 25, 98, 109, 110, 111]. Alternatively, slit-like confinement (representing channels with height $\ll$ width) has been employed to facilitate stretching DNA far from equilibrium in elongational fields [119]. In this case the polymer deformation results from the competition between the stretching force imposed by the field gradients and the DNA elastic spring force that resists stretching [116]. In contrast to the equilibrium behavior of confined polymer that has gained much attention to date (see Ref. [115] for a review), the influence of confinement on this non-equilibrium process has only recently begun to be examined. Initial studies in this field [66, 119] have demonstrated a unique feature of DNA stretching in slit-like nanochannels: the steric interactions between DNA and the confining walls become weaker and eventually vanish as the molecule extends, suggesting that the stretching process may be conformation-dependent.

Several experimental studies have investigated the stretching of unconfined DNA in extensional hydrodynamic flows [26, 27, 28, 29, 67] and electric fields [31, 117]. A sudden increase in the steady-state extension of DNA was observed near a critical velocity (electric field) gradient or strain rate of $\dot{\varepsilon}_c$. The values of $\dot{\varepsilon}_c$ determined in these experiments agree well with the theoretical prediction of $\dot{\varepsilon}_c \approx 0.5/\tau$, where τ is the longest relaxation time of the polymer [94]. The abrupt coil-stretch transition is closely related to the shape of the spring force law [26]. For DNA in bulk, the force law is characterized by a linear force regime from equilibrium to ~30% relative extension and a highly nonlinear response at large extensions (See Figure 6.1B). For $\dot{\varepsilon} < \dot{\varepsilon}_c$, the stretching force exerted on the polymer is lower than the spring force and thus the conformation is weakly perturbed. As soon as the strain rate is increased above $\dot{\varepsilon}_c$, the stretching force exceeds the linear portion of the spring force, and the polymer stretches into a significantly extended state until its nonlinear elasticity limits any further extension. During this conformational transition, polymer molecules also exhibit slowed-down transient dynamics towards steady-state and an increased magnitude of extension fluctuations [67, 120, 121], similar to the critical phenomena observed in a thermodynamic phase transition. The essential physical reason for these unique behaviors is the existence of large number of configurations corresponding to vastly different extensions that are accessible close to the critical strain rate, at which the stretching force balances the entire linear region of the elastic spring force [67]. In potential flows, this configuration space can also be interpreted in terms of a conformational energy landscape [116] that becomes relatively flat near the coil-stretch transition. The aforementioned characteristics of the coil-stretch transition, i.e., the drastic deformation, the dynamic slowdown, and the significant conformation fluctuations, are enhanced by the extension-dependent hydrodynamic drag coefficient, a result of the dominant intramolecular HI for DNA in bulk [28, 29, 67, 116, 121]. The drag coefficient of the polymer directly impacts on the stretching force imposed by the field gradients. An extremely large increase in the drag coefficient as the polymer fully extends from the coiled state can lead to conformational hysteresis at the coil-stretch transition [28, 116].

Slit-like nanochannels offer a very powerful method to change the course of DNA deformation by impacting both the applied stretching force and the DNA spring force. The stretching force is

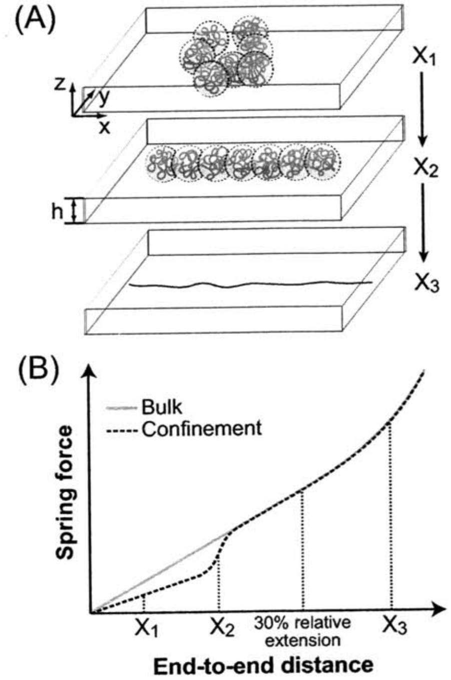
(A)
z
y
x
h
X1
X2
X3
(B)
Bulk
Confinement
Spring force
X1
X2
30% relative extension
X3
End-to-end distance

Fig. 6.1: *(A) Schematic of the DNA stretching process in slit-like nanochannels. (B) A schematic comparison of the effective spring force law for DNA in confinement and in bulk. The bulk spring force varies linearly with the end-to-end distance below ~30% relative extension. In confinement, DNA molecules near equilibrium are sterically confined and the corresponding spring force is reduced. Highly extended DNA is no longer confined and the spring force restores back to the bulk force law.*

affected through modulation of intromolecular HI: nanoslits with height smaller than the equilibrium size of DNA are capable of screening long range HI, leading to an increased drag coefficient of DNA and thus stronger stretching force [56, 65]. Meanwhile, since the increase in drag coefficient is more dramatic for coiled DNA than that for highly extended molecule, the overall extension dependence of the drag coefficient is significantly reduced. Modification of the DNA spring force relies on the steric interactions between DNA and the confining walls, which, however, are only important for DNA molecules at moderate extensions [66]. A highly extended DNA is not sterically confined in the nanochannels and the corresponding spring force stays unaffected (i.e., identical to the bulk spring force, see Figure 6.1). As the extension decreases, the lateral dimension of the DNA (z-dimension in Figure 6.1A) grows until it becomes equivalent to the channel height h. After this point, the conformation of the DNA is constrained by the steric confinement and the spring force is reduced. In nanochannels much taller than the persistence length of the DNA, this transition occurs within the bulk linear force regime (i.e., below 30% fractional extension) [119], and the spring force for confined DNA near equilibrium is still linear with extension but the spring constant is smaller [44, 57]. As a result, the spring force law of DNA in slit-like confinement contains two linear regimes: a confined linear force regime close to equilibrium and a truncated bulk linear force regime at larger extensions (see Figure 6.1B), which are connected by a transition region where the spring force gradually restores to the bulk force law as the DNA stretches. The relative widths of these regions depend upon the channel height h [66, 119]. The compound effect of the more uniform drag coefficient and the newly introduced conformation dependence in the spring force of DNA under confinement results in a very different stretching process. In the confined linear spring force regime, DNA molecules can be more easily deformed due to the increased drag coefficient and softened spring, pointing to the fact that confinement may allow a much earlier coil-stretch transition. As the DNA extends into the transition region, the spring stiffens and acts to limit the amount of extension. Once the DNA becomes non-sterically confined, stretching progresses as if the DNA were in bulk but with an increased drag coefficient. We have previously shown experimental evidence of this "bulk-like" deformation at large extensions and found that despite the fact that the spring force in this region does not differ from the bulk force law, the increased drag coefficient reduces the strain rate required to stretch DNA to a certain extension [119]. The purpose of this study is to investigate the coil-stretch transition that takes place at moderate extensions where the DNA spring force is affected by the steric confinement. The existence of two linear spring force regimes with distinct spring constants foreshadows that confinement will both quantitatively and qualitatively modify coil-stretch transition.

6.2 Experiments

6.2.1 Device Geometry

We electrophoretically stretched single DNA molecules in homogeneous extensional electric fields under varying degrees of confinement. In a planar homogeneous extensional electric field, the electrophoretic velocity of a point charge varies linearly with position:

$$v_x = \mu E_x = \dot{\varepsilon} x \tag{6.1}$$

$$v_y = \mu E_y = -\dot{\varepsilon} y \tag{6.2}$$

where v_x and v_y are the velocities in the x and y directions, respectively, E_x and E_y are the electric fields in the x and y directions, respectively, μ is the electrophoretic mobility, and the strain rate $\dot{\varepsilon}$ is a constant. This type of field kinematics was achieved by applying symmetric potentials to a cross-slot channel with the incorporation of hyperbolically curved sidewalls (see Figure 6.2A and B). Since the shape of the sidewalls matches exactly the streamlines in a planar homogeneous extensional field, there are no inhomogeneities to disrupt the linear electric field profile over the entire intersection region [79]. For the same planar geometry (x-y plane), the field lines do not depend on channel height so long as the height is uniform within a device. The channel has been recently used to study stretching of confined DNA at large extensions [119]. A unique feature of the channel is that it allows for extremely long residence time (t_{res}) of DNA in the extensional electric field so that any molecular individualism effects [26,27] can be overcome and the steady-state behaviors of DNA can be observed. The long residence time was achieved by applying independently controlled potentials to the side reservoirs and thus enabling sensitive adjustment of the stagnation point position via perturbations to the field (see Figure 6.2B). With this capability of stagnation point control, any DNA molecules of interest can be trapped at the stagnation point for very high accumulated strains ($\varepsilon = \dot{\varepsilon} t_{\text{res}}$).

6.2.2 Channel and DNA Preparation

Cross-slot channels with three different heights were used in this study. 2 μm tall microchannels were constructed in polydimethylsiloxane (PDMS, Sylgard 184, Dow Corning) using soft-lithography on a silicon master (SU8-2 photoresist). The PDMS channels were soaked in 0.5 × Tris-Boric acid-EDTA (TBE, Omnipure) buffer at 40 °C overnight to eliminate permeation driven flow through the PDMS [99], rinsed and dried briefly, and sealed to a glass cover-slide. Glass nanochannels with two different heights (h = 300 nm and 150 nm) were created by a photo-resist protected etch in buffered oxide etchant and thermally bonded to a glass cover slide as described previously [100]. The glass nanochannels were filled with filtered deionized water and rinsed via application of potentials at the fluid reservoirs before use. All channels were flushed with the experimental buffer prior to exposure to DNA molecules. The experimental buffer was 0.5 × TBE solution with 0.1% 10 kDa polyvinylpyrrolidone (PVP, Polysciences), and an oxygen scavenger system consisting of 4% (vol.) betamercaptoethanol (BME, Cabiochem), 12.5 mg/mL glucose (Mallinckrodt), 0.16 mg/mL glucose oxidase (Sigma), and 9.6 μg/mL catalase (Sigma). Channels were flushed with new buffer every two hours during experiments to ensure a constant ionic strength environment [58]. T4 DNA molecules (165.6 kbp, Nippon gene) and λ-DNA molecules (48.502 kbp, New England Biolabs) were stained (at a DNA concentration of 0.69 μg/mL) with YOYO-1 (Invitrogen) dye at a basepair to dye ratio of 4:1 and allowed to sit at least overnight. DNA samples were diluted 2 to 10-fold immediately before experiments to reach an optimal concentration for observation.

6.2.3 Electric Field Characterization

The electric field kinematics generated in the intersection region of all cross-slot devices were verified by tracking the center of mass of electrophoresing DNA under conditions in which they do not appreciably deform. λ-DNA (contour length $L_c \approx 21\,\mu$m) was used as the tracer since it is large enough to easily track, but small enough to not appreciably deform at the electric fields employed. Figure 6.3A shows the center of mass position of 257 λ-DNA molecules as they electrophorese through the 300 nm tall channel. The role of the hyperbolically shaped sidewall is easily observed

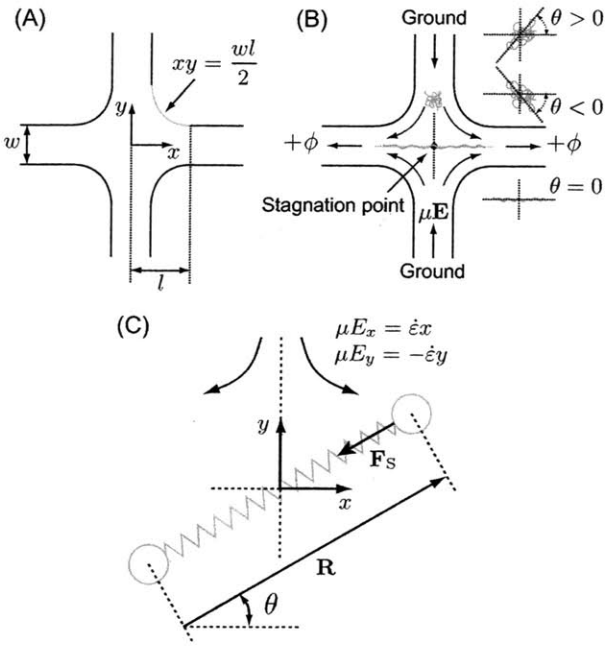
(A)
$xy = \frac{wl}{2}$
y
x
w
l
(B)
Ground
$\theta > 0$
$\theta < 0$
$+\phi$
$+\phi$
$\theta = 0$
Stagnation point
$\mu\mathbf{E}$
Ground
(C)
$\mu E_x = \dot{\varepsilon}x$
$\mu E_y = -\dot{\varepsilon}y$
y
$\mathbf{F}_S$
x
$\mathbf{R}$
θ

Fig. 6.2: *(A) Diagram of the cross-slot stretching device geometry. The geometrical parameters of the channels used in this study are summarized in Table 6.1. (B) Schematic of the motion and stretching of DNA molecules in the device. Independent applied voltages to the left and right arms of the channel allow adjustment of the location of the stagnation point and trapping of the DNA molecules. Also shown is the geometrical setup for the measurement of the angle of the principal axis of the radius of gyration (θ). (C) Setup of the Brownian dumbbell model in a planar homogeneous extensional electric field. The center of mass of the dumbbell is fixed at the stagnation point.*

Table 6.1: *Channel dimensions and T4 DNA relaxation times.*

h	l (μm)	w (μm)	τ_{I} (s)	τ_{II} (s)
2.0 μm	100	40	1.9	1.9
300 nm	50	40	3.0	6.4
150 nm	50	40	5.7	21.2

as no disruption to the streamlines occurs even very near the walls. Figure 6.3B and C show the experimental determination of the strain rate as the slope of the position versus time plots on semi-log scales. The strain rate is indeed uniform in the intersection region of the channel, and experiments at different applied voltages confirmed that the strain rate is linear with applied electric field for all channel heights used (data not shown).

6.2.4 DNA Stretching Experiments

T4 DNA was used for the stretching experiments. A typical molecule was electrophoretically driven into the channel intersection, trapped at the stagnation point, and observed for 9 minutes or at least 20 units of strain at desired strain rate. The time constraint is to limit photo-bleaching of and photo-induced damage to the stained DNA molecules. We used an inverted Zeis Axiovert 200 microscope with a 63× 1.4NA oil-immersed objective to observe single DNA molecules. Images were captured using a Hamamatsu EB-CCD camera (model 7190-21) and NIH image software. The maximum extension of the DNA was measured from a simple threshold, and the angle of the principal axis of the DNA radius of gyration tensor with respect to the axis of elongation was extracted following procedures described in Ref. [57]. For each strain rate studied, images of 25–35 DNA molecules were taken. Steady-state DNA configurations were sampled from each individual traces at time intervals equal to the higher-extension relaxation time τ_{I} after the molecule has experienced a strain of 10 (except for the case of $\mathrm{De}_{\mathrm{I}} = 0.1$, a strain of 5 was used because 10 units of strain can not be attained under this very small applied strain rate due to the limited observation time). Ensemble averages and standard deviations were calculated with the samples collected from all traces.

6.3 Dumbbell Model

6.3.1 Model Description

In addition to experiments, we construct a Brownian dumbbell model to obtain a qualitative description of DNA stretching in slit-like confinement. We model T4 DNA as two charged beads connected by an elastic spring. The dumbbell is placed in a homogeneous planar extensional electric field and its center of mass is fixed at the stagnation point (see Figure 6.2C). According to the theorem of electrohydrodynamic equivalence proposed by Long et al. [84], the electrophoretic stretching force $\mathbf{F}_{\mathrm{E}}$ on each bead equals to the drag force exerted on the bead by a hydrodynamic flow in which the flow velocity is the same with the bead electrophoretic velocity in the electric field: $\mathbf{F}_{\mathrm{E}} = \zeta\left(\mu\mathbf{E} - \mathbf{v}_{\mathrm{bead}}\right)$, where ζ, μ, and $\mathbf{v}_{\mathrm{bead}}$ are the bead drag coefficient, bead electrophoretic mobility, and instantaneous velocity of the bead, respectively. The probability density function of

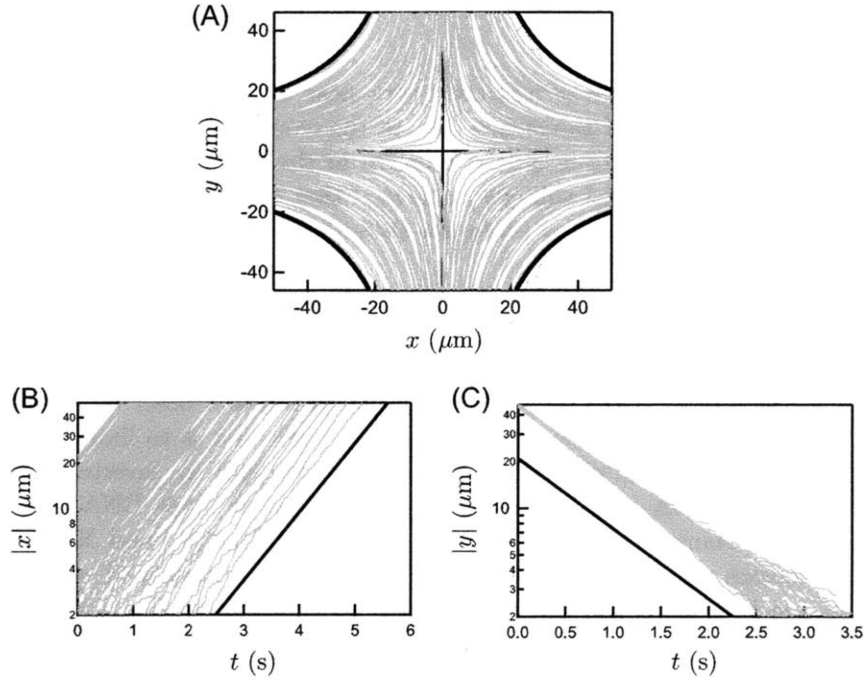

Fig. 6.3: *Confirmation of planar elongational deformation in the center region of the 300 nm device by tracking* λ*-DNA molecules. (A) Trajectories of the center of mass of each* λ*-DNA molecule illuminate the electric field streamlines in the device. The bold black lines indicate the channel walls. (B) and (C) display the absolute values of the* x *and* y *locations (respectively) of each molecule with time. The solid black lines are the average of the fitted slopes of individual traces, yielding a strain rate of* $\dot{\varepsilon} = 1.04 \pm 0.07\,\mathrm{s}^{-1}$*. The low-extension relaxation time and the higher-extension relaxation time of* λ*-DNA in the 300 nm channel are estimated to be* $\tau_{\mathrm{II}} \approx 0.32\,s$ *and* $\tau_{\mathrm{I}} \approx 0.20\,s$ *[57, 66], giving* $\mathrm{De}_{\mathrm{II}} \approx 0.33$ *and* $\mathrm{De}_{\mathrm{I}} \approx 0.21$.

the dumbbell end-to-end vector, $\psi(\mathbf{R}, t)$, satisfies the diffusion equation [92]:

$$\frac{\partial \psi}{\partial t} = -\frac{\partial}{\partial \mathbf{R}} \cdot \psi \left(\nabla \mu \mathbf{E} \cdot \mathbf{R} - \frac{2 k_{\mathrm{B}} T}{\zeta} \frac{\partial}{\partial \mathbf{R}} \ln \psi + \frac{2}{\zeta} \mathbf{F}_{\mathrm{S}} \right) \tag{6.3}$$

where $\mathbf{R}$ is the dumbbell end-to-end vector and $\mathbf{F}_{\mathrm{S}}$ is the elastic spring force (see Figure 6.2C). We seek steady-state solutions for ψ which allow us to predict the steady-state properties of the dumbbell such as the average end-to-end distance and the degree of extension fluctuations, as will be described later. Previous works [28, 29, 116, 121] have employed similar models to study the coil-stretch transition of polymers in bulk in which case the drag coefficient varies with extension due to HI. Here the dumbbell model represents DNA molecule in thin channels where long range HI is screened, and we assume the drag coefficient of the dumbbell to be constant. In addition, we neglect the dumbbell extension in the channel height dimension so that the dumbbell end-to-end distance ($R = |\mathbf{R}|$) satisfies $R^2 \approx R_x^2 + R_y^2$, where R_x and R_y are the dumbbell end-to-end distances in the x and y directions, respectively. For a planar homogeneous extensional electric field, the first term in parentheses on the right-hand side of Equation 6.3 can be expressed as $\nabla \mu \mathbf{E} \cdot \mathbf{R} = \frac{\partial}{\partial \mathbf{R}}[\frac{1}{2} \dot{\varepsilon} R^2 \cos(2\theta)]$, where θ is the angle of the dumbbell principal axis with respect to the axis of elongation (see Figure 6.2C, $-\pi/2 < \theta < \pi/2$). The analytical solution to Equation 6.3, for dumbbells at steady-state such that $\partial \psi / \partial t = 0$, can now be found [92]:

$$\psi(\mathbf{R}) = K \exp \left\{ \frac{1}{k_{\mathrm{B}} T} \left[\frac{1}{4} \zeta \dot{\varepsilon} R^2 \cos(2\theta) + \int_{\mathbf{R}} \mathbf{F}_{\mathrm{S}}(\mathbf{R}) \cdot d\mathbf{R} \right] \right\} \tag{6.4}$$

where K is the normalization constant which satisfies the condition $\int_{\mathbf{R}} \psi d\mathbf{R} = 1$.

6.3.2 Spring Force Law in Confinement

Information regarding the spring force law is required in order to compute the probability distribution function ψ using Equation 6.4. Since confinement can either significantly reduce the spring force or have no impact on the spring force depending on the extension of the molecule, it is important that the spring force used in the dumbbell model accounts for these extension-dependent confining effects. The wormlike chain force law derived by Marko and Siggia [76] has usually been used to represent the spring force of DNA in bulk. The wormlike chain spring force is given by $\mathbf{F}_{\mathrm{S,bulk}} = -H_{\mathrm{bulk}} \mathbf{R} f(R/L_c)$ where L_c is the contour length of the spring and H_{bulk} is the unconfined Hookean spring constant which can be expressed in terms of L_c and the Kuhn step size b as $H_{\mathrm{bulk}} = 3 k_{\mathrm{B}} T / L_c b$. The dimensionless function $f(R/L_c)$ in the force law describes the nonlinear response of the spring

$$f\left(\frac{R}{L_c}\right) = \frac{L_c}{6R} \left[\left(1 - \frac{R}{L_c}\right)^{-2} + \frac{4R}{L_c} - 1 \right] \tag{6.5}$$

At low extensions ($R/L_c \ll 1$) f is approximately unity and the spring force becomes linear with extension: $\mathbf{F}_{\mathrm{S,bulk}} \approx -H_{\mathrm{bulk}} \mathbf{R}$. Considering that the DNA spring force is affected by the steric confinement only at these small extensions where the nonlinearity represented by f is not important, we assume that confinement primarily contributes to modifying the spring constant. Hence, we adapt the bulk wormlike chain spring force law to the confined case and use an extension-dependent spring constant H to represent the confinement-induced effects: $\mathbf{F}_{\mathrm{S}} = -H(R) \mathbf{R} f(R/L_c)$.

At large extensions where DNA is not sterically confined, the spring force remains identical to the bulk force law and $H = H_{\mathrm{bulk}}$. At extensions very close to equilibrium, confined DNA exhibits linear spring force law with a reduced spring constant which we denote as the low-extension spring constant H_{low} ($H_{\mathrm{low}} < H_{\mathrm{bulk}}$). A transition region exists where the spring constant H gradually changes from H_{low} to H_{bulk} with increasing extension.

We seek the value of the spring constant H as a function of the dumbbell extension for all three channels used in this study. The $2\,\mu$m tall channel does not significantly confine T4 DNA [119] so that $H = H_{\mathrm{bulk}}$ at all extensions. In the 300 nm and 150 nm tall channels, DNA is confined near equilibrium and H is extension-dependent. In order to obtain the functional form of H with respect to the dumbbell extension, we consider the fact that any modifications of the spring constant directly manifest themselves in the DNA relaxation dynamics, which can be measured experimentally by stretching T4 DNA molecules to nearly full extension using a high electric field gradient, turning off the field, and monitoring the evolution of the mean-square extension of these molecules [119]. Consequently, we can use the experimental relaxation data to infer the spring constant in confinement. We first examine the effects of an extension-dependent spring constant on the relaxation of an initially stretched dumbbell. The equation of change for the mean-square dumbbell end-to-end distance $\langle R^2 \rangle$ can be derived from the diffusion equation (Equation 6.3) by setting no electric field, multiplying the equation by R^2, and integrating over all the configuration space [92]:

$$\frac{d}{dt}\langle R^2 \rangle = \frac{8k_{\mathrm{B}}T}{\zeta} + \frac{4}{\zeta}\langle \mathbf{F}_{\mathrm{S}} \cdot \mathbf{R} \rangle \tag{6.6}$$

We examine the relaxation behavior at extensions where H is affected by confinement. In both the 300 nm and 150 nm tall channels, the deviation of H from H_{bulk} occurs within the bulk linear force regime [119] so we employ the simplified spring force law $\mathbf{F}_{\mathrm{S}} = -H\mathbf{R}$ to Equation 6.6. We further assume fluctuation of the dumbbell end-to-end distance is small during the relaxation process such that $\langle HR^2 \rangle \approx H\langle R^2 \rangle$, giving

$$\frac{d}{dt}\langle R^2 \rangle = \frac{8k_{\mathrm{B}}T}{\zeta} - \frac{4H}{\zeta}\langle R^2 \rangle \tag{6.7}$$

When the dumbbell has reached equilibrium such that $H = H_{\mathrm{low}}$ and $d\langle R^2 \rangle_{\mathrm{eq}}/dt = 0$, the mean-square equilibrium end-to-end distance of the dumbbell can be solved from Equation 6.7: $\langle R^2 \rangle_{\mathrm{eq}} = 2k_{\mathrm{B}}T/H_{\mathrm{low}}$. Substituting this result into Equation 6.7, and defining a dimensionless dumbbell end-to-end distance $X = R/L_c$ and a scaled relaxation function $G = \langle X^2 \rangle - \langle X_{\mathrm{eq}}^2 \rangle$, we arrive at

$$\frac{dG}{dt} = -\frac{4H}{\zeta}G - \frac{4(H - H_{\mathrm{low}})}{\zeta}\langle X_{\mathrm{eq}}^2 \rangle \tag{6.8}$$

At high extensions where $X \gg X_{\mathrm{eq}}$ and $H = H_{\mathrm{bulk}}$, the second term on the right-hand side of Equation 6.8 can be neglected and the relaxation of G follows a single exponential decay $dG/dt = -G/\tau_{\mathrm{I}}$, where τ_{I} is the higher-extension relaxation time given by $\tau_{\mathrm{I}} = \zeta/4H_{\mathrm{bulk}}$. Similarly, for molecules close to equilibrium, $H = H_{\mathrm{low}}$, the second term on the right-hand side of Equation 6.8 vanishes and the decay of G is also exponential with a single time constant $\tau_{\mathrm{II}} = \zeta/4H_{\mathrm{low}}$ which we term as the low-extension relaxation time. The prediction of two distinct relaxation time constants by Equation 6.8 is in accord with recent experimental results of DNA relaxation times in confinement [66, 119].

Equation 6.8 can be rearranged to give

$$\frac{4H}{\zeta} = -\frac{1}{\langle X^2 \rangle}\frac{dG}{dt} + \frac{1}{\tau_{\mathrm{II}}}\frac{\langle X^2_{\mathrm{eq}} \rangle}{\langle X^2 \rangle} \tag{6.9}$$

Multiplying Equation 6.9 by τ_{I} and considering the bead drag coefficient ζ is assumed to be a constant for a given channel height, we obtain

$$\frac{H}{H_{\mathrm{bulk}}} = -\frac{\tau_{\mathrm{I}}}{\langle X^2 \rangle}\frac{dG}{dt} + \frac{\tau_{\mathrm{I}}}{\tau_{\mathrm{II}}}\frac{\langle X^2_{\mathrm{eq}} \rangle}{\langle X^2 \rangle} \tag{6.10}$$

Equation 6.10 allows us to calculate the spring constant from the relaxation data measured in experiments. We first located on experimental data (see Figure 6.4A and B) the two regions where G decays as a single exponential function and extracted the corresponding time constants τ_{I} and τ_{II}, following procedures described previously [66]. Results of the relaxation times for all three channels are summarized in Table 6.1 (see Appendix A.1 for a comparison between the relaxation times of T4 DNA measured here and these reported in chapter 5 for the same channel heights). The low-extension spring constant H_{low} is given by $H_{\mathrm{low}}/H_{\mathrm{bulk}} = \tau_{\mathrm{I}}/\tau_{\mathrm{II}}$. We next evaluated the first-order time derivative of the relaxation function and finally used Equation 6.10 to calculate the spring constant in the transition region where H varies with extension. As a result, the above approach of relating the dumbbell model relaxation to experimental relaxation data directly gives the value of H_{low}, and more importantly, the quantitative extension-dependence of the spring constant in terms of a smooth transition region.

Figure 6.4C and D show the extracted spring constant (normalized by H_{bulk}) as a function of the dumbbell end-to-end extension X for all three channels and the resulting spring force laws, respectively. It is clearly seen that the nanochannels change both the magnitude and the functional form of the spring force within the bulk linear force regime ($0 \leq X < 0.3$). At small extensions, we observe a second linear force regime corresponding to sterically confined DNA with a reduced spring constant H_{low}. This confined linear regime is connected to a truncated bulk linear force regime present at larger extensions through a rather wide transition region where the spring force increases nonlinearly with X towards the bulk force law. The nonlinearity of the spring in the transition region primarily results from the gradual increase of the spring constant from H_{low} to H_{bulk}. A decrease in channel height not only lowers the value of H_{low}, but also broadens both the confined linear force regime and the transition region. Consequently, the steric confining effects hold for a larger range of extensions (i.e., H restores to H_{bulk} at a larger extension) in the more confined channel, in agreement with previous scaling analysis [66]. In the 150 nm tall channel, the extension at which transition region terminates has been pushed up very close to $X = 0.3$. We expect that with further decrease in channel height, the transition region will eventually extend into the nonlinear regime, and the confined linear force regime will become the only linear region in the spring force law. We note that the spring force used in the dumbbell model represents the global effective spring force of a real DNA chain, which is the compound effect of the polymer's intrinsic entropic elasticity and the repulsive interactions among monomers (i.e., intramolecular excluded volume forces). The intrinsic spring constant (i.e., neglecting excluded volume effect) of a completely 2D chain is 2/3 that of a 3D bulk chain [68]. However, we observe that the effective spring force law can decrease by more than 50% compared to the bulk value. The excluded volume effect, therefore, should be playing an important role.

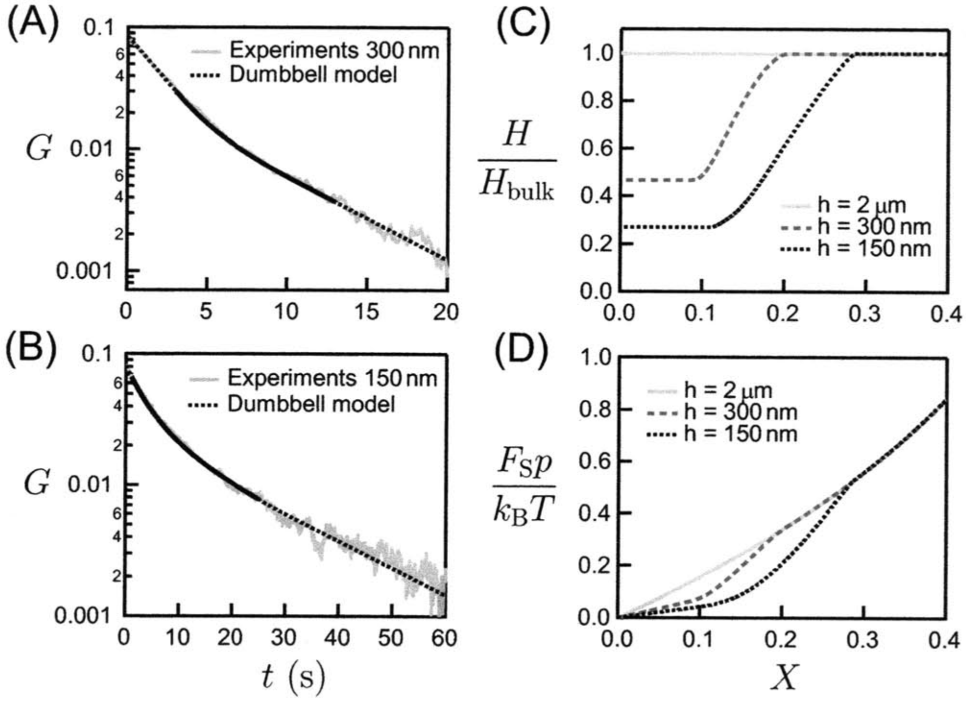

Fig. 6.4: *(A-B) Experimental relaxation data and relaxation of the dumbbell model calculated using Equation 6.8 with the extracted spring constant for the 300 nm tall channel (A) and the 150 nm tall channel (B). The two regions where* H *is a constant are indicated with dotted lines and the transition region where* H *varies with extension is indicated with the black solid line in the dumbbell relaxation curve. (C) The ratio* H/H_{bulk} *as a function of the dimensionless dumbbell end-to-end distance* X *extracted from experimental relaxation data for the* $2\,\mu m$*, 300 nm, and 150 nm tall channels. (D) The corresponding dimensionless dumbbell spring force* $F_S p/k_B T$ *as a function of* X *for the three channels,* p *is the persistence length of the DNA.*

Now we have all the information needed to compute the dumbbell configuration probability density function ψ. We rewrite Equation 6.4 in terms of dimensionless parameters and finally arrive at the equation that is used to calculate ψ:

$$\psi(X, \theta) = K \exp\left\{ -3N\left(\int_0^X \frac{H}{H_{\mathrm{bulk}}} x f(x) dx - \mathrm{De_I} X^2 \cos(2\theta) \right) \right\} \tag{6.11}$$

where N is the number of Kuhn steps in the spring $N = L_c/b$, and the dimensionless group $\mathrm{De_I}$ is the Deborah number defined using the the higher-extension relaxation time $\mathrm{De_I} = \dot{\varepsilon}\tau_{\mathrm{I}}$.

6.3.3 Predicting Experimental Observables

The probability density function ψ can be used to predict the steady-state properties of the dumbbell for given values of Deborah number $\mathrm{De_I}$. We focus on three important properties that characterize the coil-stretch transition: the average extension, the degree of extension fluctuations, and the molecular orientation in the extensional electric field. However, the dumbbell model is used to represent the end-to-end vector of a real DNA chain which is not experimentally observable. Instead, the maximum extension R_{max} of the DNA was measured in experiments. We use X_{max} to denote the fractional maximum extension of the DNA: $X_{\mathrm{max}} = R_{\mathrm{max}}/L_c$. At large $\mathrm{De_I}$ where DNA molecules are highly extended, the maximum extension and the end-to-end distance are almost identical and share similar distributions. At low $\mathrm{De_I}$ where DNA molecules do not significantly deviate from equilibrium, the distributions of X_{max} can be quite different from the distribution of X. Specifically, we expect the end-to-end distance X to hold a lower average value and exhibit more fluctuations. In order to predict the behavior of the maximum extension, we constructed a special probability distribution function, $P(X_{\mathrm{max}}|X)$, defined as the probability distribution of the maximum extension when the end-to-end distance of the molecule is fixed at a certain value. $P(X_{\mathrm{max}}|X)$ was determined using Brownian dynamics simulations of a multi bead-spring model (see Appendix A.2 for details). This function allows us to map the dumbbell model prediction for X to the distribution of the maximum extension, $P(X_{\mathrm{max}})$:

$$P(X_{\mathrm{max}}) = \int_0^1 P(X_{\mathrm{max}}|X) dX \int_{-\pi/2}^{\pi/2} \psi(X,\theta) X d\theta \tag{6.12}$$

The average fractional maximum extension can now be computed using

$$\langle X_{\mathrm{max}} \rangle = \int_0^1 X_{\mathrm{max}} P(X_{\mathrm{max}}) dX_{\mathrm{max}} \tag{6.13}$$

We calculated the standard deviation (σ) of X_{max} to indicate the magnitude of extension fluctuations.

$$\sigma = \sqrt{\int_0^1 \left(X_{\mathrm{max}} - \langle X_{\mathrm{max}} \rangle\right)^2 P(X_{\mathrm{max}}) dX_{\mathrm{max}}} \tag{6.14}$$

The orientation of the DNA in the stretching electric field has been experimentally examined by measuring the the root-mean-square angle (θ_{RMS}, see Figure 6.2B) of the principal axis of the DNA radius of gyration [119]. We thus calculated the same quantity for the dumbbell model:

$$\theta_{\mathrm{RMS}} = \sqrt{\int_0^1 \int_{-\pi/2}^{\pi/2} \theta^2 \psi(X,\theta) X dX d\theta} \tag{6.15}$$

In the T4 DNA relaxation experiments described earlier, we also only measured the maximum extension of DNA. We transformed the measured mean-square maximum extension $\langle X_{\mathrm{max}}^2 \rangle$ into the square end-to-end distance X^2 so that Equation 6.10 can be applied to calculate H. With the function $P(X_{\mathrm{max}}|X)$, the mean-square maximum extension corresponding to a certain end-to-end distance X can be determined: $\langle X_{\mathrm{max}}^2 \rangle = \int_0^1 X_{\mathrm{max}}^2 P(X_{\mathrm{max}}|X) dX_{\mathrm{max}}$. The transformation was performed by simply seeking backwards for the square end-to-end distance X^2 at a given $\langle X_{\mathrm{max}}^2 \rangle$.

6.4 Results and Discussion

6.4.1 Steady-state Extension

Figure 6.5 shows both the experimental results and dumbbell model predictions for the steady-state properties of T4 DNA molecules (contour length $L_c \approx 75\,\mu\mathrm{m}$). All quantities are plotted against $\mathrm{De_I}$, the Deborah number using the higher-extension relaxation time (τ_{I}) to normalize the strain rate. Figure 6.5A presents the average maximum fractional extensions of T4 DNA for the three channels with different heights. The experimental data collapse at large $\mathrm{De_I}$, confirming that τ_{I} is the correct time scale that governs DNA stretching in confinement at large extensions [119]. At small values of $\mathrm{De_I}$, DNA molecules in the nanochannels clearly exhibit distinct deformation process comparing with molecules in the $2\,\mu\mathrm{m}$ tall channel which does not significantly confine T4 DNA. While a rather abrupt increase in extension is observed near $\mathrm{De_I} = 0.5$ in the $2\,\mu\mathrm{m}$ tall channel, the coil-stretch transition becomes more gradual in confinement: the onset of DNA stretching occurs much earlier and the sharpness of the transition reduces with decreasing channel height. The dumbbell model qualitatively predicts the stretching of DNA in confinement. Specifically, the predicted coil-stretch transitions agree almost quantitatively with experimental data at low $\mathrm{De_I}$, and the extension curves corresponding to different channel heights collapse at high $\mathrm{De_I}$. The model overpredicts DNA extension at large stretch, possibly due to the fact that the dumbbell model overestimates the stretching force by representing a continuous polymer with two beads positioned at the polymer's termini, which are subject to stronger field strengths than a majority of the polymer in between.

6.4.2 Extension Fluctuations

A unique feature accompanying the coil-stretch transition is the greatly enhanced conformation fluctuations near the critical strain rate [67]. We probe the steady-state extension fluctuations of T4 DNA by measuring the standard deviation (σ) of the fractional maximum extension. Results of σ as a function of $\mathrm{De_I}$ are displayed in Figure 6.5B. A single peak is clearly observed in the experimental standard deviation plot for DNA in the $2\,\mu\mathrm{m}$ tall channel (see inset of Figure 6.5B). The peak occurs at $\mathrm{De_I} \approx 0.6$, in good agreement with that reported in a similar study for T4 DNA in bulk hydrodynamic elongational flow performed by Gerashchenko and Steinberg [67]. The magnitude of the peak measured in their study, however, is about 1.7-fold larger than that observed here for the same DNA in the $2\,\mu\mathrm{m}$ tall channel. We believe that a probable reason for this disparity

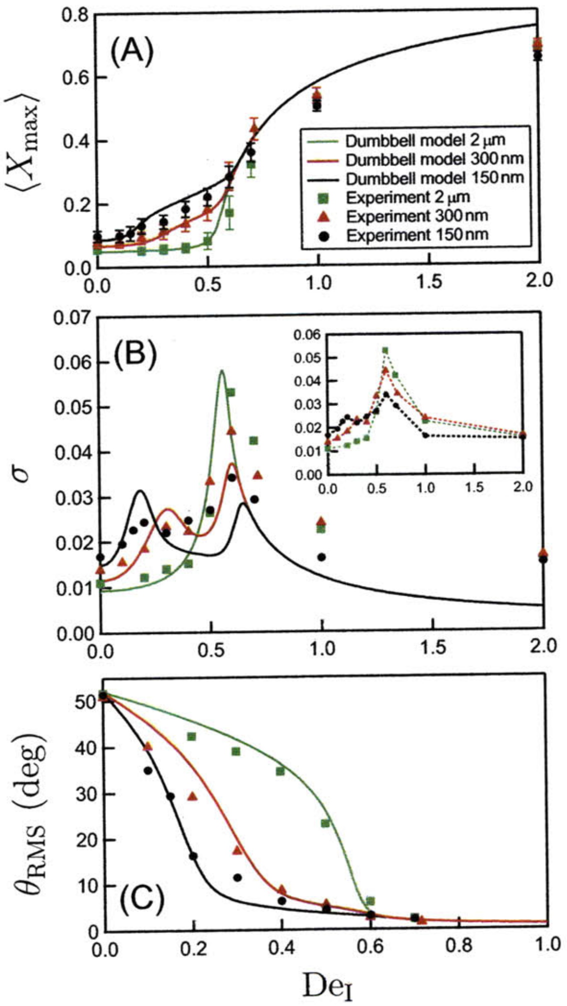

Fig. 6.5: *Experimental results and the dumbbell model predictions of the steady-state DNA behaviors. (A) The ensemble average steady-state maximum extension. (B) The standard deviation of the maximum extension which is a direct indication of the degree of extensional fluctuations, inset shows just the experimental standard deviation data for better clarity. (C) The root-mean-square angle of the principal axis of the molecule relative to the axis of elongation* (θ_{RMS}*, in degrees). All quantities are plotted against* $\mathrm{De_I}$.

is the much stronger extension-dependence of the drag coefficient of DNA in bulk due to dominant intramolecular HI (see Appendix A.3 for details). The location of the peak in σ for the $2\,\mu$m tall channel also corresponds well to where the drastic increase in extension is seen in Figure 6.5A. In fact, the maxima of the standard deviation provide a quantitative criterion for the determination of the critical strain rates in the coil-stretch transition [67], which, for the confined case, can be difficult to identify from the more gradual increase in extension.

The standard deviation data for DNA in the nanochannels show dramatically different characteristics. The peak at $\mathrm{De_I} \approx 0.6$ still exists but has a lower amplitude in the more confined channel. More importantly, we observe increased fluctuations at equilibrium (i.e., $\mathrm{De_I} = 0$), and the emergence of a second small peak at lower values of $\mathrm{De_I}$. As the channel height decreases, the value of this local maximum increases and its location moves towards smaller $\mathrm{De_I}$ (peak occurs at $\mathrm{De_I} \approx 0.3$ in the 300 nm tall channel and $\mathrm{De_I} \approx 0.2$ in the 150 nm tall channel). The existence of a second peak suggests that the coil-stretch transition in these nanochannels is characterized by two critical strain rates, a phenomenon unique to confinement in polymer rheology. The dumbbell model confirms the shift from a single critical strain rate in the microchannel to two critical strain rates in confinement. The predicted values of the critical $\mathrm{De_I}$ corresponding to the local maxima in σ match experiments well. Effects of the channel heights on the magnitude of these peaks and the equilibrium fluctuations are also qualitatively captured in the model. However, the dumbbell model overpredicts the magnitude of the peak near equilibrium and underpredicts that at the larger $\mathrm{De_I}$. Considering that the dumbbell model is a very simplistic description of a real DNA molecule, we would expect some moderate quantitative differences.

6.4.3 Molecular Orientation in the Extensional Electric Field

Figure 6.5C shows the root-mean-square angle (θ_{RMS}) of the principal axis of the in-plane DNA radius of gyration versus $\mathrm{De_I}$. θ_{RMS} indicates the degree of alignment towards the axis of elongation (x-axis) from the equilibrium average of $\theta_{\mathrm{RMS,eq}} = 52°$. Highly extended molecules align completely with the stretching electric field and give $\theta_{\mathrm{RMS,eq}} = 0°$ (see Figure 6.2B). It is clearly seen that DNA molecules start to orient towards the x-axis at very low values of $\mathrm{De_I}$ and yield strong measurable response of θ_{RMS}. Both the experimental data and the dumbbell model predictions show dramatically faster alignment of DNA molecules with the stretching electric field in the nanochannels. In all three channels, the molecules have already become fairly aligned with the stretching field at the Deborah number where significant stretching occurs or the first peak in the standard deviation emerges, indicating that this orientational response characterizes the behaviors departing from equilibrium dynamics prior to coil-stretch transition [119]. The molecule must first align with the field in order to be deformed, and the faster molecular orientation in the nanochannels is thus in accord with the earlier onset of stretching observed in Figure 6.5A.

6.4.4 Force Balance and Effective Conformational Energy

Both the experiments and theory show that the coil-stretch process is qualitatively different in confinement and the existence of two critical Deborah numbers. Further insight can be gained by revisiting the dumbbell model and considering both a force balance and effective conformational energy landscape. The conformation of a polymer in an elongational field is a competition between the spring force and the stretching force (electric field). The counterbalance between these two forces can be further related to an effective conformational energy landscape, which is very useful

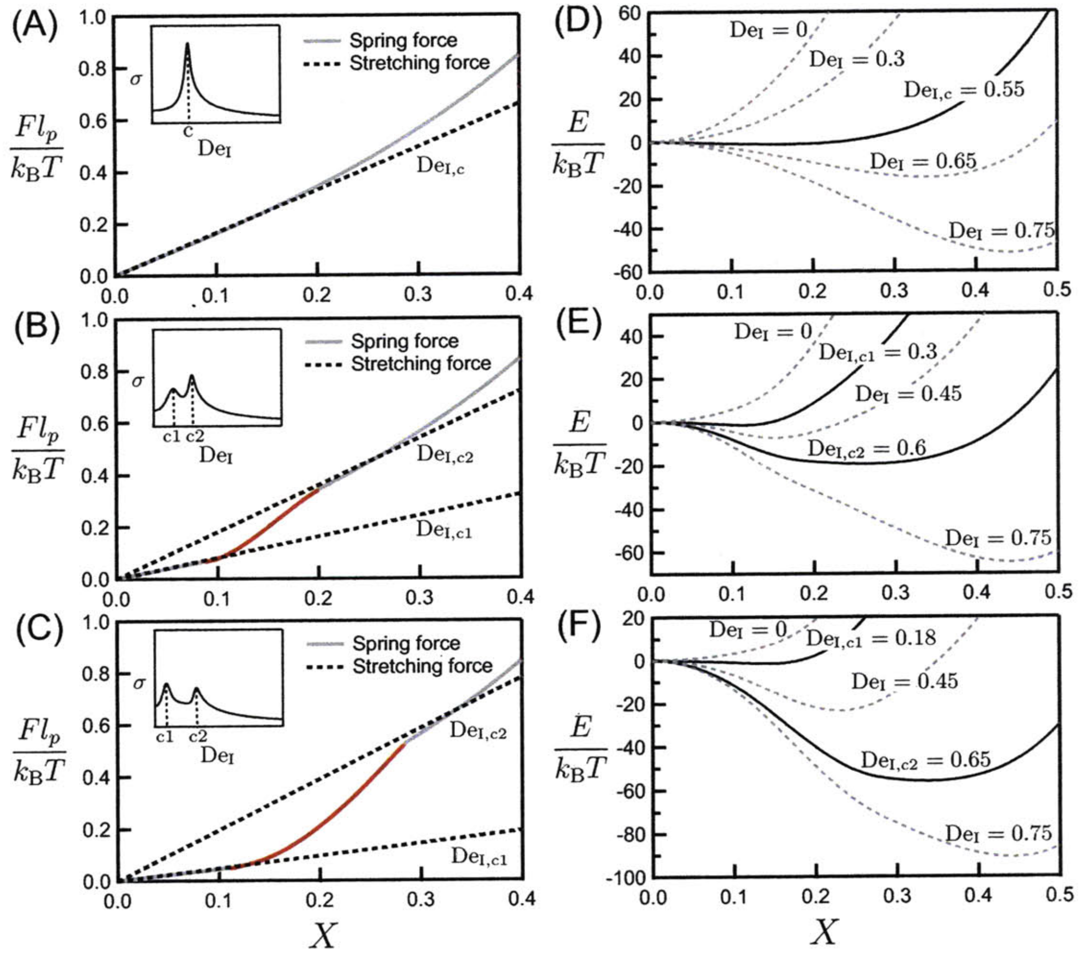

Fig. 6.6: *(A–C) Comparison between the stretching force exerted on a dumbbell with* $\theta = 0$ *at the critical* $\mathrm{De_I}$ *and the dumbbell spring force, for the* $2\,\mu m$ *tall channel (A), the 300 nm tall channel (B), and the 150 nm tall channel (C). Both forces are nondimensionalized with* k_BT/p. *The red lines in (B) and (C) indicate the transition regions of the spring force where the spring constant increases with* X. *Insets show the dumbbell model prediction of the standard deviation* σ *versus* $\mathrm{De_I}$ *for corresponding channel heights. The critical Deborah number is determined by seeking local maxima of* σ *for each channel. A single critical Deborah number* $\mathrm{De_{I,c}}$ *exists in the* $2\,\mu m$ *tall channel while there are two critical Deborah numbers for the nanochannels,* $\mathrm{De_{I,c1}}$ *and* $\mathrm{De_{I,c2}}$. *(D–F) The effective conformational energy* (E/k_BT) *of the dumbbell as a function of* X *at different values of* $\mathrm{De_I}$ *for the* $2\,\mu m$ *tall channel (D), the 300 nm tall channel (E), and the 150 nm tall channel (F). The energy landscapes at the critical Deborah numbers in each channel are highlighted with the black solid lines.*

for the interpretation of the coil-stretch transition [28, 29, 116, 122, 123]. From Equation 6.11, we can define an effective dumbbell conformational free energy E that satisfies $\psi \sim \exp(E/k_BT)$:

$$\frac{E(X,\theta)}{k_BT} = 3N\left[\int_0^X \frac{H}{H_{\text{bulk}}} x f(x)dx - \text{De}_{\text{I}} X^2 \cos(2\theta)\right] \tag{6.16}$$

We consider a dumbbell at steady-state and assume it is completely aligned with the axis of elongation ($\theta = 0$). The electrophoretic stretching force exerted on each bead now varies linearly with the dumbbell extension: $F_{\text{E}} = \frac{1}{2}\zeta\dot{\varepsilon}R$. We nondimensionalize the force with k_BT/p, giving $\widehat{F}_{\text{E}} = F_{\text{E}}p/k_BT = 3\text{De}_{\text{I}}X$. The dimensionless spring force is given by $\widehat{F}_{\text{S}} = F_{\text{S}}p/k_BT = \frac{3}{2}\frac{H}{H_{\text{bulk}}}Xf(X)$ and reduces to $\widehat{F}_{\text{S}} = \frac{3}{2}\frac{H}{H_{\text{bulk}}}X$ at small values of X. The effective conformation energy of the dumbbell as a function of X is calculated with Equation 6.16 by setting $\theta = 0$. Figure ?? shows the comparison between $\widehat{F}_{\text{E}}$ at the critical Deborah numbers and the dumbbell spring force $\widehat{F}_{\text{S}}$ for each channel, as well as the corresponding effective conformational energy landscapes at several different values of De_{I}. The critical Deborah numbers are determined by seeking local maxima of the predicted standard deviations (see insets of Figure 6.6A–C): $\text{De}_{\text{I,c}} = 0.55$ for the $2\,\mu$m tall channel, $\text{De}_{\text{I,c1}} = 0.3$ and $\text{De}_{\text{I,c2}} = 0.6$ for the 300 nm tall channel, $\text{De}_{\text{I,c1}} = 0.18$ and $\text{De}_{\text{I,c2}} = 0.65$ for the 150 nm tall channel.

Figure 6.6A shows the force comparison for the $2\,\mu$m tall channel in which the bulk spring force law applies. It is clearly seen that the linear region of the spring force is balanced by the stretching force at the critical Deborah number. This force balance creates a flat effective energy profile within the entire bulk linear force regime (see Figure 6.6D), indicating that the dumbbell has equal probability to sample at any of these end-to-end extensions ($0 \leq X < 0.3$) and thus exhibits large extension fluctuations. At $\text{De}_{\text{I}} < \text{De}_{\text{I,c}}$, the stretching force is lower than the spring force at all extensions (except for $X = 0$) so the dumbbell remains collapsed. This collapsed state is also implied by the effective energy landscape that shows a single minimum at $X = 0$ at these small values of De_{I}. Once De_{I} is increased above $\text{De}_{\text{I,c}}$, the stretching force becomes larger than the spring force within the linear force regime and we observe the formation of a deep energy well with the minimum point now located at a much higher extension (beyond the linear force regime). As a result, the linear nature of the bulk spring force at small extensions induces this sudden shift in the location of the energy minimum, and eventually leads to the sharp coil-stretch transition.

In the nanochannels, the presence of two linear regimes with different spring constants in the DNA spring law is responsible for the two critical strain rates in the coil-stretch transition. As shown in Figure 6.6B and C, the confined linear force regime at small extensions and the truncated bulk linear force regime at larger extensions are balanced by the stretching force at two different critical Deborah numbers, $\text{De}_{\text{I,c1}}$ and $\text{De}_{\text{I,c2}}$, respectively. The force balance is clearly seen at $\text{De}_{\text{I,c1}}$ but less evident at $\text{De}_{\text{I,c2}}$ especially for the 150 nm tall channel. Alternatively, the effective energy landscape can provide a much clearer demonstration of this force balance because the exact superposition of the stretching force and the spring force is not required for a relatively flat energy profile: we observe in Figure 6.6E and F that the energy landscape becomes flat within the range of extensions where the magnitudes of $\widehat{F}_{\text{E}}$ and $\widehat{F}_{\text{S}}$ are close to each other at both critical Deborah numbers. Early stretching occurs once the Deborah number exceeds $\text{De}_{\text{I,c1}}$ as the effective energy starts to show a clear minimum at $X > 0$. The stretching process, however, is limited by the nonlinear transition region of the spring force (indicated as the red lines in Figure 6.6B and C). For Deborah numbers between $\text{De}_{\text{I,c1}}$ and $\text{De}_{\text{I,c2}}$, the nonlinear spring force restricts the locations of the energy minimum to extensions within the transition region, and thus results in a more gradual increase in extension with $\mathrm{De_I}$.

Using the simple scaling of $\widehat{F}_\mathrm{E} \sim \widehat{F}_\mathrm{S}$, we can estimate the values of the critical Deborah numbers for all three channel heights. For the $2\,\mu$m tall channel $H = H_\mathrm{bulk}$ and thus $\widehat{F}_\mathrm{S} = \frac{3}{2}X$ in the linear force regime, giving $\mathrm{De_{I,c}} \sim 0.5$. For the nanochannels, the spring force is given by $\widehat{F}_\mathrm{S} = \frac{3}{2}\frac{H_\mathrm{low}}{H_\mathrm{bulk}}X$ and $\widehat{F}_\mathrm{S} = \frac{3}{2}X$ in the two linear regimes, respectively. The resulting two critical Deborah numbers are $\mathrm{De_{I,c1}} \sim H_\mathrm{low}/2H_\mathrm{bulk}$ (this yields $\mathrm{De_{I,c1}} \sim 0.24$ for the 300 nm tall channel and $\mathrm{De_{I,c1}} \sim 0.13$ for the 150 nm tall channel), and $\mathrm{De_{I,c2}} \sim 0.5$. The estimations of the critical Deborah numbers from the scaling analysis are similar to these determined from the standard deviation data.

The magnitude of the steady-state extension fluctuation is directly linked to the flatness of the effective conformational energy landscape. From Figure 6.6D–F we see that as the channel height decreases, the effective energy for a molecule at equilibrium (i.e., $\mathrm{De_I} = 0$) shows a more gradual increase from $X = 0$ due to the reduced spring constant at these small extensions. As a result, a thermal disturbance ($\Delta E \sim k_\mathrm{B}T$) produces a larger change in extension in the more confined channel, consistent with the enhanced equilibrium fluctuations observed in experiments. At the critical strain rates in each channel, the magnitude of the standard deviation σ is proportional to the span of extension over which the effective energy has a flat profile. Since the flat energy landscape results from the balance of the stretching force with the linear region of the spring force, the width of the corresponding linear spring force regime essentially determines the value of σ at these critical strain rates. A decrease in channel height broadens the confined linear force regime and narrows the truncated bulk linear force regime (see Figure 6.4D), leading to an increased peak in the standard deviation at $\mathrm{De_{I,c1}}$ and a suppressed peak at $\mathrm{De_{I,c2}}$, as observed in Figure 6.5B. Finally, we point out that the existence of two critical strain rates in the coil-stretch transition requires two distinct ranges of extensions where the spring force keeps strong linearity. As discussed in section 6.3.2, further decrease in the channel height from 150 nm may push the transition region into the nonlinear regime of the spring force (i.e., $X > 0.3$) and the resulting spring force law returns to possessing a single linear force regime. Under this condition, we postulate that a single peak in the standard deviation exists at $\mathrm{De_{I,c}} \sim H_\mathrm{low}/2H_\mathrm{bulk}$ and the coil-stretch transition is again characterized by a single critical strain rate. These effects of further confinement are yet to be examined.

6.5 Conclusions

We have used a nanofluidic cross-slot device to investigate the influence of slit-like confinement on the coil-stretch transition of single DNA molecules in a 2D homogeneous extensional electric field. We examine the evolution of three steady-state properties with applied strain rate that characterize the coil-stretch transition: the average extension, the magnitude of extension fluctuations, and the molecular orientations in the extensional electric field. Comparing with the sharp transition occurred near a single critical strain rate in the unconfined case, DNA molecules in the nanochannels exhibit highly modified coil-stretch processes. Specifically, the onset of DNA stretching starts earlier, the transition progresses more gradually, and most importantly, we identify two distinct critical strain rates in the transition. Prior to the conformation transition, DNA shows much faster alignment with the stretching electric field in the nanochannels. We have constructed a Brownian dumbbell model in which the confinement effects are represented with a constant drag coefficient and an extension-dependent spring constant extracted from experimental relaxation data. The dumbbell model is able to provide qualitative predictions of the coil-stretch transition of DNA in confinement. By exploring the interplay between the stretching force and the spring force as well as the effective energy landscape of the dumbbell model, we conclude that the essential physical reason for the different coil-stretch transition is the altered DNA spring force law which for the channel heights studied here contains two linear force regimes with distinct spring constants. Further experiments should be performed to explore the effects of even stronger confinement. Our results are not only of fundamental importance to the understanding of the interactions between confinement and a deforming polymer, but also useful in the design of devices aiming to exploit confinement to manipulate DNA molecules.

CHAPTER 7

Equilibrium Dynamics of DNA in Strong Slit-like Confinement

We experimentally investigated the equilibrium conformation and dynamics of single DNA molecules in slit-like nanochannels. Our goal is to provide more insight into the behaviors of polymers within the two regimes of slit-like confinement where existing studies show inconsistent results. We measured the in-plane radius of gyration ($R_{||}$), diffusivity (D), and longest relaxation time (τ) of λ-DNA (48.5 kbp) as functions of the slit height using fluorescence microscopy. Our results show that the in-plane radius of gyration increases monotonically with decreasing slit height, in contrast to results from Bonthuis et al. [60], but in agreement with our simulations and those of other groups. In strong confinement (slit height $< 100\,\text{nm}$), the scaling of D, τ, and $R_{||}$ with slit height does not show an evident change, suggesting that the transition from the de Gennes regime to the Odijk regime is gradual and broad. This work was done in collaboration with Stephen L. Levy form Cornell University (nanoslit fabrication), Daniel W. Trahan (Brownian dynamics simulation), and Jeremy J. Jones (experiments with TE buffer).

7.1 Introduction

Although scaling theories for the properties of polymers under confinement have been proposed for years [43, 44, 45, 46, 52, 53], experimental investigations have only recently begun to be carried out. With the advances in microfabrication technologies, it is now possible to fabricate fluidic channels with well-defined geometries and characteristic dimensions on a scale of tens to hundreds of nanometers. Those devices, combined with fluorescence microscopy, have allowed the direct experimental observation of the conformation and dynamic behavior of highly confined polymers. Such knowledge can be used to not only test and refine existing theories of polymer physics, but also guide the design and optimization of devices for the manipulation of biological macromolecules such as DNA [16,47].

Slit-like confinement has served as a prominent platform in establishing scaling concepts for confined polymers [43,44]. Unlike the pseudo-biaxial confinement in circular, square, or rectangular nanochannels, slit-like nanochannels offer a uniaxial confinement that constrains the polymer's orientational and translational degrees of freedom in only one dimension. The response of a polymer depends strongly on the strength of the confinement and different regimes of confinement can be distinguished. Three competing length scales affect the final conformation of the chain: the 3D bulk radius of gyration $R_{g,\mathrm{bulk}}$, the persistence length p of the polymer, and the the height h of the confining slit. In weak confinement where $h \sim 2R_{g,\mathrm{bulk}}$, the initial squeezing of the chain by the confining walls results in a decrease of the polymer's 3D size, as shown by Cordeiro et al. [124] using variational theory. Upon further confinement, the repulsive (excluded-volume) interactions between chain segments cause the chain to expand. In moderate confinement where $p \ll h < R_{g,\mathrm{bulk}}$ (de Gennes regime), the dynamics of a polymer has been characterized by Brochard and de Gennes [43,44] using blob theory. The theory describes a confined polymer as a string of self-avoiding blobs with diameter equal to the slit height h and yields scaling predictions for the equilibrium size, diffusivity, and longest relaxation time of the polymer. The blob description of the chain breaks down as the slit height h approaches the persistence length p, because the orientational and translational degrees of freedom become restricted (in the height dimension) even at the length scale of a single statistical segment. Instead, Odijk proposed [46,52,53] a deflection chain theory which argues that in such strong confinement, the chain contour can be stored only through successive deflections of the chain from the wall.

A number of experimental [56,57,59,60,61,62,63,125] and simulation [55,126,127,128,129,130] studies have been conducted to quantitatively probe the equilibrium dynamics of polymer confined in nanoslits and test the above theories. Much progress has been made in understanding the polymer dynamics in the de Gennes regime (see reviews by Hsieh and Doyle [115], Levy and Craighead [64], and Graham [131]). Both experiments [56,57,59,125] and simulations [55] have provided consistent and compelling evidence suggesting that the framework of blob theory provides an adequate description of the conformation and dynamics of polymer under moderate slit-like confinement. Though, it has been shown [57] that the blobs are partial draining which is a minor correction to the assumptions of blob theory. Blob theory was shown to accurately predict the scalings of polymer's equilibrium size R with respect to chain length L_c and channel height h, as well as the scalings of the diffusivity D and longest relaxation time τ with respect to L_c. The dependence of D and τ on the slit height h found in these studies, however, were slightly weaker than predicted by blob theory [56,57]. By assessing each individual assumption made in blob theory, Hsieh et al. [57] revealed that the origin of this discrepancy is solely due to the partial-draining nature of the blobs.

In contrast to the sound understanding gained for moderate confinement, a less clear picture has been established regarding the behavior of polymer in both weak confinement and strong confinement (Odijk's deflection chain regime), primarily because of the contradictory results presented in existing studies. In weak confinement, early studies by van Vliet and ten Brinke [126,127] using Monte Carlo simulations have shown a non-monotonic behavior of the 3D radius of gyration of a self-avoiding walk confined in slits, in accord with predictions of Cordeiro et al. [124]. Cifra and Bleha [128] also used Monte Carlo simulation to investigate a similar problem and characterized the behavior of both the mean-square 3D end-to-end distance ($\langle R_{3d}^2 \rangle$) and the projection of the end-to-end distance into the confining plane. Their results confirmed the initial dip of $\langle R_{3d}^2 \rangle$ upon slit-like confinement. However, the 2D projection of the end-to-end distance showed a monotonic increase from its bulk value with decreasing slit height. Similar trend of the 2D projections of both the end-to-end distance and maximum extension was reported in simulations performed by Hsu and Grassberger [129] and Chen et al. [55]. Bonthuis et al. [60] recently measured the projected in-plane radius of gyration ($R_{\|}$) of DNA confined in nanoslits using fluorescence microscopy. Contrary to findings from simulations, the in-plane radius of gyration was larger than its bulk value at $h \approx 2R_{\|,\mathrm{bulk}}$, and was first reduced upon further confinement until $h \approx R_{\|,\mathrm{bulk}}/2$. Uemura et al. [63] also claimed to have experimentally observed the initial decrease of the 2D length of DNA molecules in weak slit-like confinement though the errors of their data overlap. In another experimental study, Lin et al. [62] investigated the 2D extension of DNA confined in nanoslits. Although the same DNA substrate was used and the range of slit height studied by Lin et al. is very similar to that in experiments of Bonthuis et al., the measured extension increased monotonically with decreasing slit height.

Disagreement also exists in studies attempting to probe the transition from the de Gennes regime to Odijk regime in nanoslits. The onset of the Odijk regime has been reported for square nanochannels by Reisner et al. [98] using single molecule DNA experiments. The measured scalings of DNA extension and relaxation time (determined from the stretch autocorrelation function) versus channel dimension h showed a strong discontinuity around $h \approx 100\,\mathrm{nm}$, about twice the DNA persistence length. The experimental scalings of both variables at $h < 100\,\mathrm{nm}$ were found to be in agreement with Odijk's deflection chain theory. For nanoslits (channel width much larger than the polymer size), however, the applicability of the theory remains a question because the assumptions of small fluctuations is not satisfied in the width dimension [52]. Several studies have suggested the transition between de Gennes regime and Odijk regime in nanoslits to be gradual and broad. Balducci et al. [56] measured the diffusivity of DNA in nanoslits over a wide range of slit height ($0.4 < R_{g,\mathrm{bulk}}/h < 14$). No drastic change in the scaling of diffusivity with h was observed when the slit height approached the DNA persistence length. Strychalski et al. [61] also experimentally examined DNA diffusivity in nanoslits and extended the measurements into more shallow slits with height well below the DNA persistence length. No evident transition to the Odijk regime was identified even at a channel height of $h = 28\,\mathrm{nm}$, about half the persistence length. Instead, their diffusivity data followed a single power law over the full range of confinement studied, from 541 to 28 nm, and the extracted exponent was in good agreement with that reported by Balducci et al.. Odijk [53] employed the Flory approach of minimizing the free energy of a confined polymer and proposed a scaling argument for the chain's equilibrium size. The scaling is identical with that predicted by blob theory as will be shown. Cifra et al. [130] performed Monte Carlo simulation of wormlike chain confined in slit. A rather mild change in the scaling of the end-to-end distance with channel height h was observed when h becomes smaller than the persistence length of the chain. On the other hand, Bonthuis et al. [60] measured the scaling of the in-plane radius of gyration and the relaxation time of DNA versus channel height in nanoslits. The scaling of both quantities displayed a sharp change at $h \approx 100\,\mathrm{nm}$ which Bonthuis et al. attribute to the onset of the Odijk regime.

The in-plane radius of gyration beyond this transition channel height becomes independent of h, in disagreement with Odijk's prediction, and the relaxation time of DNA decreases with channel height. Lin et al. [62] also measured a plateau in the extension of DNA in nanoslits when the channel height is below the persistence length.

The purpose of the current study is to provide more insight into the conformation and dynamics of polymers within the two regimes of slit-like confinement where existing studies show inconsistent results. We use DNA as the model polymer and present experimental measurements of the in-plane radius of gyration, diffusivity, and the longest relaxation time of DNA confined in nanoslits with height varying from $8.5\,\mu$m to 32 nm. We also report the 3D conformation of DNA molecules in slit-like confinement obtained from Brownian dynamics simulations. There are two major focuses of this study: (1) investigating the response of DNA conformation to weak confinement, and (2) probing whether a sharp transition between the de Gennes regime and Odijk regime exists in nanoslits.

7.2 Scaling Arguments for Polymer Dynamics in Nanoslits

In this section we briefly review the scaling predictions for polymers in slit-like confinement. We consider a linear polymer consisting of N statistical segments with length $2p$ in good solvent and confined in a slit with height h, where p is the persistence length.

7.2.1 Moderate Confinement: $p \ll h < R_{g,\text{bulk}}$

The behavior of a chain under moderate confinement where $p \ll h < R_{g,\text{bulk}}$ has been treated by de Gennes et al. [43,45] using blob theory. The theory assumes (1) the polymer can be modeled as a string of blobs with each blob having a diameter h, (2) statistical segments within each blob are not aware of the presence of the confinement and retain their 3D orientational and translational freedom as if they were in bulk, (3) the blobs follow a 2D self-avoiding walk, and (4) each blob is considered non-draining (i.e., segments within a blob interact hydrodynamically) while there are no hydrodynamic interactions between blobs.

From the Flory theory [68], the bulk radius of gyration of the polymer follows the scaling $R_{g,\text{bulk}} \sim v^{1/5}p^{2/5}N^{3/5} \sim L_c^{3/5}(pw)^{1/5}$ where w is the effective diameter of the polymer, $v \approx wp^2$ is the excluded volume of a single segment, and $L_c = 2Np$ is the contour length. For a charged polymer such as DNA, the effective diameter w can deviate significantly from the bare diameter [132]. Using assumption (2) and the bulk scaling, one can estimate the number of polymer segments in each blob (g) as

$$g \sim h^{5/3}p^{-4/3}w^{-1/3} \tag{7.1}$$

The total number of blobs is thus given by $N_{\text{blob}} = N/g$. Assumption (3) allows one to extract the scaling of the equilibrium size of the chain (R):

$$R^2 \sim h^2 N_{\text{blob}}^{3/2} \sim L_c^{3/2}h^{-1/2}(pw)^{1/2} \tag{7.2}$$

The drag coefficient of the chain can be estimated using assumption (4):

$$\zeta_{\text{chain}} \sim \zeta_{\text{blob}}N_{\text{blob}} \sim \eta h N_{\text{blob}} \sim \eta L_c h^{-2/3}(pw)^{1/3} \tag{7.3}$$

where η is the solvent viscosity. The scaling of diffusivity can thus be written as

$$D \sim \frac{k_{\mathrm{B}}T}{\zeta_{\mathrm{chain}}} \sim \eta^{-1} L_c^{-1} h^{2/3} (pw)^{-1/3} \tag{7.4}$$

The spring constant H of a polymer near equilibrium has been shown [44,45] to be $H \sim k_{\mathrm{B}}T/R^2$. The longest relaxation time τ is therefore given by

$$\tau \sim \frac{\zeta_{\mathrm{chain}}}{H} \sim R^2 \zeta_{\mathrm{chain}} \sim \eta L_c^{5/2} h^{-7/6} (pw)^{5/6} \tag{7.5}$$

The assumptions made in the blob theory have been examined in detail in several experimental studies [56,57]. Only the assumption of non-draining blob was found compromised, which leads to deviations in the predicted h-dependence of Equation 7.4 and 7.5.

7.2.2 *Strong Confinement: $h < p$*

In confinement with $h < p$, a less complete theoretical understanding of the static and dynamic properties of single polymer in nanoslits has been reached. Odijk [46] proposed a deflection chain theory to describe the behavior of a semiflexible polymer confined in a circular tube with the diameter much smaller than p. A new length scale was derived as the deflection length $\lambda \sim p^{1/3} h^{2/3}$ and the polymer chain was treated as a series of rigid rods of length λ that reflect off the channel boundary [46]. The deflection chain theory was further generalized for square and rectangular nanochannels [52,53] and it was suggested that the dynamics of polymer in strong confinement is greatly complicated by the formation of hairpins and thus the transition from the de Gennes regime to the Odijk regime is nontrivial.

Although deflection chain theory has yielded close predictions of chain extensions in square and rectangular nanochannels comparing to experimental results [16,98], it is still an open question whether the theory can be directly adapted to nanoslits with width much larger than p. Odijk [53] recently developed a scaling for the size of a highly confined chain in nanoslits using the Flory approach. He treated the polymer as L_c/λ rod segments squeezed into a 2D pancake with diameter R and height h. Due to the large channel width, the global persistence length [52] equals to the chain persistence length p and the rod segments retain their orientational degree of freedom in directions parallel to the confining plane. Assuming the slit height is much larger than the effective width of the chain ($h \gg w$), the excluded volume of a single segment hence scales as $\beta \approx \lambda^2 w$ and the free energy of the chain is given by (Equation 21 in Ref. [53])

$$\frac{F}{k_{\mathrm{B}}T} \approx \frac{R^2}{L_c p} + \frac{\beta (L_c/\lambda)^2}{R^2 h} \tag{7.6}$$

The first term in Equation 7.6 is the elastic energy needed to extend the chain to an extension of R, and the second term rises from the repulsive interactions (excluded-volume effects) of all L_c/λ chain segments. Minimization of F with respect to R yields

$$R^2 \sim (L_c p) \left(\frac{L_c w}{ph} \right)^{1/2} = L_c^{3/2} h^{-1/2} (pw)^{1/2} \tag{7.7}$$

The final result of Equation 7.7 is identical to that of Equation 7.2, suggesting that the scalings of

R versus L_c and h do not change from the de Gennes regime to the Odijk regime. We note that the above derivation requires the second term in Equation 7.6 to be greater than unity (i.e., the energy from the excluded-volume effects larger than k_BT). Substituting the result of Equation 7.7 into Equation 7.6, one obtains

$$\frac{\beta(L_c/\lambda)^2}{R^2 h} \sim \left(\frac{L_c w}{ph}\right)^{1/2} \tag{7.8}$$

Therefore, Equation 7.7 is only valid when the excluded-volume parameter [53] $Z \sim L_c w/ph$ satisfies $Z > 1$. Otherwise the behavior of the chain is effectively that of an ideal chain and its size remains constant as $R^2 \sim L_c p$.

Following the deflection chain picture and assuming no hydrodynamic interactions between chain segments, the drag coefficient of the chain can be estimated to be [56] $\zeta_{\text{chain}} \sim \zeta_{\text{rod}}(L_c/\lambda)$ where ζ_{rod} represents the drag coefficient of one rod segment. In a circular tube where hydrodynamic interactions are screened at a length scale equal to the tube diameter d_{tube}, ζ_{rod} is given by $\zeta_{\text{rod}} \sim \eta\lambda/\log(d_{\text{tube}}/d_{\text{h}})$ with d_{h} the hydrodynamic diameter of the chain [133]. In nanoslits, however, the decay of the far-field velocity magnitude is not exponential [134], and we write ζ_{rod} as $\zeta_{\text{rod}} \sim \eta\lambda/f(h)$ where $f(h)$ is a factor depending on the slit height. The diffusivity can thus be expressed as

$$D \sim \frac{k_BT}{\zeta_{\text{chain}}} \sim \eta^{-1} L_c^{-1} f(h) \tag{7.9}$$

Equation 7.4 and 7.9 suggest that the L_c^{-1} dependence of D is expected for all slit heights, which was verified recently in single molecule DNA experiments [61].

Polymer chains are not significantly elongated in nanoslits even when the slit height becomes smaller than the persistence length [62, 130]. Therefore, one can assume the spring force remains linear near equilibrium and the longest relaxation time still keeps the same L_c-dependence:

$$\tau \sim R^2 \zeta_{\text{chain}} \sim \eta L_c^{5/2} \tag{7.10}$$

7.3 Experiments

7.3.1 Channel and DNA Preparation

The nanoslits used in this study were fabricated from fused-silica wafers (Mark Optics) using two layers of contact photolithography and reactive ion etching (CHF_3/O_2) as described previously [61]. The device consisted of one 150 μm wide, 1 mm long nanoslit in the center and two 1 cm long deep regions on the sides of the slit. The channel depths were determined using a Tencor P-10 surface profiler and range from 32-560 nm. A 2 μm tall glass channel was donated by U.S. Genomics. A 8.5 μm tall channel was constructed in polydimethylsiloxane (PDMS, Sylgard 184, Dow Corning) using soft lithography on a silicon master (SU8-2 photoresist).

λ-DNA (48.502 kbp, New England Biolabs) suspended at a concentration of 0.69 μg/mL was stained with YOYO-1 (Invitrogen) dye at a base pair to dye ratio of 4:1 and allowed to sit at least overnight. DNA samples were diluted 2–10-fold immediately before experiments to reach an optimal concentration for observation. Two types of experimental buffer were used: (1) 1.5×TBE (270 mM Tris base, 270 mM boric acid, and 6 mM EDTA); (2) 1×TE (10 mM Tris base and 1 mM EDTA), 50 mM NaCl. In both buffers an oxygen scavenger system consisting of 4% (vol) β-mercaptoethanol (BME, Cabiochem), 12.5 mg/mL glucose (Mallinckrodt), 0.16 mg/mL glucose oxidase (Sigma), and

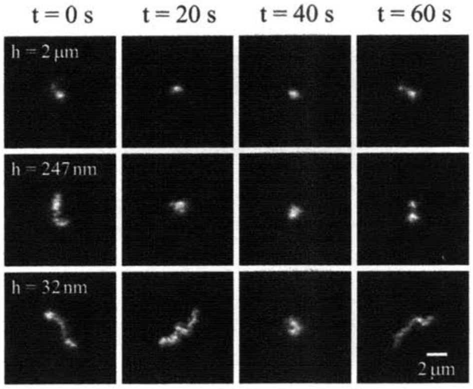

Fig. 7.1: *Snap shots of λ-DNA molecules confined in the 2 µm, 247 nm, and 32 nm tall nanoslits. For each nanoslit, images of a single molecule are shown and the time interval between images is 20 s.*

9.6 µg/mL catalase (Sigma) was incorporated. The buffer viscosities were determined to be 1.17 cP for the TBE buffer and 1.15 cP for the TE buffer at 22.5°C by measuring the diffusivity of 0.925 µm polystyrene beads (Polysciences). The buffer ionic strengths were estimated to be 56.9 mM in the TBE buffer and 60.3 mM in the TE buffer.

7.3.2 Experimental Procedure

Nanoslits were filled via capillarity with a filtered solution of 50% ethanol and 50% deionized water. The device was then thoroughly rinsed with deionized water via application of potentials at the fluid reservoirs. The channel was further flushed with filtered 1 M NaOH for 4 minutes to remove any residual chemicals left from the fabrication process, and rinsed again with water. Prior to each experiment, the channels were flushed with the experimental buffer for 1 hour. DNA molecules were electrokinetically driven into the nanoslits using an electric field between 20 and 50 V/cm. A typical experiment involves identifying a molecule of interest, turning off the electric field, waiting for 1 minute to allow the molecule to equilibrate from any deformation occurred while traveling in the channel, and then starting image acquisition. We used an inverted Zeiss Axiovert 200 microscope with a 100× NA 1.4 oil-immersed objective and an X-Cite 120 light source to observe single DNA molecules. Images were captured using a Hamamatsu EB-CCD camera (model 7190-21) and NIH image software at a rate of 30 frames/second for all experiments. 3600 frames (2 minutes) were collected for each molecule. Averages were taken over ensembles containing 30-70 different molecules per channel.

7.3.3 Data Analysis

We note that the DNA image taken from the fluorescence microscopy is a projection of the 3D molecule onto the *x*-*y* plane (parallel to the confining channel walls) and thus does not explicitly contain information regarding the DNA size in the *z*-dimension (channel height dimension).

The images were processed using custom-developed code in Interactive Data Language (IDL). A background image was subtracted from the image before the analysis. Figure 7.1 shows typical images (background subtracted) of λ-DNA in the channels. It is clearly seen that as the slit depth decreases, DNA molecule becomes more extended. We calculate the center of mass vector $\mathbf{r}_{\mathrm{cm}}$ and the radius of gyration tensor $\mathbf{G}$ of the DNA in each frame:

$$\mathbf{r}_{\mathrm{cm}}(t) = \frac{\sum \mathbf{r}(t) I(\mathbf{r}, t)}{\sum I(\mathbf{r}, t)} \tag{7.11}$$

$$\mathbf{G}(t) = \frac{\sum [\mathbf{r}(t) - \mathbf{r}_{\mathrm{cm}}(t)][\mathbf{r}(t) - \mathbf{r}_{\mathrm{cm}}(t)] I(\mathbf{r}, t)}{\sum I(\mathbf{r}, t)} \tag{7.12}$$

where the sum was taken over all pixels spanned by the molecule, $\mathbf{r}$ is the position vector, and $I(\mathbf{r}, t)$ is the fluorescence intensity at position $\mathbf{r}$. The in-plane diffusivity D can be obtained from the mean-square-displacement (MSD):

$$\mathrm{MSD}(\delta t) = \mathrm{MSD}_x(\delta t) + \mathrm{MSD}_y(\delta t) = 4D\delta t \tag{7.13}$$

where δt is the lag time, $\mathrm{MSD}_x(\delta t) = \langle [r_{\mathrm{cm},x}(t + \delta t) - r_{\mathrm{cm},x}(t)]^2 \rangle$, and $\mathrm{MSD}_y(\delta t) = \langle [r_{\mathrm{cm},y}(t + \delta t) - r_{\mathrm{cm},y}(t)]^2 \rangle$. Figure 7.2A and B show results of the center of mass trajectories and the MSD curves for λ-DNA in a 90 nm channel. In the absence of appreciable background flows, the center of mass trajectories yield a symmetric distribution, and the MSD values calculated for both the x-direction and y-direction agree well with each other.

The radius of gyration tensor $\mathbf{G}$ is related to the instantaneous size, shape, and orientation of the DNA. The 2D image of a molecule is described as an ellipse with the radii R_{M} and R_{m} of its major and minor principal axes given by

$$R_{\mathrm{M}} = 2\sqrt{\lambda_1}, \quad R_{\mathrm{m}} = 2\sqrt{\lambda_2} \tag{7.14}$$

where λ_1 and λ_2 ($\lambda_1 \geq \lambda_2$) are the eigenvalues of $\mathbf{G}$. The in-plane two-dimensional radius of gyration, denoted as $R_{\|}$, is given by the square root of the trace of $\mathbf{G}$ or

$$R_{\|} = \frac{1}{2}\sqrt{R_{\mathrm{M}}^2 + R_{\mathrm{m}}^2} \tag{7.15}$$

The angle between the major principal axis of the DNA and the x-axis is [135]

$$\theta(t) = \arctan\left(\frac{\lambda_1(t) - G_{xx}(t)}{G_{xy}(t)}\right), \; -\frac{\pi}{2} < \theta < \frac{\pi}{2} \tag{7.16}$$

The longest rotational relaxation time τ_{r} and the longest stretch relaxation time τ_{s} are the characteristic times describing the slowest mode of the polymer's internal motion. τ_{r} and τ_{s} can be extracted by fitting a single-exponential function to the time autocorrelation function of $\theta(t)$ and $R_{\|}(t)$, respectively. The rotational autocorrelation function is defined as [57,135]

$$C_{\mathrm{r}}(\delta t) = \frac{\langle (\theta(t + \delta t) - \theta_0)(\theta(t) - \theta_0) \rangle}{\langle (\theta(t) - \theta_0)^2 \rangle} \sim \exp(-\delta t/\tau_{\mathrm{r}}) \tag{7.17}$$

where θ_0 is the equilibrium average of $\theta(t)$ and is taken to be zero in the calculation because the average orientation of a DNA is isotropic [57]. We have also verified this assumption from the experimental measurements (data not shown). The stretch autocorrelation function is defined as

$$C_s(\delta t) = \frac{\langle (R_{||}(t+\delta t) - R_{||,0})(R_{||}(t) - R_{||,0})\rangle}{\langle (R_{||}(t) - R_{||,0})^2\rangle} \sim \exp(-\delta t/\tau_s) \tag{7.18}$$

where $R_{||,0}$ is the equilibrium average of $R_{||}(t)$. We note that the rotational relaxation time obtained with our method is half of the true τ_r because the phase space is cut to half by defining the orientation of the major axis to be in between $-\pi/2$ and $\pi/2$. In this case τ_r and τ_s should equal to each other for a polymer chain in either a theta or good solvent [68,69].

7.3.4 Effects of Photobleaching

Photobleaching of the fluorescent dye is always a practical concern in single molecule DNA experiments. The decreasing DNA fluorescent signal with time produces an apparent decay in the DNA size as measured by image analysis. For example, Figure 7.2C shows that the ensemble average fluorescence intensity of λ-DNA in a 90 nm tall slit drops by about 40% after 2 minutes of observation. Figure 7.2D displays the measured average in-plane radius of gyration $R_{||}$ as a function of frame number (time). Despite the large degree of fluctuations, an overall decrease of $R_{||}$ can be observed, as indicated by the black line which is a linear fit of the data. This decay in the measured $R_{||}$ was observed for all slit heights. Photobleaching may also physically shorten the contour length of the DNA with time and thus change the dynamic properties of the molecule. The DNA is expected to diffuse and relax faster if it becomes shorter. Hence, we examine whether the DNA molecules remains intact by checking the time variation of both the diffusivity and relaxation time during the course of an experiment, as described by Hsieh et al. [57]. For the diffusivity, we cut each individual movie into six submovies and compare the MSD curves from the ensemble average of the submovies. Since much better statistics are required to obtain accurate relaxation times, we divide the movies into two submovies and compare the corresponding autocorrelation curves. Figure 7.2E and F show results of such an analysis for λ-DNA in the 90 nm tall slit. The MSD curves of the six different ensembles plotted in Figure 7.2E show nearly exact superposition at small lag times. They deviate from each other at long lag times due to limited statistics but no sign of systematic change is observed. Similar behavior of the rotational autocorrelation function was observed in Figure 7.2E, suggesting the physical properties of the DNA do not appreciably change over the course of an experiment.

7.3.5 Point Spread Function (PSF)

The DNA image captured from the fluorescence microscopy is a convolution of the true image of YOYO-1 dyes with the point spread function (PSF) of the optical system [136]. The PSF causes the apparent size of the DNA to be larger than its actual value. To quantify this effect, we determine the in-plane PSF of our imaging system by measuring the intensity profile of 50 nm fluorescent polystyrene beads immobilized onto a glass coverslip. Figure 7.3 shows the typical image of a single

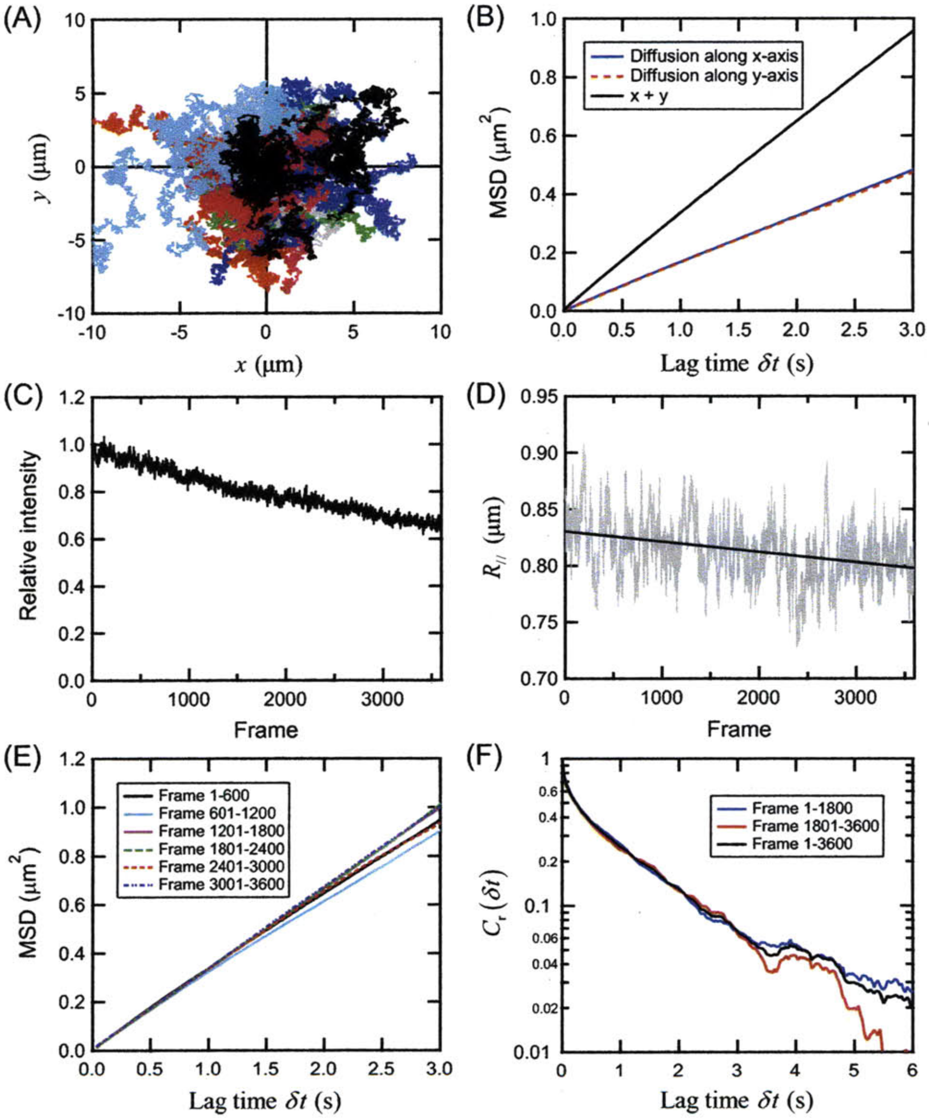

Fig. 7.2: *Summary of image analysis for* λ*-DNA in a 90 nm tall slit in the 1.5×TBE buffer. (A) Center of mass trajectories for 35* λ*-DNA molecules. (B) Mean-square-displacement (MSD) as a function of lag time. The MSD along the x-axis and y-axis are also shown. (C) Evolution of the average fluorescence intensity of* λ*-DNA (normalized by the average intensity in the first frame) with frame number (1/30 s between consecutive frames). (D) Evolution of the average in-plane radius of gyration* $R_{\|}$ *with frame number. The black line is a linear fit to the data showing an overall decrease of* $R_{\|}$ *due to photobleaching. (E) Analysis of* λ*-DNA diffusion from different time segments of the experimental movies. The MSD curves show good agreement at small lag times and fluctuate at long lag times due to limited statistics. (F) Analysis of the rotational autocorrelation function* $C_{\mathrm{r}}(\delta t)$ *from different time segments of the experimental movies.*

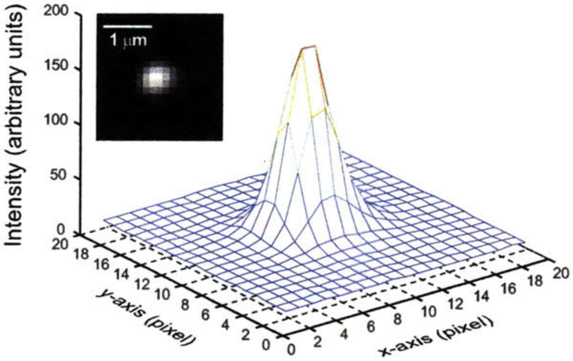

Fig. 7.3: *Typical image of a 50 nm fluorescent polystyrene bead under a 100× NA 1.4 objective and the corresponding 2D fluorescence intensity profile. One pixel corresponds to a length of 135 nm.*

50 nm bead and its 2D intensity profile. We fit the image to a 2D Gaussian function given by [137]

$$I(x, y) = I_0 \exp\left(-\frac{(x - x_0)^2 + (y - y_0)^2}{2\sigma_{\text{PSF}}^2}\right) + B \tag{7.19}$$

where I_0, x_0, y_0, σ_{PSF}, and B are fitting parameters. The standard deviation σ_{PSF} is determined to be about 190 nm. The optical resolution σ_0, which is the full width at half maximum of the point spread function, is $\sigma_0 = 2.355\sigma_{\text{PSF}} \approx 450\,\text{nm}$, significantly larger than the size of the beads used for the measurement. This value is expected from the optical resolution of our microscope system of [136] $\approx 1.22\times$excitation wavelength/NA (numerical aperture)$\approx 1.22 \times 500\,\text{nm}/1.4 \approx 440\,\text{nm}$.

7.4 Brownian Dynamics Simulations

Considering the experiments do not explicitly provide any information of the DNA conformation in the z-direction, we performed Brownian dynamics simulations of a bead-spring chain confined in slit-like channels to extract both the in-plane radius of gyration $R_{\parallel}$ and the true 3D radius of gyration R_g. We modeled λ-DNA as a bead-spring chain with N_{b} beads and $N_{\text{s}} = (N_{\text{b}} - 1)$ springs of equal length. The equation of motion for the position $\mathbf{r}_i$ of the ith bead is:

$$\frac{d\mathbf{r}_i}{dt} = \frac{1}{\zeta_{\text{b}}}\left[\mathbf{F}_i^{\text{B}}(t) + \mathbf{F}_i^{\text{S}}(t) + \mathbf{F}_i^{\text{EV}}(t) + \mathbf{F}_i^{\text{W}}(t)\right] \tag{7.20}$$

where ζ_{b} is the bead drag coefficient, $\mathbf{F}_i^{\text{B}}$ is the Brownian force, $\mathbf{F}_i^{\text{S}}$ is the total spring force felt by the bead, $\mathbf{F}_i^{\text{EV}}$ is the intrachain excluded-volume force, and $\mathbf{F}_i^{\text{W}}$ represents the interaction of the bead with the channel walls. We have neglected intrachain hydrodynamic interactions (HI) as we are only interested in the static conformation of the polymer [55]. We nondimensionalize the variables as follows:

$$\hat{\mathbf{r}} = \frac{\mathbf{r}}{l_{\rm s}}, \quad \hat{t} = \frac{t}{\zeta_{\rm b} l_{\rm s}^2 / k_{\rm B}T} \tag{7.21}$$

where $\mathbf{r}$ is position, $l_{\rm s}$ is the maximum extension of a single spring ($l_{\rm s} = L_{\rm c}/N_{\rm s}$), and t is time. We nondimensionalize the forces $\mathbf{F}$ as follows:

$$\hat{\mathbf{F}}\left(\hat{\mathbf{r}}\right) = \frac{\mathbf{F}}{k_{\rm B}T/l_{\rm s}} \tag{7.22}$$

This leads to the dimensionless form of Equation 7.20:

$$\frac{d\hat{\mathbf{r}}_i}{d\hat{t}} = \hat{\mathbf{F}}_i^{\rm B} + \hat{\mathbf{F}}_i^{\rm S} + \hat{\mathbf{F}}_i^{\rm EV} + \hat{\mathbf{F}}_i^{\rm W} \tag{7.23}$$

The dimensionless Brownian force is given by:

$$\hat{\mathbf{F}}_i^{\rm B} = \sqrt{\frac{24}{\Delta\hat{t}}}(\mathbf{r}_n)_i \tag{7.24}$$

where $\Delta\hat{t}$ is the dimensionless time step and $(\mathbf{r}_n)_i$ are uniform random numbers such that each component $(\mathbf{r}_n)_i^j \in [-1/2, 1/2]$, where j denotes the coordinate x, y, or z. The net non-dimensional spring force on the ith bead is:

$$\hat{\mathbf{F}}_i^{\rm S} = \begin{cases} \hat{\mathbf{f}}^{\rm s}_{i,2}, & i = 1 \\ \hat{\mathbf{f}}^{\rm s}_{i,i+1} + \hat{\mathbf{f}}^{\rm s}_{i,i-1}, & 1 < i < N_{\rm b} \\ \hat{\mathbf{f}}^{\rm s}_{i,N_{\rm b}-1}, & i = N_{\rm b} \end{cases} \tag{7.25}$$

where $\hat{\mathbf{f}}^{\rm s}_{i,j}$ is the force of the spring connecting the ith and jth beads developed by Underhill and Doyle [138] which closely matches the force-extension behavior of a continuous worm-like chain:

$$\hat{\mathbf{f}}^{\rm s}_{i,j} = \left[\frac{C\hat{r}_{j,i}}{(1-\hat{r}_{j,i}^2)^2} + \frac{G\hat{r}_{j,i}}{v(1-\hat{r}_{j,i}^2)} + D\hat{r}_{j,i} + B\hat{r}_{j,i}(1-\hat{r}_{j,i}^2)\right]\frac{\hat{\mathbf{r}}_j - \hat{\mathbf{r}}_i}{\hat{r}_{j,i}} \tag{7.26}$$

where C, G, D, B are numerical factors defined by Underhill and Doyle [138], v is the number of persistence lengths represented by each spring ($v = l_{\rm s}/p$), and $\hat{r}_{j,i}$ is given by $\hat{r}_{j,i} = |\hat{\mathbf{r}}_j - \hat{\mathbf{r}}_j|$. The intrachain excluded volume force $\hat{\mathbf{F}}_i^{\rm EV}$ is modeled with the soft potential used by Jendrejack et al. [139]:

$$\hat{\mathbf{F}}_i^{\rm EV} = -\sum_{\substack{j=1 \\ j\neq i}}^{N_{\rm b}} \frac{9}{2}\hat{\nu}^{\rm ev}\left(\frac{3}{4\sqrt{\pi}}\right)^3 v^{9/2}\exp\left[-\frac{9}{4}v\hat{r}_{ij}^2\right]\hat{\mathbf{r}}_{ji} \tag{7.27}$$

where $\hat{\nu}^{\rm ev} = \nu^{\rm ev}/l_{\rm s}^3$ is the dimensionless form of the excluded volume parameter $\nu^{\rm ev}$. The interactions between a bead and the walls represented by $\hat{\mathbf{F}}_i^{\rm W}$ are resolved using a modified Heyes-Melrose algorithm [140, 141]. Whenever a bead moves outside the channel domain during a time step, it is moved to the nearest point on the domain boundary before commencing the next time step:

$$\Delta\hat{\mathbf{r}}_i^{\rm HM} = \Delta\mathbf{p}_i H\left(\Delta p_i\right) \tag{7.28}$$

where $\Delta\hat{\mathbf{r}}_i^{\mathrm{HM}}$ is the displacement vector due to the Heyes-Melrose algorithm, $\Delta\mathbf{p}_i$ is the vector pointing from the bead outside the domain to the nearest boundary point, and the Heaviside step function $H(\Delta p_i)$ restricts the application of the algorithm to only the beads that have penetrated the domain boundaries.

We used $N_{\mathrm{b}} = 111$ beads to model λ-DNA ($L_c = 22\,\mu$m, $l_{\mathrm{s}} = 200\,$nm) and performed simulations for channels with height from 11 μm to 90 nm. We did not simulate DNA in channels thinner than 90 nm because the spring force law used in the bead-spring model is expected to be not valid when the channel height becomes much smaller than the Kuhn length (∼ 100 nm) [142]. We used a constant excluded-volume parameter $\nu^{\mathrm{ev}} = 1.3 \times 10^{-4}\,\mu\mathrm{m}^3$ for all channel heights. This value of ν^{ev} was determined such that the 3D bulk radius of gyration of the bead-spring chain matches the experimental value of $R_{g,\mathrm{bulk}} \approx 640\,$nm predicted from the bulk diffusivity of λ-DNA in the 1.5×TBE buffer. We used a time step of $\Delta\hat{t} = 5 \times 10^{-4}$ in all simulations. In every simulation, the bead-spring chain was initially placed in the channel with desired height at a random Gaussian configuration (neglecting configurations in which beads are present outside the channel walls). After an initial equilibration period, the 3D configurations of the chain were periodically recorded for hundreds of relaxation times. We then computed both the 3D radius of gyration tensor and the in-plane radius of gyration tensor from these configurations. For the 2D radius of gyration tensor, we have convoluted the raw chain configuration with the experimentally measured point spread function before the calculation.

7.5 Results and Discussion

7.5.1 *Conformation of DNA in Nanoslit*

We measured the in-plane radius of gyration $R_{\|}$ of λ-DNA (using Equation 7.15) from DNA images in slits with height from 8.5 μm to 32 nm. Because the values of $R_{\|}$ determined this way are consistently biased by both the point spread function and photobleaching of the dye, we only look at the qualitative aspect of the data and will not use them to develop the quantitative scaling relation between the DNA size and the slit height. A more precise estimation of the scaling exponent regarding the h-dependence of DNA size can be inferred from the product of the DNA diffusivity D and rotational relaxation time τ_{r}, as will be discussed in a later section.

The bulk in-plane radius of gyration $R_{\|,\mathrm{bulk}}$ of λ-DNA was determined from its bulk diffusivity D_{bulk} using the relations $R_{g,\mathrm{bulk}} = 0.203(k_{\mathrm{B}}T/\sqrt{6}\eta D_{\mathrm{bulk}})$ [69] and $R_{\|,\mathrm{bulk}} = \sqrt{\frac{2}{3}}R_{g,\mathrm{bulk}}$ where $R_{g,\mathrm{bulk}}$ is the bulk 3D radius of gyration. Since the measurement of the center of mass and thus the diffusivity is less sensitive to the point spread function and photobleaching, we expect the value of $R_{\|,\mathrm{bulk}}$ evaluated this way to be more accurate than that directly measured from the DNA image. The measured bulk diffusivity of λ-DNA in the 1.5×TBE buffer is $D_{\mathrm{bulk}} = 0.45 \pm 0.02\,\mu\mathrm{m}^2/\mathrm{s}$, giving $R_{g,\mathrm{bulk}} \approx 0.64\,\mu$m and $R_{\|,\mathrm{bulk}} \approx 0.52\,\mu$m. Bonthuis et al. [60] measured $R_{\|,\mathrm{bulk}} \approx 0.84 \pm 0.1\,\mu$m for λ-DNA in a solution of 10 mM Tris-EDTA and 50 mM NaCl. This value of $R_{\|,\mathrm{bulk}}$ corresponds to $R_{g,\mathrm{bulk}} \approx 1.03 \pm 0.12\,\mu$m, significantly larger than the value of $0.73 \pm 0.05\,\mu$m reported by Smith et al. [71] for λ-DNA in a similar buffer (1×TE, 10 mM NaCl).

Figure 7.4A shows the scaled ensemble average in-plane radius of gyration $\langle R_{\|}\rangle / R_{\|,\mathrm{bulk}}$ of λ-DNA as a function of h measured both in experiments for 1.5×TBE buffer and from Brownian dynamics simulations. The results reported by Bonthuis et al. [60] are also shown for comparison. The simulation results were calculated after the raw chain configurations were convoluted with

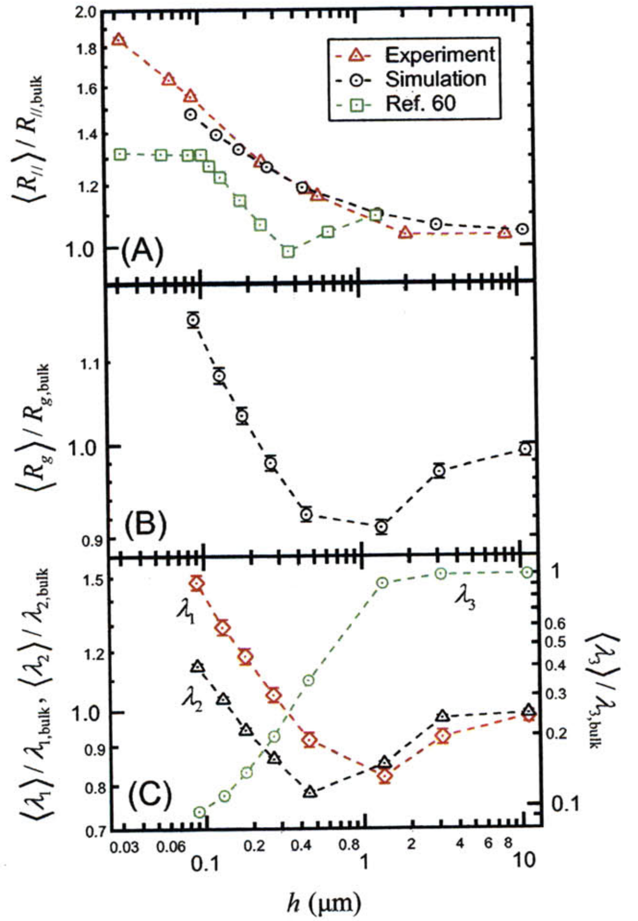

Fig. 7.4: *Dependence of different measurements of the DNA conformation on slit height h. (A) Ensemble average in-plane radius of gyration* $R_{\|}$ *(scaled by the estimated bulk value of* $0.52\,\mu m$*) measured experimentally in 1.5× TBE buffer and determined from Brownian dynamics simulations. Error is less than the size of the symbols. The experimental errors do not include the possibly large systematic components induced by the PSF of the optical system and photobleaching of the YOYO-1 dye. The simulation results have been convoluted with the experimentally measured PSF (see Figure 7.3). Also shown are the results from Bonthuis et al. [60] measured using a slightly different method. (B) Ensemble average 3D radius of gyration* R_g *(scaled by its bulk value* $R_{g,\mathrm{bulk}}$*) determined from simulations. (C) Ensemble average eigenvalues (*λ_i*, i =1, 2, 3, all scaled by their bulk values) of the three principal axes of the 3D radius of gyration tensor determined from simulations.*

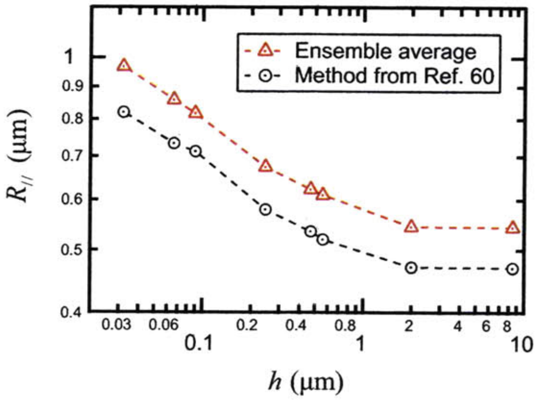

Fig. 7.5: *A comparison of the in-plane radius of gyration $R_{||}$ of λ-DNA evaluated using different methods.*

the measured PSF and yield quantitative agreement with experiments. Both our experiments and simulations show monotonic increase of $\langle R_{||}\rangle$ with decreasing h, in accord with previous simulations [55, 128, 129]. In the taller slits where $h > 2R_{g,\mathrm{bulk}} \sim 1\,\mu$m, $\langle R_{||}\rangle$ does not change significantly but stays nearly at a constant value which was slightly larger than the estimated $R_{||,\mathrm{bulk}}$ due to the point spread function. In contrast, the data of Bonthuis et al. exhibit vastly different behavior from bulk to $h \approx 400\,$nm. The measured $R_{||}$ is ~10% larger than $R_{||,\mathrm{bulk}}$ at $h = 1.3\,\mu$m, indicating there is an initial increase in $R_{||}$ from bulk to this slit height. Further decrease in h leads to a compression of $R_{||}$ until h reaches $\sim 400\,$nm, below which $R_{||}$ starts to grow again. We realize that Bonthuis et al. used a different approach to evaluate $R_{||}$ instead of taking the ensemble average: they calculated $R_{||}$ using Equation 7.15 in which the values of R_{M} and R_{m} were determined from the peaks of their distributions. We have employed this method to analyze our experimental data but the results show qualitatively the same trend with that of the ensemble average $R_{||}$ (see Figure 7.5). We notice that the data of $R_{||}$ between our experiments and the study of Bonthuis et al. also show distinct behaviors in strong confinement ($h < 100\,$nm). We will discuss these differences in a later section.

Figure 7.4B shows the scaled 3D radius of gyration $\langle R_g\rangle / R_{g,\mathrm{bulk}}$ determined from simulations without any PSF modification. It is clearly seen that R_g behaves differently from the projected 2D radius of gyration in slits with $h > 1\,\mu$m: while $\langle R_{||}\rangle$ shows a mild increase, $\langle R_g\rangle$ decreases with h from its bulk value and displays a minimum at $h \approx 2R_{g,\mathrm{bulk}}$. The trend of $\langle R_g\rangle$ and the location of its minimum observed in Figure 7.4B agree qualitatively to those reported by Cifra and Bleha [128]. Furthermore, We calculated the three eigenvalues (λ_i, i =1, 2, 3, $\lambda_1 \geq \lambda_2 \geq \lambda_3$) of the 3D radius of gyration tensor from the simulations. The eigenvalues correspond to the square radii of the three principal axes of the radius of gyration tensor and can provide more details of the chain's 3D conformation. van Vliet and ten Brinke [126] have shown previously that the two larger eigenvalues λ_1 and λ_2 exhibit very similar behaviors with that of R_g, and the smallest eigenvalue λ_3 first remains constant for $h \gg 2R_{g,\mathrm{bulk}}$ and decreases in further confinement. All these qualitative features have been reproduced by our simulations, as can be seen from Figure 7.4C where results

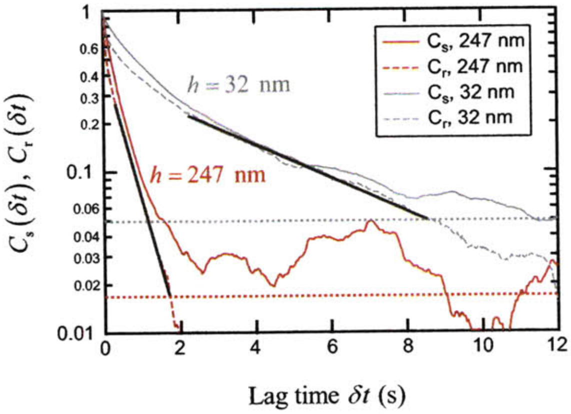

Fig. 7.6: *Curves of the rotational autocorrelation function* C_{r} *and the stretch autocorrelation function* C_{s} *versus the lag time* δt *for the 247 nm and* 32 *nm tall slits measured in the 1.5× TBE buffer. The black solid lines are single-exponential fits to the rotational autocorrelation functions which were used to extract* τ_{r}. *The red and grey dotted horizontal lines indicate the statistical noises of these measurements for the 247 nm and* 32 *nm tall slits, respectively.*

of $\langle\lambda_i\rangle/\lambda_{i,\mathrm{bulk}}$ are plotted against h.

We now point out that existing studies [124, 126, 127, 128] that have reported an initial compression of the polymer coil by slit-like confinement all refer to the 3D size of the chain, and it is non-physical for the projected 2D size to decrease with confinement. The 2D size of the chain is determined by the in-plane self-avoiding walk which depends upon the monomer density. A reduction in the z-dimension of the polymer by slit-like confinement will always increase the monomer density and the resulting increased excluded-volume interactions will force the chain to expand in the x-y plane. This monotonic increase of the 2D size of a confined polymer is verified by both our experiments and simulations, as well as simulations from several other groups [55, 128, 129]. On the other hand, the change of the 3D polymer size is a competition between the swelling in the x-y plane and the compression in the z-direction. As a coiled polymer becomes confined, the initial squeezing of the coil by the two confining planes does not significantly perturb the in-plane self-avoiding walk and the decrease in the chain's z-dimension overwhelms the expansion in the x-y plane, resulting in an overall reduction of the 3D coil size. Confinement also leads to re-orientation of the principal axes of the chain [126]. Specifically, the two longer principal axes orient toward the x-y plane and the shortest axis toward the z-direction. Before the two longer axes have considerably aligned, their radii are still affected by the z-dimension of the chain and the initial decrease of $\langle\lambda_1\rangle$ and $\langle\lambda_2\rangle$ in weak confinement is again due to the compression of the chain in the z-direction.

7.5.2 *Measuring the Longest Relaxation Time of DNA*

We computed both the rotational autocorrelation function C_r and stretch autocorrelation function C_s from the time-sequence images of DNA to extract τ_r and τ_s, respectively. The standard deviation of the autocorrelation function is

$$\sigma_C = \frac{1}{\langle u^2 \rangle}\sqrt{\langle u(t)^2 u(t+\delta t)^2 \rangle - \langle u(t)u(t+\delta t)\rangle^2} \tag{7.29}$$

where u denotes either $(\theta - \theta_0)$ or $(R_\| - R_{\|,0})$. The standard deviation reaches its maximum value of 1 at sufficiently large lag time ($\delta t \gg \tau$) such that $u(t)$ and $u(t+\delta t)$ are uncorrelated. Therefore, we take the statistical noise to be $1/\sqrt{n}$ for both C_r and C_s where n is the total number of independent samples. The value of n was determined to be the product of the number of individual DNA movies collected for a given slit height and the number of independent samples in each movie taken as the length of the movie (2 minutes) divided by $3\tau_\mathrm{r}$ (or $3\tau_\mathrm{s}$).

Figure 7.6 shows examples of the autocorrelation functions measured for λ-DNA in a 247 nm and a 32 nm tall slits in the 1.5×TBE buffer. The two horizontal lines indicate the corresponding statistical noise associated with these measurements. It is clearly seen that all four curves exhibit faster initial decay at small lag times due to contributions from higher order modes [69]. The decay gradually slows down and becomes single-exponential when the numerical values of these autocorrelation functions have decreased below about 0.3, indicating the slowest mode begins to dominate. The longest rotational relaxation time τ_r and the stretch relaxation time τ_s were determined by fitting the linear regions (in a semilog scale) of the corresponding autocorrelation curves. A wide linear region, starting from $C_\mathrm{r} \sim 0.3$ and extend all the way down to statistical noise, can be identified from the two rotational autocorrelation curves, while a much smaller linear region exists in the stretch autocorrelation curves within the range $0.3 > C_\mathrm{s} > 3 \times$ Noise. The slopes of the linear regions are similar between C_r and C_s for the same slit height. Two major reasons are responsible for the inferior quality of the stretch autocorrelation function [57]. First, the apparent decay of $R_\|$ induced by photobleaching (see Figure 7.2C) disrupts the linearity of C_s (in a semilog scale). In addition, the inability to accurately determine the mean equilibrium radius of gyration $R_{\|,0}$ from experiments often causes C_s to not decay to zero in the long time limit (see curve of C_s for the 247 nm tall slit in Figure 7.6). In contrast, photobleaching has minimum effect on the measured orientation of DNA, and the value of θ_0 is analytically known to be zero which has also been verified experimentally. As a result, the rotational relaxation time can be more accurately measured from experiments.

7.5.3 *Static and Dynamic Scalings vs Channel Height*

We have measured the diffusivity D, the longest rotational relaxation time τ_r, and the longest stretch relaxation time τ_s of λ-DNA in the 1.5×TBE buffer in slits with heights of 2 μm, 560 nm, 471 nm, 247 nm, 90 nm, 66 nm, and 32 nm. We also performed the same measurements in the TE buffer in the 247 nm, 90 nm, and 66 nm tall slits to examine the possibility of any specific effects on the scaling of these dynamic properties from the interactions between DNA and the boric acid in the TBE buffer [87].

Results of the dynamic properties of λ-DNA are summarized in Figure 7.7. Note that all the data have been corrected to correspond to a buffer viscosity of $\eta = 1\,\mathrm{cP}$ using equations $D(1\,\mathrm{cP}) = D\eta$ and $\tau(1\,\mathrm{cP}) = \tau/\eta$. The errors do not include systematic components which are assumed to

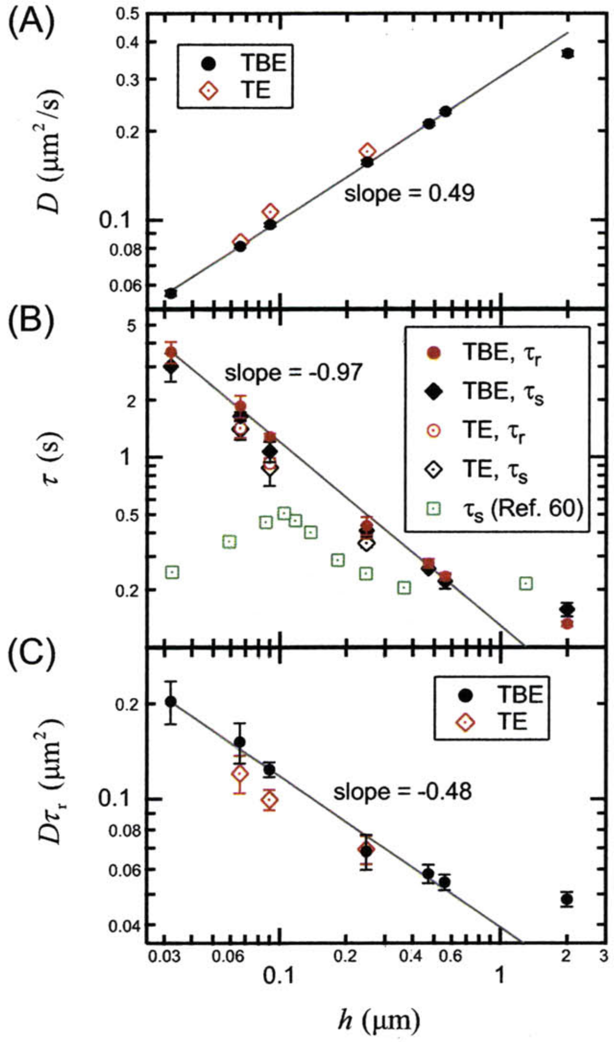

Fig. 7.7: *Dynamic properties of* λ*-DNA measured in both the 1.5*$\times$ *TBE buffer and the TE buffer as functions of the slit height* h*. All data have been corrected to a buffer viscosity of 1 cP. Solid lines represent power law fits (by minimizing the value of Chi-square) to the data (excluding the data for* $h = 2\,\mu m$*) from the TBE buffer. (A) Diffusivity. Error is less than the size of the symbols. Slope of the line is* 0.49 ± 0.01*. (B) The longest rotational relaxation time and stretch relaxation time. Solid line is a power law fit to the rotational relaxation time (for* $h < 1\,\mu m$*) in the TBE buffer. Slope of the line is* -0.97 ± 0.03*. Also shown are results of the stretch relaxation times reported by Bonthuis et al. [60]. (C) Product of the diffusivity and the rotational relaxation time. Slope of the line is* -0.48 ± 0.02*.*

be small as these measurements are less affected by the point spread function and photobleaching. Figure 7.7A shows the DNA diffusivity as a function of slit height. The diffusivity data from 560 nm to 32 nm tall slit measured in the 1.5×TBE buffer are well described by a single power law fit (by minimizing the value of Chi-square) with an exponent of 0.49 ± 0.01. Both the values of diffusivity and its scaling with respect to h are in quantitative agreement with previous studies [57, 61]. The diffusivities measured in the TE buffer display similar slope (0.50 ± 0.04 determined from the three data points) with h, although their values are consistently larger than these in the TBE buffer under the same slit height. We do not observe any abrupt change in the scaling of diffusivity as the slit height becomes smaller than 100 nm, in accord with the results of Strychalski et al. [61].

Figure 7.7B shows the rotational relaxation time and stretch relaxation time against slit height h. Results of the stretch relaxation time of λ-DNA reported by Bonthuis et al. [60] are also plotted for comparison [1]. The measured rotational relaxation time τ_r and stretch relaxation time τ_s agree well with each other in both buffers, and they all show similar slope versus h. Switching the experimental buffer from TBE to TE leads to a decrease in both τ_r and τ_s (although the errors still overlap). Consistent with the scaling of diffusivity, no sudden change in the scaling of either τ_s or τ_r is seen for $h < 100\,\mathrm{nm}$. A single power law relation suffices to characterize all the relaxation time data for $h < 1\,\mu\mathrm{m}$. The fitted scaling exponent is -0.97 ± 0.03 for τ_r and -0.94 ± 0.04 for τ_s in the TBE buffer, in quantitative agreement with the exponent of -0.92 ± 0.08 reported by Hsieh et al. [57] who measured τ_r of λ-DNA in nanoslits with height from 760 nm to 92 nm (in the de Gennes regime).

Finally we look at the scaling of $D\tau_r$, the product of diffusivity and rotational relaxation time. Although both D and τ_r depend on the drag coefficient of the chain ζ_{chain} (see Equation 7.4 and 7.5), their product is independent of ζ_{chain} and is only a function of chain size $D\tau_r \sim R^2$. Because both the diffusivity and rotational relaxation time can be more accurately determined from experiments than the in-plane radius of gyration, this quantity can be used as a better indicator of the DNA size. Figure 7.7C displays $D\tau_r$ as a function of h. It is seen that the scaling of $D\tau_r$ with h does not differ much between the two buffers. However, the values of $D\tau_r$ are smaller in the TE buffer, indicating that eliminating the boric acid from the buffer system reduces the size of DNA. This trend is in accord with the previous observations of larger diffusivity and shorter relaxation time in the TE buffer. As the two buffers bear similar ionic strength, the changes in these properties are most likely related to the interactions between DNA and the boric acid. A possible explanation for these differences is the higher charge density of DNA in the presence of boric acid [87] which can increase both the persistence length and effective width of DNA and thus alter the size and dynamic properties of the molecule toward the observed direction [58]. Nevertheless, the boric acid does not appear to have a strong effect on the scalings of DNA diffusivity, relaxation time, as well as their product with slit height.

The data of $D\tau_r$ from the TBE buffer also follow a single power law relation from $h = 560\,\mathrm{nm}$ to $h = 32\,\mathrm{nm}$ with a fitted slope of -0.48 ± 0.02. The same qualitative behavior is seen for the measured in-plane radius of gyration $R_{\parallel}$ (see Figure 7.4A). More importantly, the extracted scaling not only agrees with the blob theory prediction ($R^2 \sim h^{-0.5}$, Equation 7.2) but also supports the scaling proposed by Odijk [53] ($R^2 \sim h^{-0.5}$, Equation 7.7) for the deflection chain regime ($h < p$). We examine our experimental conditions to confirm that Equation 7.7 is valid in our case. We

---

[1] We note that Bonthuis et al. [60] referenced a previous study from our group [106] for the bulk relaxation of λ-DNA (0.2 s) which was in fact measured in a $2\,\mu\mathrm{m}$ tall channel, where $2R_{g,\text{bulk}}/h \sim 1$. This value is about twice the true bulk relaxaton time of λ-DNA in a 1 cP buffer (0.1 s) [143].

Table 7.1: *Summary of experimental conditions of several different studies. "BME" stands for β-mercaptoethanol and "Glox" stands for the anti-oxygen system of glucose, glucose oxidase and catalase.*

Study	Basepair to dye ratio	Buffer composition	Viscosity (cP, 22-23°C)	Ionic Strength (mM)
Current study	4:1	1.5×TBE, BME, and Glox	1.17	56.9
Hsieh et al. [57]	4:1	0.5×TBE, BME, and Glox	1.075	24.5
Balducci et al. [56]	4:1	0.5×TBE and BME	~1.1	24.5
Strychalski et al. [61]	5:1	5×TBE and BME	~1.35	155.1
Lin et al. [62]	4:1	0.5×TBE, 10 mM NaCl, BME, and Glox	~1.1	35

estimate the persistence length and effective width of the DNA to be $p \approx 54\,\mathrm{nm}$ (for unstained DNA) and $w \approx 6.6\,\mathrm{nm}$ in the 1.5×TBE buffer [58,132]. The condition $h \gg w$ is satisfied even in the thinnest slit (32 nm tall) investigated. Also, the excluded-volume parameter $Z \sim L_c w/ph > (22000\times 6.6)/(54\times 100) \gg 1$ for $h < 100\,\mathrm{nm}$, indicating the repulsive interactions between deflection segments are important. *Overall, no sharp transition from the moderate confinement to strong confinement was identified in any of the experimental results.*

7.5.4 Comparison with Previous Results

First we compare our data with those reported in several previous experimental studies [56,57,61,62]. We have re-analyzed the raw DNA images from Ref. [57] to calculate the in-plane radius of gyration $R_{\|}$ and the maximum extension X_{max}. The experimental conditions of these studies are summarized in Table 7.1.

The contour length of the DNA chain relies on the basepair to dye ratio in the staining process, while the persistence length and effective width of DNA are dependent on the buffer ionic strength I. In order to make quantitative comparisons of the data from the above studies, the effects of the different experimental conditions (i.e., staining ratio and buffer) must be taken into account. We correct the diffusivity and relaxation time data from different studies with Equation 7.4 and 7.5 so that the resulting data all correspond to the same experimental condition: basepair to dye ratio of 4:1, buffer viscosity of $\eta = 1\,\mathrm{cP}$, and buffer ionic strength of $I = 56.9\,\mathrm{mM}$.

We use the formula proposed by Dobrynin [144] to estimate the persistence length p

$$p = 46.1 + \frac{1.1915\,\mathrm{M}}{\sqrt{I}}\,\mathrm{nm} \tag{7.30}$$

The effective width w is calculated using Stigter's prediction [132]

$$w = \kappa^{-1}\left(0.7704 + \ln\frac{2\pi\nu_{\mathrm{eff}}^2}{k_B T \varepsilon\varepsilon_0 \kappa}\right) \tag{7.31}$$

where ν_{eff} is an effective DNA line charge, ε is the dielectric constant of water, ε_0 is the permittivity of free space, and κ is the inverse Debye screening length

$$\kappa^2 = \frac{2N_{\mathrm{A}}e^2I}{\varepsilon\varepsilon_0 k_{\mathrm{B}}T} \tag{7.32}$$

In the above equation, N_{A} is Avogadro's number, and e is the electronic charge.

Figure 7.8A and B show results of the corrected diffusivity and longest rotational relaxation time reported in different studies. It is clearly seen that our data yield quantitative agreement with those reported in Ref. after correcting the effects of different experimental conditions. On the other hand, the diffusivity data reported in Ref. [56] and [61] also show similar scaling with the slit height h but the absolute values are about 10% smaller than those from the current study and Ref. [57]. We believe this discrepancy is resulted from the presence of the anti-oxygen system (Glox) consisting of glucose, glucose oxidase, and catalase in the experimental buffers of the current study and Ref. [57], which was not used in Ref. [56] and [61]. The same phenomenon has been observed previously by Hsieh et al. [57].

Figure 7.81C and D show comparisons of the scaled ensemble average in-plane radius of gyration $\langle R_{\|}/R_{\|,\mathrm{bulk}}\rangle$ and the relative extension $\langle X_{\max}\rangle/L_c$ as functions of slit height h. We see again both our data of $\langle R_{\|}\rangle$ and $\langle X_{\max}\rangle$ match these determined from the raw DNA images of Ref. [57]. We have also plotted in Figure S1D the relative extensions of λ-DNA in nanoslits reported by Lin et al. [62]. Their data show a faster increase with decreasing h in the range of $200\,\mathrm{nm} < h < 1\,\mu\mathrm{m}$ and gradually slows down with further confinement. Although a change in the scaling of $\langle X_{\max}\rangle$ with h is observed in the data of Lin et al., the transition is not as sharp as that observed by Bonthuis et al. [60] and the extension still appears to increase with decreasing h for $h < 100\,\mathrm{nm}$. We also point out that the measurement of the DNA extension from image analysis is as well subject to significant bias introduced by both photobleaching and the point spread function of the optical system. Consequently, the extension data probably cannot yield an accurate scaling regarding the DNA size with slit height.

Now we compare our data with those reported by Bonthuis et al. [60]. We observe two major discrepancies regarding the DNA size and relaxation time between the current study and experiments performed by Bonthuis et al. for $30\,\mathrm{nm} < h < 400\,\mathrm{nm}$. First, the values of τ_{r} and τ_{s} determined from our experiments are significantly larger (more than a factor of 2) than the results of Bonthuis et al. after viscosity correction. We notice that the number of YOYO-1 dye molecules used to stain a single λ-DNA was different in the two studies: a base pair to dye ratio of 4:1 was used in the current study while Bonthuis et al. used a ratio of 6:1. Intercalating dyes such as YOYO-1 are known to affect both the structural and mechanical properties of DNA [145]. It is generally assumed that the contour length of the DNA increases linearly with the amount of bound YOYO-1 up to about 35% at a saturating dye concentration of 1 dye per 4 base pairs [97,98]. We thus estimate that the contour length of λ-DNA to be $\sim$ 10% longer in the current study than that in the study of Bonthuis et al. given the different staining ratio. For the persistence length of DNA, contradictory data exist regarding the effects of YOYO-1 binding. Several studies [146,147] used optical tweezers to probe the force-extension behavior of DNA and suggested that the intercalation of YOYO-1 significantly reduces the DNA persistence length. On the other hand, Günther et al. [148] recently measured the force-extension curves of DNA using magnetic tweezers and found the persistence length of DNA to be rather independent of the staining ratio. Günther et al. claimed to have exclusively measured the entropic forces from bending fluctuations by suppressing the additional YOYO-1 intercalation

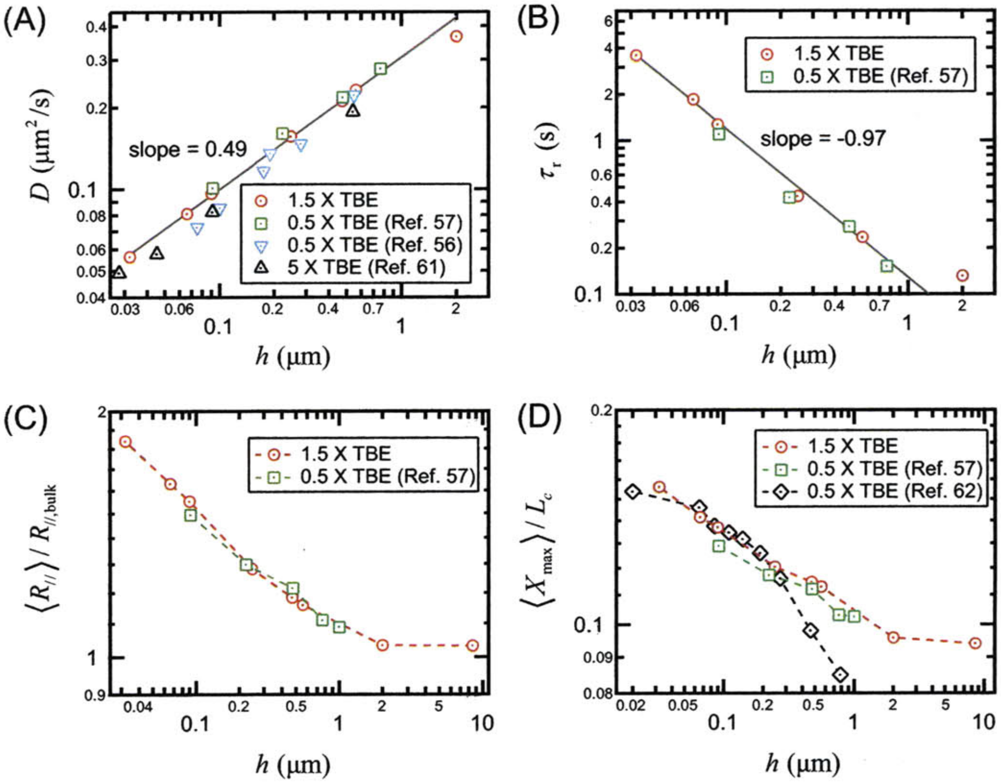

Fig. 7.8: *Comparison of the static and dynamic properties of λ-DNA in slit-like channels measured from the current and several previous studies. (A) Diffusivity measured in this study and reported in Ref. [56,57,61]. (B) Rotational relaxation time measured in this study and reported in Ref. [57]. All the diffusivity and relaxation time data plotted in (A) and (B) have been corrected to correspond to the same experimental condition: basepair to dye ratio of 4:1, buffer viscosity of 1 cP, and buffer ionic strength of* 56.9 *mM. (C) The scaled in-plane radius of gyration measured in this study and re-analyzed from raw data in Ref. [57]. (D) The fractional maximum extension measured in this study, re-analyzed from raw data in Ref. [57], and reported in Ref. [62].*

which can occur at large applied forces [146]. Nevertheless, considering the small difference in the staining ratios used in the two studies, we do not expect the persistence length of the DNA to vary dramatically. For instance, we estimate the persistence length of λ-DNA to be only ~20% smaller in the current study using the relation between the DNA contour length and persistence length reported in Table 1 of Ref. [147]. Note that the absolute values of the DNA persistence length in the current study and in the study of Bonthuis et al. are different from the data reported in Ref. [147] which were obtained in a buffer with a much higher ionic strength ($\mathrm{I} \approx 160\,\mathrm{mM}$). However, we assume the relative ratio of the persistence length as a function of the contour length does not depend strongly on the ionic strength. From the relation $\tau \sim L_c^{5/2} p^{5/6}$ (see Equation 7.5), the larger contour length and possibly smaller persistence length can make the relaxation time 5% higher in our experiments, which is far less than the difference seen in Figure 7.7B. In addition, the ionic strengths of both the TBE and TE buffer used in the current study are close to that used by Bonthuis et al. (10 mM Tris-EDTA, 50 mM NaCl, $\mathrm{I} \approx 56\,\mathrm{mM}$), the effects from the ionic strength induced changes in the persistence length and effective width of DNA [58] are thus expected to be minor. We do notice that Bonthuis et al. determined the stretch relaxation time by fitting the autocorrelation function C_s in the range of $1 > C_s > 0.1$. Since the decay of C_s at $C_s > 0.3$ still relies considerably on the higher order modes (see Figure 7.6), including this portion of the data in the fitting can significantly underestimate the longest relaxation time, which we suspect is one of the main reasons for the vastly different relaxation times for the same DNA substrate and similar slit height between the two studies.

Secondly, the scalings of both $R_{\|}$ and τ_s with h reported by Bonthuis et al. show a strong discontinuity at $h \approx 100\,\mathrm{nm}$ below which $R_{\|}$ becomes h-independent and τ_s starts to decrease with h. Our data do not shown these same trends. The stretch relaxation time measured by Bonthuis et al. is about the same for $h \approx 250\,\mathrm{nm}$ and $h = 33\,\mathrm{nm}$. In contrast, we show a more than 8-fold increase in both τ_r and τ_s when the slit height is reduced from 247 nm to 32 nm. The corresponding autocorrelation functions also decay dramatically slower in the 32 nm tall slit, as can be seen in Figure 7.6. Bonthuis et al. did not report the diffusivity of λ-DNA. The distinct behaviors of DNA in the strong confinement is unlikely caused by the nanochannels as they were all fabricated from the same substrate with similar methods in both studies. The discrepancy persists when we performed the experiments in the TE buffer which has very similar composition with the buffer used by Bonthuis et al.. It is possible that if the persistence length of the DNA in our experiments is significantly smaller than that in the study of Bonthuis et al., we might have not reached the regime where the slit height is much smaller than the persistence length and thus will not be able to observe the sharp transition. Given the fact that the transition was observed at $h \approx 100\,\mathrm{nm}$ by Bonthuis et al. while we did not see any evident change in the scalings of DNA size, diffusivity, and relaxation time with h even at $h = 32\,\mathrm{nm}$, the above postulation requires the persistence length of the DNA in our study to be at least$\sim (1 - 32/100) \approx 70\%$ smaller. However, as stated previously, we do not expect the persistence length of the DNA to be significantly different in the two studies. Currently the cause of the discrepancy still remains unclear.

7.6 Conclusion

In summary, we have experimentally investigated the equilibrium conformation and dynamics of single DNA molecules in slit-like nanochannels. We measured the in-plane radius of gyration, diffusivity and longest relaxation time of λ-DNA (48.5 kbp) as functions of the channel height using fluorescence microscopy. The measured in-plane radius of gyration $R_{||}$ displays a monotonic increase with decreasing channel height, in contrast to results from Bonthuis et al. [60]. We further performed Brownian dynamics simulations and demonstrated that the behavior of the in-plane radius of gyration and the 3D radius of gyration is different in weak confinement where $h \sim 2R_{g,\text{bulk}}$, as suggested by previous simulations [128]. This finding stresses the importance to distinguish the true 3D conformation of a polymer and its 2D projection when comparing theories with experimental results which are usually 2D measurements. We also examined the scalings of the DNA size, diffusivity, and longest relaxation time versus slit height in slit-like channels with height from 2 μm to 32 nm. All three properties show a single power law scaling with h, indicating the transition from the de Gennes regime to Odijk's deflection chain regime should be broad and gradual. The measured scalings of diffusivity and relaxation time agree quantitatively with previous studies [56,57,61], and the measured scaling of DNA size agrees with Odijk's recent scaling arguments [53]; namely that the h-dependence of the chain size does not change in the deflection chain regime. These results provide insight into the fundamental behavior of polymer under slit-like confinement and can be useful for the design of future processes aiming to utilize the capability of these ultra-thin devices to drastically alter the conformation and dynamics of polymer chains. Finally, we remark that all the nanoslits investigated in our experiments are much taller than both the Debye screening length ($\sim$ 1 nm) and the effective width of the DNA. It is possible that further decrease in channel height can lead to considerable interactions between the local ionic environment near the negatively charged channel wall and the DNA backbone, and thus induce other effects to DNA that are not considered in the current study.

CHAPTER 8

Conclusions and Outlook

The work presented in this thesis consists of two major topics: 1, designing micro- and nano-scale single molecule DNA stretching devices that can potentially serve as future platforms for gene mapping, and 2, experimentally investigating the fundamental physics of DNA conformation and dynamics in slit-like nanoconfinement. These two parts, however, are not independent studies but intrinsically related to each other. A comprehensive understanding of DNA behavior in confinement forms the essential fundamental basis for the design of devices aiming to exploit confinement to stretch DNA molecules, and the nanofluidic stretching devices also provide us with the unique opportunity to probe the non-equilibrium dynamics of confined DNA that have been rarely studied in the past. In this chapter, we briefly summarize the major findings of this work, comment on their impact, and suggest possible future directions.

In the aspect of device design, the general criteria we set for the stretching device are simple geometry, easy implementation, good compatibility with single molecule DNA mapping processes, and of course the ability to uniformly stretch DNA molecules within a sample ensemble. As these criteria stand, we pursue the use of an elongational electric field with a stagnation point generated in the center of a cross-slot or T channel to stretch DNA molecules. Since electric field scales well with small channel dimensions, we employ channels with height equal to or smaller than the natural size of the DNA molecules ($R_{g,\text{bulk}} \sim 1\,\mu\text{m}$) to keep the DNA always in focus. The presence of the stagnation point allows the possibility to first dynamically trap and then stretch a single DNA molecule. The trapping capability not only ensures that sufficient strain can be applied to the DNA to attain uniform extension within an ensemble of molecules, but also allows prolonged imaging time which is important for any mapping applications. As a proof-of-principle study, we first used a $2\,\mu$m tall, symmetric T channel to demonstrate stable trapping and stretching of single DNA molecules. We showed that stretching can occur even beyond the elongational region due to the two opposing uniform electric fields, and thus much longer DNA molecules can still be trapped and stretched with this device.

The second stretching device we developed is a full cross-slot channel with the incorporation of hyperbolically curved sidewalls for the intersection region. Since the shape of the sidewalls matches exactly the streamlines in a homogeneous elongational field, disruption to the electric field profile due to the channel walls is minimized and we can obtain a homogeneous planar elongational electric field with a stagnation point within the entire intersection region. We then used this device to perform the first detailed study of the effect of slit-like confinement on the steady-state extension of DNA as a function of strain rate. We showed that confinement can significantly reduce the strain rate required to achieve a certain extension by increasing the drag coefficient of the molecule through screening of long range intramolecular hydrodynamic interactions, and thus facilitate DNA stretching. More importantly, because the steric interactions between the polymer and the confining walls decrease as the polymer extends, we examined how these extension-dependent interactions manifest themselves during the stretching process. In particular, as the relaxation of the DNA molecule very near equilibrium and at higher extensions is best described by two different time constants, we characterized the role of each time constant to establish guidelines for the operation of the device. We identified the higher-extension relaxation time as the correct time scale governing the large change in extension with applied strain rate. We also showed preliminary data suggesting the low extension relaxation time to be only important in polymer rotation and small deviations from equilibrium. Since the two relaxation time constants can be dramatically different in strong confinement, naive application of unconfined theory without realizing the correct time scale to use would significantly mis-predict the strain rates required to deform DNA molecules.

Following the above study, we investigated in more details the low-extension behavior of a deforming polymer in slit-like confinement, specifically, the coil-stretch transition of single DNA molecules in a homogeneous planar elongational electric field. This problem has been extensively studied for unconfined DNA where the major focus is always on the extension-dependent drag coefficient due to dominating HI. Here the use of confinement creates a completely different scenario: the confinement significantly reduces the extension-dependence of the drag coefficient by screening long range HI, while introduces a strong extension-dependence into the DNA spring constant through steric interactions. We provided the first experimental demonstration that these confinement-induced changes strongly modify the coil-stretch transition of single DNA molecules. We observed a more gradual coil-stretch transition characterized by two distinct critical strain rates for DNA in confinement, different from the unconfined case where a single critical strain rate exists. We further developed a dumbbell model to extract an effective spring law from experimental relaxation data. Using the spring law and kinetic theory modeling, we successfully predicted a two-stage coil-stretch transition emerges in confinement, suggesting that the change in the coil-stretch transition is due to a modified spring law in confinement.

Finally, we carried out studies to characterize the equilibrium conformation and dynamics of single DNA in slit-like confinement. Although a large number of studies have been carried out in this field, currently open questions still remain regarding the equilibrium behavior of single DNA in both weak ($h \sim 2R_{g,\mathrm{bulk}}$) and strong ($h < p$) slitlike confinement, because existing studies show inconsistent results. Our intention is to provide more insight into these two regimes of confinement.

We used both experiments and simulations to demonstrate that the in-plane radius of gyration and the 3D radius of gyration of DNA behaves differently in weak confinement. This finding stresses the importance to distinguish the true 3D conformation of a polymer and its 2D projection when comparing theories with experimental results which are usually 2D measurements. In strong confinement, we did not identify any evident change in the scalings of equilibrium size, diffusivity, and longest relaxation time of the polymer with channel height from the de Gennes regime to the Odijk regime, in strong contrast to the results of Bonthuis et al. [60]. Although the cause of the discrepancy is not yet clear, we compared our experimental results to recent theories as well as experimental results reported previously, and found excellent agreement. The transition between the de Gennes and Odijk regimes in slit-like confinement currently still remains an open question, and our finding adds more experimental evidence to the side of a continuous transition between these two regimes.

As a whole, this thesis presents not only designs of single molecule DNA stretching devices that can be readily used for DNA mapping, but also a major step forward in the characterization of polymers in confinement. We hope to have set a strong fundamental foundation upon which future studies of polymeric behavior in confinement can build on. At the very least, we hope to have illustrated that polymer dynamics, especially deformed polymer dynamics, is nontrivial in confinement and the possibility of new time scales and length scales must be accepted. The ability to predict these effects and design devices to exploit them will greatly aid future single molecule analysis.

Appendix A

Appendices

A.1 T4 DNA Relaxation Time

The relaxation times of T4 DNA measured in chapter 6 (referred as new) are consistently larger than these reported in chapter 5 (referred as old) for the same channel heights. Values of the relaxation times for all three channels are summarized in Table A.1.

Table A.1: *Comparison of T4 DNA relaxation times measured in chapter 5 and chapter 6.*

h	Relaxation time (new) Temperature: 22°C	Relaxation time (old) Temperature: 25°C
2.0 μm	$\tau_{\mathrm{I}} = 1.9\,\mathrm{s}$	$\tau_{\mathrm{I}} = 1.5\,\mathrm{s}$
300 nm	$\tau_{\mathrm{I}} = 3.0\,\mathrm{s}$	$\tau_{\mathrm{I}} = 2.7\,\mathrm{s}$
	$\tau_{\mathrm{II}} = 6.4\,\mathrm{s}$	$\tau_{\mathrm{II}} = 5.4\,\mathrm{s}$
150 nm	$\tau_{\mathrm{I}} = 5.7\,\mathrm{s}$	$\tau_{\mathrm{I}} = 4.6\,\mathrm{s}$
	$\tau_{\mathrm{II}} = 21.2\,\mathrm{s}$	$\tau_{\mathrm{II}} = 18.3\,\mathrm{s}$

We believe the discrepancy results from both the different temperatures at which the experiments were performed (22°C for chapter 6 and 25°C for chapter 5) and the variations in the concentration of the YOYO-1 dye from Invitrogen. The experimental temperature affects the buffer viscosity η and the dye concentration determines the contour length L_c of the stained DNA. Both the higher-extension relaxation time τ_{I} and the low-extension relaxation time τ_{II} rely on η and L_c as suggested by previous studies [57,66]: $\tau_{\mathrm{I}} \sim \eta L_c^{2.2}$ and $\tau_{\mathrm{II}} \sim \eta L_c^{2.45}$. The buffer viscosity was determined using microrheology [149] to be $\eta = 1.08\,\mathrm{cP}$ at 22°C and $\eta = 1.02\,\mathrm{cP}$ at 25°C. We first remove the viscosity effects from the relaxation time data by calculating a scaled relaxation time $\tilde{\tau} = \tau\eta_{\mathrm{ref}}/\eta$, where the reference viscosity η_{ref} is chosen to be 1 cP. We then estimate the ratio of the contour length of T4 DNA used in chapter 6 and in chapter 5 from the scaling:

$$\frac{L_{c,\mathrm{new}}}{L_{c,\mathrm{old}}} = \left(\frac{\tilde{\tau}_{\mathrm{I,new}}}{\tilde{\tau}_{\mathrm{I,old}}}\right)^{1/2.2} = \left(\frac{\tilde{\tau}_{\mathrm{II,new}}}{\tilde{\tau}_{\mathrm{II,old}}}\right)^{1/2.45} \tag{A.1}$$

Results of the ratio corresponding to each set of relaxation time data are shown in the last column of Table A.2. The data suggest that the contour length of the T4 DNA used in this study is on average about 5% longer. From this difference in L_c, we further estimate that the concentration of the batch of YOYO-1 dye used in chapter 5 is about 18% lower than that used in chapter 6.

Table A.2: *Comparison of the T4 DNA relaxation times scaled to 1 cP.*

h	$\tilde{\tau}$ (new)	$\tilde{\tau}$ (old)	$\tilde{\tau}_{\mathrm{new}}/\tilde{\tau}_{\mathrm{old}}$	$L_{c,\mathrm{new}}/L_{c,\mathrm{old}}$
2.0 μm	$\tilde{\tau}_{\mathrm{I}} = 1.76\,\mathrm{s}$	$\tilde{\tau}_{\mathrm{I}} = 1.47\,\mathrm{s}$	1.20	1.09
300 nm	$\tilde{\tau}_{\mathrm{I}} = 2.78\,\mathrm{s}$	$\tilde{\tau}_{\mathrm{I}} = 2.65\,\mathrm{s}$	1.05	1.02
	$\tilde{\tau}_{\mathrm{II}} = 5.93\,\mathrm{s}$	$\tilde{\tau}_{\mathrm{II}} = 5.29\,\mathrm{s}$	1.12	1.05
150 nm	$\tilde{\tau}_{\mathrm{I}} = 5.28\,\mathrm{s}$	$\tilde{\tau}_{\mathrm{I}} = 4.51\,\mathrm{s}$	1.17	1.07
	$\tilde{\tau}_{\mathrm{II}} = 19.63\,\mathrm{s}$	$\tilde{\tau}_{\mathrm{II}} = 17.94\,\mathrm{s}$	1.09	1.04

A.2 Brownian Dynamics Simulations

We used a Brownian dynamics (BD) simulation method developed by Kim and Doyle [141] to compute the probability distribution function $P(X_{\max}|X)$. T4 DNA molecules were modeled as chains of N_{b} beads connected by $N_{\mathrm{s}} = (N_{\mathrm{b}} - 1)$ springs with equal length. We fixed the end-to-end distance R of the bead-spring chain and let the chain to sample all possible configurations under conditions with no background flows (or electric fields). For each channel height, we ran a series of simulations at varying values of R and measured the corresponding probability distribution of the maximum extension $R_{\max}$ which allows us to construct the function $P(X_{\max}|X)$. We note that this method provides an approximation of the probability distribution function $P(X_{\max}|X)$ because this quantity could change when the chains are placed in flows (or electric fields).

A.2.1 Bead-spring Chain Model

The equation of motion for the position $\mathbf{r}_i$ of the ith bead is:

$$\frac{d\mathbf{r}_i}{dt} = \frac{1}{\zeta_{\mathrm{b}}}\left[\mathbf{F}_i^{\mathrm{B}}(t) + \mathbf{F}_i^{\mathrm{S}}(t) + \mathbf{F}_i^{\mathrm{EV}}(t) + \mathbf{F}_i^{\mathrm{W}}(t) + \mathbf{F}_i^{\mathrm{EE}}(t)\right] \tag{A.2}$$

where ζ_b is the bead drag coefficient, $\mathbf{F}_i^\mathrm{B}$ is the Brownian force, $\mathbf{F}_i^\mathrm{S}$ is the total spring force felt by the bead, $\mathbf{F}_i^\mathrm{EV}$ is the intrachain excluded volume force due to nearby beads, $\mathbf{F}_i^\mathrm{W}$ represents the interaction of the bead with the channel walls, and $\mathbf{F}_i^\mathrm{EE}$ represents the interaction between the end beads to enforce a certain end-to-end distance. We have neglected intrachain hydrodynamic interactions (HI) as the DNA molecules are placed in channels with height smaller than the bulk radius of gyration of the DNA [56]. We nondimensionalize the variables as follows:

$$\widehat{\mathbf{r}} = \frac{\mathbf{r}}{l_\mathrm{s}}, \quad \widehat{t} = \frac{t}{\zeta_\mathrm{b} l_\mathrm{s}^2 / k_\mathrm{B}T} \tag{A.3}$$

where $\mathbf{r}$ is position, l_s is the maximum extension of a single spring ($l_\mathrm{s} = L_c/N_\mathrm{s}$) and t is time. We nondimensionalize the forces $\mathbf{F}$ as follows:

$$\widehat{\mathbf{F}}\left(\widehat{\mathbf{r}}\right) = \frac{\mathbf{F}}{k_\mathrm{B}T/l_\mathrm{s}} \tag{A.4}$$

This leads to the dimensionless form of Equation A.2:

$$\frac{d\widehat{\mathbf{r}}_i}{d\widehat{t}} = \widehat{\mathbf{F}}_i^\mathrm{B} + \widehat{\mathbf{F}}_i^\mathrm{S} + \widehat{\mathbf{F}}_i^\mathrm{EV} + \widehat{\mathbf{F}}_i^\mathrm{W} + \widehat{\mathbf{F}}_i^\mathrm{EE} \tag{A.5}$$

The dimensionless Brownian force is given by:

$$\widehat{\mathbf{F}}_i^\mathrm{B} = \sqrt{\frac{24}{\Delta\widehat{t}}}\,(\mathbf{r}_n)_i \tag{A.6}$$

where $\Delta\widehat{t}$ is the dimensionless time step and $(\mathbf{r}_n)_i$ are uniform random numbers such that each component $(\mathbf{r}_n)_i^j \in [-1/2, 1/2]$, where j denotes the coordinate x, y, or z. The net non-dimensional spring force on the ith bead is:

$$\widehat{\mathbf{F}}_i^\mathrm{S} = \begin{cases} \widehat{\mathbf{f}}_{i,2}^\mathrm{s}, & i = 1 \\ \widehat{\mathbf{f}}_{i,i+1}^\mathrm{s} + \widehat{\mathbf{f}}_{i,i-1}^\mathrm{s}, & 1 < i < N_\mathrm{b} \\ \widehat{\mathbf{f}}_{i,N_\mathrm{b}-1}^\mathrm{s}, & i = N_\mathrm{b} \end{cases} \tag{A.7}$$

where $\widehat{\mathbf{f}}_{i,j}^\mathrm{s}$ is the force of the spring connecting the ith and jth beads given by a modified Marko-Siggia spring force law [76, 150]:

$$\widehat{\mathbf{f}}_{i,j}^\mathrm{s} = \frac{v}{\lambda}\left[\widehat{r}_{j,i} - \frac{1}{4} + \frac{1}{4\left(1 - \widehat{r}_{j,i}\right)^2}\right]\frac{\widehat{\mathbf{r}}_j - \widehat{\mathbf{r}}_i}{\widehat{r}_{j,i}} \tag{A.8}$$

where λ is the ratio of the effective persistence length to the true persistence length ($\lambda = l_\mathrm{eff}/l_\mathrm{p}$), v is the number of true persistence lengths represented by each spring ($v = l_\mathrm{s}/l_\mathrm{p}$), and $\widehat{r}_{j,i}$ is given by $\widehat{r}_{j,i} = |\widehat{\mathbf{r}}_j - \widehat{\mathbf{r}}_j|$. The intrachain excluded volume force $\widehat{\mathbf{F}}_i^\mathrm{EV}$ is modeled with the soft potential used by Jendrejack et al. [139]:

$$\widehat{\mathbf{F}}_i^{\mathrm{EV}} = -\sum_{\substack{j=1 \\ j\neq i}}^{N_\mathrm{b}} \frac{9}{2}\widehat{\nu}^{\mathrm{ev}} \left(\frac{3}{4\sqrt{\pi}}\right)^3 \upsilon^{9/2} \exp\left[-\frac{9}{4}\upsilon \widehat{r}_{ij}^2\right] \widehat{\mathbf{r}}_{ji} \tag{A.9}$$

where $\widehat{\nu}^{\mathrm{ev}} = \nu^{\mathrm{ev}}/l_\mathrm{s}^3$ is the dimensionless form of the excluded volume parameter ν^{ev}. The interactions between a bead and the walls represented by $\widehat{\mathbf{F}}_i^{\mathrm{W}}$ are resolved using a modified Heyes-Melrose algorithm [140, 141]. Whenever a bead moves outside the channel domain during a time step, it is moved to the nearest point on the domain boundary before commencing the next time step:

$$\Delta\widehat{\mathbf{r}}_i^{\mathrm{HM}} = \Delta\mathbf{p}_i H\left(\Delta p_i\right) \tag{A.10}$$

where $\Delta\widehat{\mathbf{r}}_i^{\mathrm{HM}}$ is the displacement vector due to the Heyes-Melrose algorithm, $\Delta\mathbf{p}_i$ is the vector pointing from the bead outside the domain to the nearest boundary point, and the Heaviside step function $H\left(\Delta p_i\right)$ restricts the application of the algorithm to only the beads that have penetrated the domain boundaries. Finally, the force $\mathbf{F}_i^{\mathrm{EE}}$ enforces a constant end-to-end distance R at the end of each time step by equally moving the two end beads at a distance

$$\Delta\widehat{\mathbf{r}}_1 = -\Delta\widehat{\mathbf{r}}_{N_\mathrm{b}} = \frac{1}{2}\left(1 - \frac{R}{\widehat{r}_{N_\mathrm{b},1}}\right)\left(\widehat{\mathbf{r}}_{N_\mathrm{b}} - \widehat{\mathbf{r}}_1\right) \tag{A.11}$$

A.2.2 Parameters

We used $N_\mathrm{b} = 128$ beads to model T4 DNA and the corresponding λ was set to be 1.89. For each channel height, we fit the excluded volume parameter such that the simulation matches the experimental equilibrium size distribution (see Figure A.1), giving: $\nu^{\mathrm{ev}} = 4.0 \times 10^{-4}\,\mu\mathrm{m}^3$ for the $2\,\mu$m tall channel, $\nu^{\mathrm{ev}} = 5.0 \times 10^{-4}\,\mu\mathrm{m}^3$ for the 300 nm tall channel, and $\nu^{\mathrm{ev}} = 1.13 \times 10^{-3}\,\mu\mathrm{m}^3$ for the 150 nm tall channel. We used a time step of $\Delta\hat{t} = 2.5 \times 10^{-3}$ in the simulations for all three channel heights. In each simulation, a bead-spring chain was initially placed in the center of the channel with the beads equally spaced in a linear manner such that the end-to-end distance R is equal to a certain value of interest. After an initial equilibration period, the instantaneous maximum extension R_{max} was periodically recorded for hundreds of relaxation times.

A.2.3 Results

Figure A.2 shows results of the distribution of the maximum extension at various values of dimensionless end-to-end distance (X) for chains in the 150 nm tall channel. At small values of X, the distribution of X_{max} is approximately gaussian. As the end-to-end distance increases, we observe the formation of a spike at the point $X_{\mathrm{max}} = X$. Results for the other two channel heights show qualitatively similar behavior. We fit the numerical data obtained from the Brownian dynamics simulation to the following function in order to estimate the probability $P(X_{\mathrm{max}}|X)$ at any given X:

$$P(X_{\mathrm{max}}|X) = \begin{cases} K_2 \exp\left[-\dfrac{(X_{\mathrm{max}} - X_0)^2}{w^2}\right], & X_{\mathrm{max}} > X \\ K_1\delta(X_{\mathrm{max}} - X), & X_{\mathrm{max}} = X \\ 0, & X_{\mathrm{max}} < X \end{cases} \tag{A.12}$$

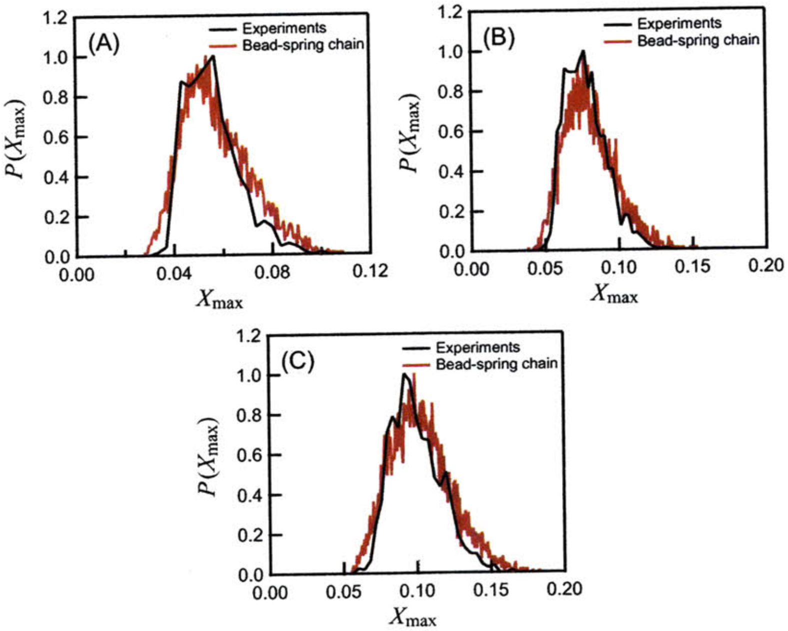

Fig. A.1: *Comparison of the probability distribution of the equilibrium maximum extension between experiments and the BD simulation of the bead-spring chain for the 2 μm tall channel (A), 300 nm tall channel (B), and the 150 nm tall channel (C).*

where δ is the Dirac delta function, X_0, w, and K_1 are the three independent fitting parameters. The value of K_2 is determined from the equation $\int_X^1 P(X_{\max}|X)dX_{\max} = 1 - K_1$, giving

$$K_2 = \frac{1 - K_1}{\int_X^1 \exp\left[-(X_{\max} - X_0)^2/w^2\right] dX_{\max}} \tag{A.13}$$

Results of the fitting are shown as the black dashed line in each subplots of Figure A.2. Quantitative agreement between the simulation data and the fit is observed. Figure A.3 displays the values of the three fitting parameters (X_0, w, and K_1) as a function of X for all three channel heights. These data determined from the simulation provide the master curves that can be used to estimate the probability distribution of $X_{\max}$ at any values of X. Consequently, the probability distribution of X predicted by the dumbbell model can be mapped into the maximum extension distribution

$$P(X_{\max}) = \int_0^1 P(X_{\max}|X)dX \int_{-\pi/2}^{\pi/2} \psi(X, \theta) X d\theta \tag{A.14}$$

Figure A.4 shows the average values and the standard deviations of the end-to-end distance X calculated from the dumbbell model as well as the same quantities for the maximum extension obtained from the mapping using Equation A.14 as comparisons. It is seen that at large De_I the behaviors of the end-to-end distance and the maximum extension are almost identical. This superposition between the two curves is due to the fact that the molecule becomes highly extended and thus the distributions of X and $X_{\max}$ does not differ significantly. However, at lower values of De_I, clear differences are observed: the end-to-end distance possesses a lower average and wider distribution (giving a larger standard deviation). In particular, the magnitude of the first peak in the standard deviation plot is significantly larger for the end-to-end distances. We therefore argue that the mapping from $P(X)$ to $P(X_{\max})$ is important in order to compare the dumbbell model predictions to experimental data.

A.3 Dumbbell Model with Extension-dependent Drag Coefficient

As noted in the article, the magnitude of the peak in the standard deviation of the fractional extension for the $2\,\mu$m tall channel is significantly lower than that for the same DNA molecule in bulk elongational flow reported by Gerashchenko and Steinberg [67]. We use a dumbbell model with extension-dependent drag coefficient to demonstrate that a very possible reason for this disparity is the much stronger extension-dependence of the drag coefficient of DNA in bulk due to dominant intramolecular hydrodynamic interactions (HI). We start with the steady-state diffusion equation written as

$$-\frac{\partial}{\partial \mathbf{R}} \cdot \psi \left(\nabla \mathbf{v} \cdot \mathbf{R} - \frac{2k_\mathrm{B}T}{\zeta} \frac{\partial}{\partial \mathbf{R}} \ln \psi + \frac{2}{\zeta} \mathbf{F}_\mathrm{S} \right) = 0 \tag{A.15}$$

where $\mathbf{R}$ is the dumbbell end-to-end vector, ψ is the probability density function of $\mathbf{R}$, $\mathbf{v}$ is the flow velocity, $\mathbf{F}_\mathrm{S}$ is the elastic spring force, and ζ is the bead drag coefficient which varies with the dumbbell end-to-end distance. In a homogeneous planar elongational flow (i.e., $v_x = \dot{\varepsilon} x$, $v_y = -\dot{\varepsilon} y$, $v_z = 0$), the analytical solution to Equation A.15 can be found when the dumbbell is completely aligned with the axis of elongation (x-axis) [29]. In this case the dumbbell end-to-end distance

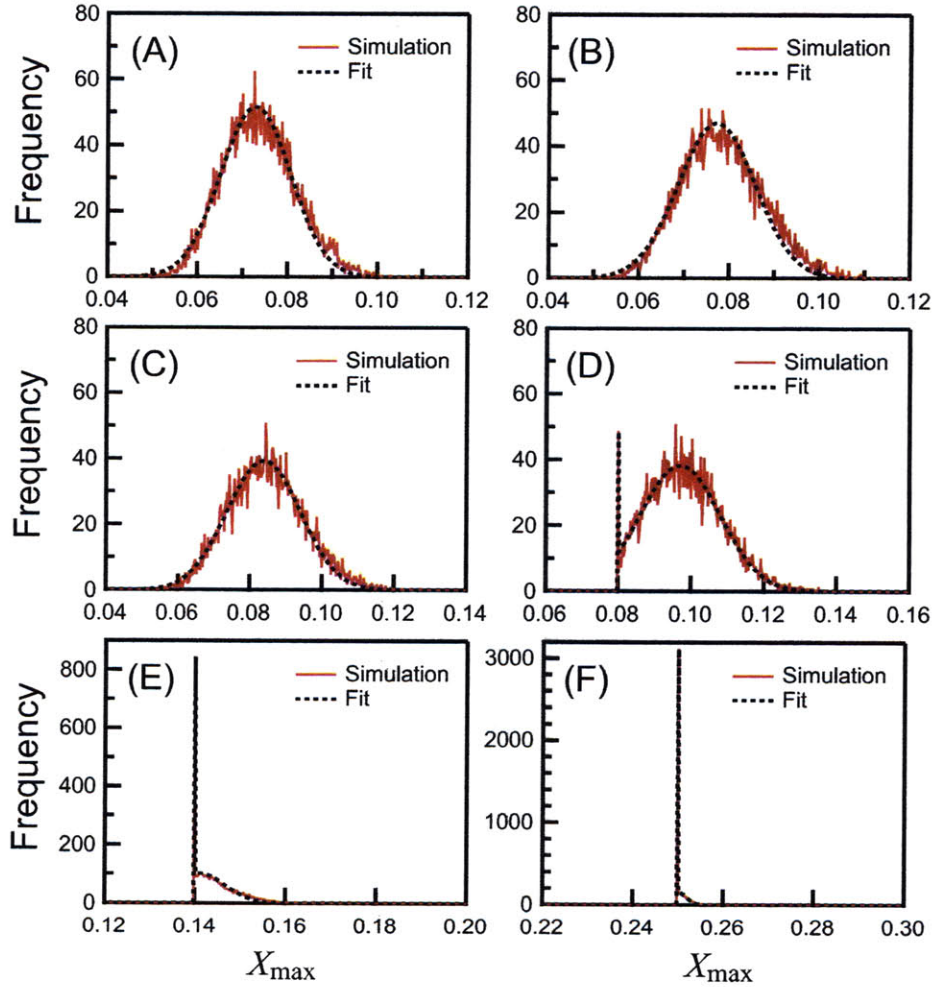

Fig. A.2: *Histograms of the the maximum extension distribution of the bead-spring chain at various values of end-to-end distance for the 150 nm tall channel case. The data in each plot correspond to a end-to-end distance of* $X = 0.01$ *(A),* $X = 0.03$ *(B),* $X = 0.05$ *(C),* $X = 0.08$ *(D),* $X = 0.16$ *(E),* $X = 0.25$ *(F). Also shown is the fit to the simulation data using Equation A.12.*

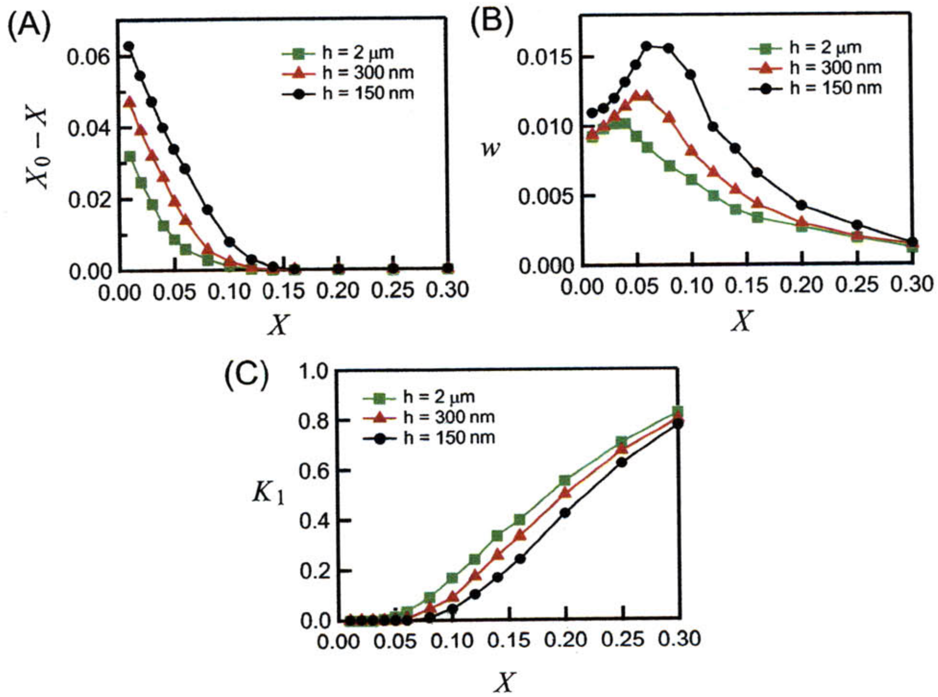

Fig. A.3: *Values of the three fitting parameters in Equation A.12 as a function of the dimensionless end-to-end distance X determined from simulation data. Results for all three channel heights are shown.*

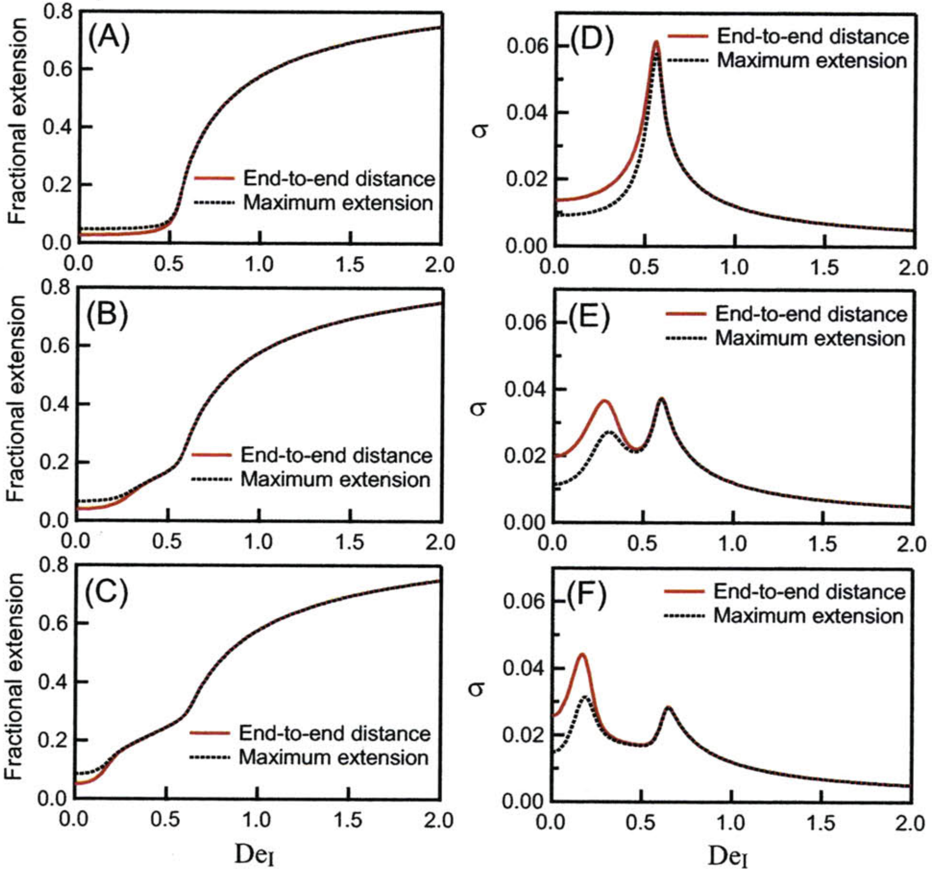

Fig. A.4: *(A-C) Comparison between the dumbbell model prediction of the average dumbbell end-to-end distance and the average maximum extension (obtained by transforming $P(X)$ to $P(X_{\max})$ using $P(X_{\max}|X)$) for the 2 μm tall channel (A), 300 nm tall channel (B), and the 150 nm tall channel (C). (D-F) Comparison between the dumbbell model prediction of the standard deviation of the end-to-end distance and that of the maximum extension for the 2 μm tall channel (D), 300 nm tall channel (E), and the 150 nm tall channel (F).*

$R = |\mathbf{R}| = R_x$ and the corresponding probability density function ψ is given by:

$$\psi(R) = K \exp\left\{\frac{1}{k_B T} \int_R \left[\frac{1}{2}\zeta(R)\dot{\varepsilon}R + F_S(R)\right] dR\right\} \tag{A.16}$$

where K is the normalization constant which satisfies the condition $\int_R \psi dR = 1$.

In the presence of HI, a coiled molecule at equilibrium has a smaller drag coefficient relative to a long rod-like configuration (i.e., when the molecule is highly stretched). For simplicity we assume that the drag coefficient increases linearly from the equilibrium coil to a fully extended state

$$\frac{\zeta(R)}{\zeta_{\text{coil}}} = 1 + \left(\frac{\zeta_{\text{extend}}}{\zeta_{\text{coil}}} - 1\right)\frac{R}{L_c} \tag{A.17}$$

where L_c is the contour length of the dumbbell spring, ζ_{extend} is the drag coefficient of the completely stretched molecule, and ζ_{coil} is the drag coefficient of the coiled molecule at equilibrium. We apply the wormlike chain force law for the dumbbell spring force, $F_S = -H_{\text{bulk}} R f(R/L_c)$, where the dimensionless function f is given by

$$f\left(\frac{R}{L_c}\right) = \frac{L_c}{6R}\left[\left(1 - \frac{R}{L_c}\right)^{-2} + \frac{4R}{L_c} - 1\right] \tag{A.18}$$

We next define a fractional dumbbell end-to-end distance $X = R/L_c$ and a Deborah number $\text{De} = \dot{\varepsilon}\zeta_{\text{coil}}/4H_{\text{bulk}}$. Equation A.16 can now be rewritten in dimensionless form as

$$\psi(X) = K \exp\left\{-3N \int_0^X \left\{x f(x) - 2\text{De}\left[1 + \left(\frac{\zeta_{\text{extend}}}{\zeta_{\text{coil}}} - 1\right)x\right]x\right\} dx\right\} \tag{A.19}$$

Equation A.19 allows us to calculate the average steady-state fractional end-to-end distance and the standard deviation of the end-to-end distance at a given Deborah number:

$$\langle X \rangle = \int_0^1 X\psi(X)dX \tag{A.20}$$

$$\sigma = \sqrt{\int_0^1 (X - \langle X \rangle)^2 \psi(X)dX} \tag{A.21}$$

Figure A.5 shows results of $\langle X \rangle$ and σ as functions of De for dumbbells with both constant drag coefficient ($\zeta_{\text{extend}}/\zeta_{\text{coil}} = 1$) and extension-dependent drag coefficient ($\zeta_{\text{extend}}/\zeta_{\text{coil}} = 2.1$). The ratio of the drag coefficient for the case of extension-dependent drag coefficient is chosen to represent T4 DNA in bulk elongational flow [67]. Results for dumbbell with a constant drag coefficient agree very well with those in the article calculated without the assumption of complete alignment with the x-axis (data not shown). It is clearly seen that the incorporation of extension-dependence into the drag coefficient produces a much sharper coil-stretch transition as well as a higher peak in the standard deviation plot. The magnitude of the peak in σ for T4 DNA in bulk is about 1.9-fold larger than that for the case of constant drag coefficient. These calculations support our postulation that the dominant hydrodynamic interactions for DNA molecules in bulk might be responsible for the disparity between our results for the 2 μm tall channel and those reported in

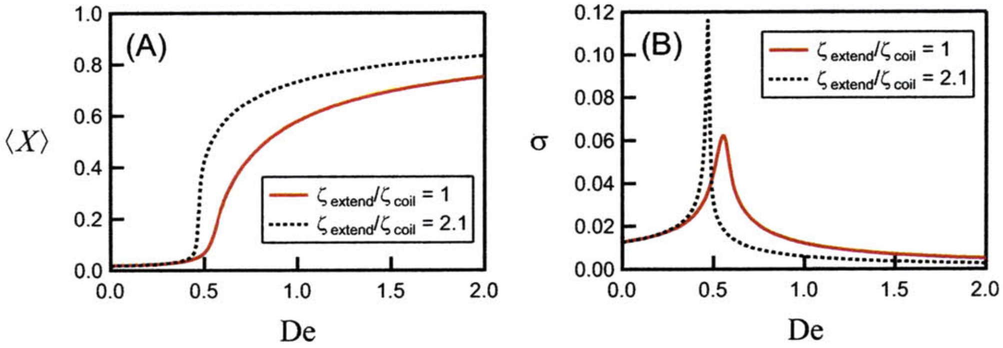

Fig. A.5: *Average steady-state fractional end-to-end distance (A) and the standard deviation of the fractional end-to-end distance (B) as functions of the Deborah number calculated using Equation A.20 and Equation A.21, respectively. Two traces are shown in each plot, one for the constant drag coefficient case* ($\zeta_{\text{extend}}/\zeta_{\text{coil}} = 1$) *and one for T4 DNA in bulk elongational flow* ($\zeta_{\text{extend}}/\zeta_{\text{coil}} = 2.1$)*.*

Ref. [67].

Bibliography

[1] Lander, E. S.; Linton, L. M.; Birren, B.; Nusbaum, C.; Zody, M. C.; Baldwin, J.; Devon, K.; Dewar, K.; Doyle, M.; FitzHugh, W.; Funke, R.; Gage, D.; Harris, K.; Heaford, A.; Howland, J.; Kann, L.; Lehoczky, J.; LeVine, R.; McEwan, P.; McKernan, K.; Meldrim, J.; Mesirov, J. P.; Miranda, C.; Morris, W.; Naylor, J.; Raymond, C.; Rosetti, M.; Santos, R.; Sheridan, A.; Sougnez, C.; Stange-Thomann, N.; Stojanovic, N.; Subramanian, A.; Wyman, D.; Rogers, J.; Sulston, J.; Ainscough, R.; Beck, S.; Bentley, D.; Burton, J.; Clee, C.; Carter, N.; Coulson, A.; Deadman, R.; Deloukas, P.; Dunham, A.; Dunham, I.; Durbin, R.; French, L.; Grafham, D.; Gregory, S.; Hubbard, T.; Humphray, S.; Hunt, A.; Jones, M.; Lloyd, C.; McMurray, A.; Matthews, L.; Mercer, S.; Milne, S.; Mullikin, J. C.; Mungall, A.; Plumb, R.; Ross, M.; Shownkeen, R.; Sims, S.; Waterston, R. H.; Wilson, R. K.; Hillier, L. W.; McPherson, J. D.; Marra, M. A.; Mardis, E. R.; Fulton, L. A.; Chinwalla, A. T.; Pepin, K. H.; Gish, W. R.; Chissoe, S. L.; Wendl, M. C.; Delehaunty, K. D.; Miner, T. L.; Delehaunty, A.; Kramer, J. B.; Cook, L. L.; Fulton, R. S.; Johnson, D. L.; Minx, P. J.; Clifton, S. W.; Hawkins, T.; Branscomb, E.; Predki, P.; Richardson, P.; Wenning, S.; Slezak, T.; Doggett, N.; Cheng, J. F.; Olsen, A.; Lucas, S.; Elkin, C.; Uberbacher, E.; Frazier, M.; Gibbs, R. A.; Muzny, D. M.; Scherer, S. E.; Bouck, J. B.; Sodergren, E. J.; Worley, K. C.; Rives, C. M.; Gorrell, J. H.; Metzker, M. L.; Naylor, S. L.; Kucherlapati, R. S.; Nelson, D. L.; Weinstock, G. M.; Sakaki, Y.; Fujiyama, A.; Hattori, M.; Yada, T.; Toyoda, A.; Itoh, T.; Kawagoe, C.; Watanabe, H.; Totoki, Y.; Taylor, T.; Weissenbach, J.; Heilig, R.; Saurin, W.; Artiguenave, F.; Brottier,

P.; Bruls, T.; Pelletier, E.; Robert, C.; Wincker, P.; Rosenthal, A.; Platzer, M.; Nyakatura, G.; Taudien, S.; Rump, A.; Yang, H. M.; Yu, J.; Wang, J.; Huang, G. Y.; Gu, J.; Hood, L.; Rowen, L.; Madan, A.; Qin, S. Z.; Davis, R. W.; Federspiel, N. A.; Abola, A. P.; Proctor, M. J.; Myers, R. M.; Schmutz, J.; Dickson, M.; Grimwood, J.; Cox, D. R.; Olson, M. V.; Kaul, R.; Raymond, C.; Shimizu, N.; Kawasaki, K.; Minoshima, S.; Evans, G. A.; Athanasiou, M.; Schultz, R.; Roe, B. A.; Chen, F.; Pan, H. Q.; Ramser, J.; Lehrach, H.; Reinhardt, R.; McCombie, W. R.; de la Bastide, M.; Dedhia, N.; Blocker, H.; Hornischer, K.; Nordsiek, G.; Agarwala, R.; Aravind, L.; Bailey, J. A.; Bateman, A.; Batzoglou, S.; Birney, E.; Bork, P.; Brown, D. G.; Burge, C. B.; Cerutti, L.; Chen, H. C.; Church, D.; Clamp, M.; Copley, R. R.; Doerks, T.; Eddy, S. R.; Eichler, E. E.; Furey, T. S.; Galagan, J.; Gilbert, J. G. R.; Harmon, C.; Hayashizaki, Y.; Haussler, D.; Hermjakob, H.; Hokamp, K.; Jang, W. H.; Johnson, L. S.; Jones, T. A.; Kasif, S.; Kaspryzk, A.; Kennedy, S.; Kent, W. J.; Kitts, P.; Koonin, E. V.; Korf, I.; Kulp, D.; Lancet, D.; Lowe, T. M.; McLysaght, A.; Mikkelsen, T.; Moran, J. V.; Mulder, N.; Pollara, V. J.; Ponting, C. P.; Schuler, G.; Schultz, J. R.; Slater, G.; Smit, A. F. A.; Stupka, E.; Szustakowki, J.; Thierry-Mieg, D.; Thierry-Mieg, J.; Wagner, L.; Wallis, J.; Wheeler, R.; Williams, A.; Wolf, Y. I.; Wolfe, K. H.; Yang, S. P.; Yeh, R. F.; Collins, F.; Guyer, M. S.; Peterson, J.; Felsenfeld, A.; Wetterstrand, K. A.; Patrinos, A.; Morgan, M. J.; Conso, I. H. G. S., *Nature* **2001**, *409*, 860.

[2] Mikkelsen, T. S.; Hillier, L. W.; Eichler, E. E.; Zody, M. C.; Jaffe, D. B.; Yang, S. P.; Enard, W.; Hellmann, I.; Lindblad-Toh, K.; Altheide, T. K.; Archidiacono, N.; Bork, P.; Butler, J.; Chang, J. L.; Cheng, Z.; Chinwalla, A. T.; deJong, P.; Delehaunty, K. D.; Fronick, C. C.; Fulton, L. L.; Gilad, Y.; Glusman, G.; Gnerre, S.; Graves, T. A.; Hayakawa, T.; Hayden, K. E.; Huang, X. Q.; Ji, H. K.; Kent, W. J.; King, M. C.; Kulbokas, E. J.; Lee, M. K.; Liu, G.; Lopez-Otin, C.; Makova, K. D.; Man, O.; Mardis, E. R.; Mauceli, E.; Miner, T. L.; Nash, W. E.; Nelson, J. O.; Paabo, S.; Patterson, N. J.; Pohl, C. S.; Pollard, K. S.; Prufer, K.; Puente, X. S.; Reich, D.; Rocchi, M.; Rosenbloom, K.; Ruvolo, M.; Richter, D. J.; Schaffner, S. F.; Smit, A. F. A.; Smith, S. M.; Suyama, M.; Taylor, J.; Torrents, D.; Tuzun, E.; Varki, A.; Velasco, G.; Ventura, M.; Wallis, J. W.; Wendl, M. C.; Wilson, R. K.; Lander, E. S.; Waterston, R. H.; Consortium, C. S. A., *Nature* **2005**, *437*, 69.

[3] Lindblad-Toh, K.; Wade, C. M.; Mikkelsen, T. S.; Karlsson, E. K.; Jaffe, D. B.; Kamal, M.; Clamp, M.; Chang, J. L.; Kulbokas, E. J.; Zody, M. C.; Mauceli, E.; Xie, X. H.; Breen, M.; Wayne, R. K.; Ostrander, E. A.; Ponting, C. P.; Galibert, F.; Smith, D. R.; deJong, P. J.; Kirkness, E.; Alvarez, P.; Biagi, T.; Brockman, W.; Butler, J.; Chin, C. W.; Cook, A.; Cuff, J.; Daly, M. J.; DeCaprio, D.; Gnerre, S.; Grabherr, M.; Kellis, M.; Kleber, M.; Bardeleben, C.; Goodstadt, L.; Heger, A.; Hitte, C.; Kim, L.; Koepfli, K. P.; Parker, H. G.; Pollinger, J. P.; Searle, S. M. J.; Sutter, N. B.; Thomas, R.; Webber, C.; Lander, E. S.; Plat, B. I. G. S., *Nature* **2005**, *438*, 803.

[4] Chan, E. Y., *Mutat. Res. Fundam. Mol. Mech. Mugag.* **2005**, *573*, 13.

[5] Olive, D. M.; Bean, P., *J. Clin. Microbiol.* **1999**, *37*, 1661.

[6] Brown, T. A., *Genomes*, John Wiley & Sons, Inc., New York 1999.

[7] Lai, E.; Birren, B. W.; Clark, S. M.; Simon, M. I.; Hood, L., *Biotechniques* **1989**, *7*, 34.

[8] Schwartz, D. C.; Li, X. J.; Hernandez, L. I.; Ramnarain, S. P.; Huff, E. J.; Wang, Y. K., *Science* **1993**, *262*, 110.

[9] Samad, A. H.; Cai, W. W.; Hu, X. H.; Irvin, B.; Jing, J. P.; Reed, J.; Meng, X.; Huang, J.; Huff, E.; Porter, B.; Shenkar, A.; Anantharaman, T.; Mishra, B.; Clarke, V.; Dimalanta, E.; Edington, J.; Hiort, C.; Rabbah, R.; Skiada, J.; Schwartz, D. C., *Nature* **1995**, *378*, 516.

[10] Taylor, J. R.; Fang, M. M.; Nie, S. M., *Anal. Chem.* **2000**, *72*, 1979.

[11] Chan, E. Y.; Goncalves, N. M.; Haeusler, R. A.; Hatch, A. J.; Larson, J. W.; Maletta, A. M.; Yantz, G. R.; Carstea, E. D.; Fuchs, M.; Wong, G. G.; Gullans, S. R.; Gilmanshin, R., *Genome Res.* **2004**, *14*, 1137.

[12] Phillips, K. M.; Larson, J. W.; Yantz, G. R.; D'Antoni, C. M.; Gallo, M. V.; Gillis, K. A.; Goncalves, N. M.; Neely, L. A.; Gullans, S. R.; Gilmanshin, R., *Nucleic Acids Res.* **2005**, *33*, 5829.

[13] Riehn, R.; Lu, M. C.; Wang, Y. M.; Lim, S. F.; Cox, E. C.; Austin, R. H., *Proc. Natl. Acad. Sci. U.S.A.* **2005**, *102*, 10012.

[14] Chan, T. F.; Ha, C.; Phong, A.; Cai, D.; Wan, E.; Leung, L.; Kwok, P. Y.; Xiao, M., *Nucleic Acids Res.* **2006**, *34*, e113.

[15] Xiao, M.; Phong, A.; Ha, C.; Chan, T. F.; Cai, D. M.; Leung, L.; Wan, E.; Kistler, A. L.; DeRisi, J. L.; Selvin, P. R.; Kwok, P. Y., *Nucleic Acids Res.* **2007**, *35*, e16.

[16] Jo, K.; Dhingra, D. M.; Odijk, T.; de Pablo, J. J.; Graham, M. D.; Runnheim, R.; Forrest, D.; Schwartz, D. C., *Proc. Natl. Acad. Sci. U.S.A.* **2007**, *104*, 2673.

[17] Dylla-Spears, R.; Townsend, J. E.; Jen-Jacobson, L.; Sohn, L. L.; Muller, S. J., *Lab Chip* **2010**, *10*, 1543.

[18] Kuhn, H.; Frank-Kamenetskii, M. D., *Nucleic Acids Res.* **2008**, *36*, e40.

[19] Dimalanta, E. T.; Lim, A.; Runnheim, R.; Lamers, C.; Churas, C.; Forrest, D. K.; de Pablo, J. J.; Graham, M. D.; Coppersmith, S. N.; Goldstein, S.; Schwartz, D. C., *Anal. Chem.* **2004**, *76*, 5293.

[20] Dukkipati, V. R.; Kim, J. H.; Pang, S. W.; Larson, R. G., *Nano Lett.* **2006**, *6*, 2499.

[21] Bensimon, A.; Simon, A.; Chiffaudel, A.; Croquette, V.; Heslot, F.; Bensimon, D., *Science* **1994**, *265*, 2096.

[22] Bensimon, D.; Simon, A. J.; Croquette, V.; Bensimon, A., *Phys. Rev. Lett.* **1995**, *74*, 4754.

[23] Allemand, J. F.; Bensimon, D.; Jullien, L.; Bensimon, A.; Croquette, V., *Biophys. J.* **1997**, *73*, 2064.

[24] Michalet, X.; Ekong, R.; Fougerousse, F.; Rousseaux, S.; Schurra, C.; Hornigold, N.; vanSlegtenhorst, M.; Wolfe, J.; Povey, S.; Beckmann, J. S.; Bensimon, A., *Science* **1997**, *277*, 1518.

[25] Douville, N.; Huh, D.; Takayama, S., *Anal. Bioanal. Chem.* **2008**, *391*, 2395.

[26] Perkins, T. T.; Smith, D. E.; Chu, S., *Science* **1997**, *276*, 2016.

[27] Smith, D. E.; Chu, S., *Science* **1998**, *281*, 1335.

[28] Schroeder, C. M.; Babcock, H. P.; Shaqfeh, E. S. G.; Chu, S., *Science* **2003**, *301*, 1515.

[29] Schroeder, C. M.; Shaqfeh, E. S. G.; Chu, S., *Macromolecules* **2004**, *37*, 9242.

[30] Larson, J. W.; Yantz, G. R.; Zhong, Q.; Charnas, R.; D'Antoni, C. M.; Gallo, M. V.; Gillis, K. A.; Neely, L. A.; Phillips, K. M.; Wong, G. G.; Gullans, S. R.; Gilmanshin, R., *Lab Chip* **2006**, *6*, 1187.

[31] Juang, Y. J.; Wang, S.; Hu, X.; Lee, L. J., *Phys. Rev. Lett.* **2004**, *93*, 268105.

[32] Randall, G. C.; Schultz, K. M.; Doyle, P. S., *Lab Chip* **2006**, *6*, 516.

[33] Balducci, A.; Doyle, P. S., *Macromolecules* **2008**, *41*, 5485.

[34] Tegenfeldt, J. O.; Bakajin, O.; Chou, C. F.; Chan, S. S.; Austin, R.; Fann, W.; Liou, L.; Chan, E.; Duke, T.; Cox, E. C., *Phys. Rev. Lett.* **2001**, *86*, 1378.

[35] Kim, J. M.; Doyle, P. S., *Lab Chip* **2007**, *7*, 213.

[36] Trahan, D. W.; Doyle, P. S., *Biomicrofluidics* **2009**, *3*, 012803.

[37] de Gennes, P. G., *Science* **1997**, *276*, 1999.

[38] Long, D.; Viovy, J. L.; Ajdari, A., *Phys. Rev. Lett.* **1996**, *76*, 3858.

[39] Smith, D. E.; Babcock, H. P.; Chu, S., *Science* **1999**, *283*, 1724.

[40] Randall, G. C.; Doyle, P. S., *Macromolecules* **2005**, *38*, 2410.

[41] Shaqfeh, E. S. G., *J. Non-Newtonian Fluid Mech.* **2005**, *130*, 1.

[42] Larson, R. G., *J. Rheol.* **2005**, *49*, 1.

[43] Brochard, F.; de Gennes, P. G., *J. Chem. Phys.* **1977**, *67*, 52.

[44] Brochard, F., *J. Phys. (Paris)* **1977**, *38*, 1285.

[45] Daoud, M.; de Gennes, P. G., *J. Phys. (Paris)* **1977**, *38*, 85.

[46] Odijk, T., *Macromolecules* **1983**, *16*, 1340.

[47] Han, J.; Craighead, H. G., *Science* **2000**, *288*, 1026.

[48] Fu, J. P.; Schoch, R. B.; Stevens, A. L.; Tannenbaum, S. R.; Han, J. Y., *Nature Nanotech.* **2007**, *2*, 121.

[49] Jun, S.; Mulder, B., *Proc. Natl. Acad. Sci. U.S.A.* **2006**, *103*, 12388.

[50] Purohit, P. K.; Kondev, J.; Phillips, R., *Proc. Natl. Acad. Sci. U.S.A.* **2003**, *100*, 3173.

[51] Sproul, D.; Gilbert, N.; Bickmore, W. A., *Nat. Rev. Genet.* **2005**, *6*, 775.

[52] Odijk, T., *J. Chem. Phys.* **2006**, *125*, 204904.

[53] Odijk, T., *Phys. Rev. E* **2008**, *77*, 060901(R).

[54] Han, J. Y.; Fu, J. P.; Schoch, R. B., *Lab Chip* **2008**, *8*, 23.

[55] Chen, Y. L.; Graham, M. D.; de Pablo, J. J.; Randall, G. C.; Gupta, M.; Doyle, P. S., *Phys. Rev. E.* **2004**, *70*, 060901(R).

[56] Balducci, A.; Mao, P.; Han, J. Y.; Doyle, P. S., *Macromolecules* **2006**, *39*, 6273.

[57] Hsieh, C.-C.; Balducci, A.; Doyle, P. S., *Macromolecules* **2007**, *40*, 5196.

[58] Hsieh, C.-C.; Balducci, A.; Doyle, P. S., *Nano Lett.* **2008**, *8*, 1683.

[59] Lin, P.-K.; Fu, C.-C.; Chen, Y.-L.; Chen, Y.-R.; Wei, P.-K.; Kuan, C. H.; Fann, W. S., *Phys. Rev. E* **2007**, *76*, 011806.

[60] Bonthuis, D. J.; Meyer, C.; Stein, D.; Dekker, C., *Phys. Rev. Lett.* **2008**, *101*, 108303.

[61] Strychalski, E. A.; Levy, S. L.; Craighead, H. G., *Macromolecules* **2008**, *41*, 7716.

[62] Lin, P.-K.; Lin, K.-H.; Fu, C.-C.; Lee, K.-C.; Wei, P.-K.; Pai, W.-W.; Tsao, P.-H.; Chen, Y.-L.; Fann, W. S., *Macromolecules* **2009**, *42*, 1770.

[63] Uemura, H.; Ichikawa, M.; Kimura, Y., *Phys Rev E* **2010**, *81*, 051801.

[64] Levy, S. L.; Craighead, H. G., *Chem. Soc. Rev.* **2010**, *39*, 1133.

[65] Bakajin, O. B.; Duke, T. A. J.; Chou, C. F.; Chan, S. S.; Austin, R. H.; Cox, E. C., *Phys. Rev. Lett.* **1998**, *80*, 2737.

[66] Balducci, A.; Hsieh, C. C.; Doyle, P. S., *Phys. Rev. Lett.* **2007**, *99*, 238102.

[67] Gerashchenko, S.; Steinberg, V., *Phys. Rev. E* **2008**, *78*, 040801(R).

[68] Rubinstein, M.; Colby, R. H., *Polymer Physics*, Oxford University Press, New York 2003.

[69] Doi, M.; Edwards, S. F., *The Theory of Polymer Dynamics*, Oxford University Press, New York 1986.

[70] Sunada, W. M.; Blanch, H. W., *Biotechnol. Prog.* **1998**, *14*, 766.

[71] Smith, D. E.; Perkins, T. T.; Chu, S., *Macromolecules* **1996**, *29*, 1372.

[72] Kleinert, H., *Path Integrals in Quantum Mechanics, Statistics, Polymer Physics, and Financial Markets*, World Scientific, New Jersey 2004.

[73] Perkins, T. T.; Quake, S. R.; Smith, D. E.; Chu, S., *Science* **1994**, *264*, 822.

[74] Flory, P. J., *Statistical Mechanics of Chain Molecules*, Hanser/Gardner Publications, New York 1969.

[75] Fixman, M.; Kovac, J., *J. Chem. Phys.* **1973**, *58*, 1564.

[76] Marko, J. F.; Siggia, E. D., *Macromolecules* **1995**, *28*, 8759.

[77] Smith, S. B.; Cui, Y. J.; Bustamante, C., *Science* **1996**, *271*, 795.

[78] Zimm, B. H., *J. Chem. Phys.* **1956**, *24*, 269.

[79] Deen, W. M., *Analysis of Transport Phenomena*, Oxford University Press, New York 1998.

[80] Probstein, R. F., *Physicochemical Hydrodynamics*, John Wiley & Sons, Inc., New Jersey 2003, 2 edn.

[81] Russel, W. B.; Saville, D. A.; Schowalter, W. R., *Colloidal Dispersions*, Cambridge University Press, London 1999.

[82] Zheng, J. J.; Li, H.-W.; Yeung, E. S., *J. Phys. Chem. B* **2004**, *108*, 10357.

[83] Henry, D. C., *Proc. R. Soc. Lond. A* **1931**, *133*, 106.

[84] Long, D.; Dobrynin, A. V.; Rubinstein, M.; Ajdari, A., *J. Chem. Phys.* **1998**, *108*, 1234.

[85] Long, D.; Ajdari, A., *Eur. Phys. J. E* **2001**, *4*, 29.

[86] van den Heuvel, M. G. L.; de Graaff, M. P.; Lemay, S. G.; Dekker, C., *Proc. Natl. Acad. Sci. U.S.A.* **2007**, *104*, 7770.

[87] Stellwagen, N. C.; Gelfi, C.; Righetti, P. G., *Biopolymers* **1997**, *42*, 687.

[88] Stigter, D., *J. Phys. Chem.* **1978**, *82*, 1424.

[89] Ohshima, H., *J. Colloid Interface Sci.* **1996**, *180*, 299.

[90] Long, D.; Viovy, J. L.; Ajdari, A., *Biopolymers* **1996**, *39*, 755.

[91] Ferree, S.; Blanch, H. W., *Biophys. J.* **2003**, *85*, 2539.

[92] Bird, R. B.; Curtiss, C. F.; Armstrong, R. C.; Hassager, O., *Dynamics of Polymeric Liquids, Volume 2: Kinetic Theory*, Wiley-Interscience, New York 1987, 2 edn.

[93] Magda, J. J.; Larson, R. G.; Mackay, M. E., *J. Chem. Phys.* **1988**, *89*, 2504.

[94] Larson, R. G.; Magda, J. J., *Macromolecules* **1989**, *22*, 3004.

[95] Larson, R. G., *J. Non-Newtonian Fluid Mech.* **2000**, *94*, 37.

[96] Larson, R. G.; Hu, H.; Smith, D. E.; Chu, S., *J. Rheol.* **1999**, *43*, 267.

[97] Perkins, T. T.; Smith, D. E.; Larson, R. G.; Chu, S., *Science* **1995**, *268*, 83.

[98] Reisner, W.; Morton, K. J.; Riehn, R.; Wang, Y. M.; Yu, Z. N.; Rosen, M.; Sturm, J. C.; Chou, S. Y.; Frey, E.; Austin, R. H., *Phys. Rev. Lett.* **2005**, *94*, 196101.

[99] Randall, G. C.; Doyle, P. S., *Proc. Natl. Acad. Sci. U.S.A.* **2005**, *102*, 10813.

[100] Mao, P.; Han, J. Y., *Lab Chip* **2005**, *5*, 837.

[101] Randall, G. 2006, *Single Molecule Analysis of DNA Electrophoresis in Microdevices*, Ph.D. thesis, Massachusetts Institute of Technology.

[102] Perkins, T. T. 1997, *Exploring Polymer Dynamics with Single DNA Molecules*, Ph.D. thesis, Stanford University.

[103] Bustamante, C.; Macosko, J. C.; Wuite, G. J. L., *Nat. Rev. Mol. Cell Biol.* **2000**, *1*, 130.

[104] Tegenfeldt, J. O.; Prinz, C.; Cao, H.; Chou, S.; Reisner, W. W.; Riehn, R.; Wang, Y. M.; Cox, E. C.; Sturm, J. C.; Silberzan, P.; Austin, R. H., *Proc. Natl. Acad. Sci. U.S.A.* **2004**, *101*, 10979.

[105] Cohen, A. E.; Moerner, W. E., *Appl. Phys. Lett.* **2005**, *86*, 093109.

[106] Randall, G. C.; Doyle, P. S., *Phys. Rev. Lett.* **2004**, *93*, 058102.

[107] Randall, G. C.; Doyle, P. S., *Macromolecules* **2006**, *39*, 7734.

[108] Xia, Y.; Whitesides, G. M., *Angew. Chem. Int. Ed.* **1998**, *37*, 551.

[109] Guo, L. J.; Cheng, X.; Chou, C. F., *Nano Lett.* **2004**, *4*, 69.

[110] Mannion, J. T.; Reccius, C. H.; Cross, J. D.; Craighead, H. G., *Biophys. J.* **2006**, *90*, 4538.

[111] Zhang, C.; Zhang, F.; van Kan, J. A.; van der Maarel, J. R. C., *J. Chem. Phys.* **2008**, *128*, 225109.

[112] Krishnan, M.; Monch, I.; Schwille, P., *Nano Lett.* **2007**, *7*, 1270.

[113] Doyle, P. S.; Bibette, J.; Bancaud, A.; Viovy, J.-L., *Science* **2002**, *295*, 2237.

[114] Brochard-Wyart, F., *Europhys. Lett.* **1993**, *23*, 105.

[115] Hsieh, C.-C.; Doyle, P. S., *Korea-Aust. Rheol. J.* **2008**, *20*, 127.

[116] de Gennes, P. G., *J. Chem. Phys.* **1974**, *60*, 5030.

[117] Tang, J.; Doyle, P. S., *Appl. Phys. Lett.* **2007**, *90*, 224103.

[118] Lee, J. S.; Shaqfeh, E. S. G.; Muller, S. J., *Phys. Rev. E* **2007**, *75*, 040802.

[119] Balducci, A. G.; Tang, J.; Doyle, P. S., *Macromolecules* **2008**, *41*, 9914.

[120] Vincenzi, D.; Bodenschatz, E., *J. Phys. A* **2006**, *39*, 10691.

[121] Celani, A.; Puliafito, A.; Vincenzi, D., *Phys. Rev. Lett.* **2006**, *97*, 118301.

[122] Beck, V. A.; Shaqfeh, E. S. G., *J. Chem. Phys.* **2006**, *124*, 094902.

[123] Beck, V. A.; Shaqfeh, E. S. G., *J. Rheol.* **2007**, *51*, 561.

[124] Cordeiro, C. E.; Molisana, M.; Thirumalai, D., *J. Phys. II (France)* **1997**, *7*, 433.

[125] Stein, D.; van der Heyden, F. H. J.; Koopmans, W. J. A.; Dekker, C., *Proc. Natl. Acad. Sci. U.S.A.* **2006**, *103*, 15853.

[126] van Vliet, J. H.; ten Brinke, G., *J. Chem. Phys.* **1990**, *93*, 1436.

[127] van Vliet, J. H.; Luyten, M. C.; ten Brinke, G., *Macromolecules* **1992**, *25*, 3802.

[128] Cifra, P.; Bleha, T., *Macromol. Theory Simul.* **1999**, *8*, 603.

[129] Hsu, H. P.; Grassberger, P., *J. Chem. Phys.* **2004**, *120*, 2034.

[130] Cifra, P.; Benkova, Z.; Bleha, T., *Faraday Discuss.* **2008**, *139*, 377.

[131] Graham, M., *Annu. Rev. Fluid Mech.* **2010**, *43*, 273.

[132] Schellman, J. A.; Stigter, D., *Biopolymers* **1977**, *16*, 1415.

[133] Batchelor, G. K., *An Introduction to Fluid Dynamics*, Cambridge University Press, Cambridge, England 1967.

[134] Liron, N.; Mochon, S., *J. Eng. Math.* **1976**, *10*, 287.

[135] Maier, B.; Rädler, J. O., *Macromolecules* **2000**, *33*, 7185.

[136] Hecht, E., *Optics*, Addison Wesley, San Fransisco 2002, 4 edn.

[137] Zhang, B.; Zerubia, J.; Olivo-Marin, J. C., *Appl. Opt.* **2007**, *46*, 1819.

[138] Underhill, P. T.; Doyle, P. S., *J. Rheol.* **2006**, *50*, 513.

[139] Jendrejack, R. M.; de Pablo, J. J.; Graham, M. D., *J. Chem. Phys.* **2002**, *116*, 7752.

[140] Heyes, D. M.; Melrose, J. R., *J. Non-Newtonian Fluid Mech.* **1993**, *46*, 1.

[141] Kim, J. M.; Doyle, P. S., *J. Chem. Phys.* **2006**, *125*, 074906.

[142] Woo, N. J.; Shaqfeh, E. S. G.; Khomami, B., *J. Rheol.* **2004**, *48*, 281.

[143] Fang, L.; Hu, H.; Larson, R. G., *J. Rheol.* **2005**, *49*, 127.

[144] Dobrynin, A. V., *Macromolecules* **2006**, *39*, 9519.

[145] Lerman, L. S., *J. Mol. Biol.* **1961**, *3*, 18.

[146] Sischka, A.; Toensing, K.; Eckel, R.; Wilking, S. D.; Sewald, N.; Ros, R.; Anselmetti, D., *Biophys. J.* **2005**, *88*, 404.

[147] Murade, C. U.; Subramaniam, V.; Otto, C.; Bennink, M. L., *Nucleic Acids Res.* **2010**, *38*, 3423.

[148] Günther, K.; Mertig, M.; Seidel, R., *Nucleic Acids Res., doi: 10.1093/nar/gkq434* **2010**.

[149] Savin, T.; Doyle, P. S., *Biophys. J.* **2005**, *88*, 623.

[150] Underhill, P. T.; Doyle, P. S., *J. Non-Newtonian Fluid Mech.* **2004**, *122*, 3.